Doctoral Thesis

Organic Electroluminescence Devices with

Microcavity Structure of

Thiophene/Phenylene Co-Oligomer Thin Films

Shohei Dokiya

Graduate School of Materials Science

Nara Institute of Science and Technology

March 2019

Supervisor : Prof. Hisao Yanagi

Table of Contents

Abstract

For the next step after practical commercialization of organic electroluminescence (EL) devices, increasing attentions have been paid to development of an organic semiconductor laser with excellent tunable emission wavelength in a visible region. However, the realization of electrically pumped organic lasers requires high-density carrier injection, reduced waveguiding loss due to light absorption by electrodes, and bypassing non-radiative triplet excitons and polarons. Consequently, selection of functional materials and consideration of device structures are necessary. Among a variety of organic molecular species, thiophene/phenylene co-oligomers (TPCOs) are robust materials with high fluorescence efficiency and high carrier transport characteristics. Optically pumped lasing from TPCO crystals have been achieved and spectrally narrowed emission has been reported for a single crystal based light-emitting field-effect transistor, suggesting that TPCO crystals have a promising potential as organic laser media. On the other hand, an organic polariton laser can be regarded as an alternative to ordinary photon lasing owing to its lower lasing threshold energy. Polariton lasing is coherent radiation from exciton-polaritons generated by strong coupling between emissive excitons and photons typically confined in a microcavity the optical length of which is of an order of the emission wavelength. Moreover, owing to the large exciton binding energy and large oscillator strength in Frenkel excitons, organic materials are favorable as active media for polariton lasing.

In this study, toward development of an electrically pumped organic polariton laser, organic microcavity EL devices with TPCO vapor-deposited films were examined aiming formation of exciton-polaritons at room temperature under optical and electrical excitation. Firstly, Chapter 1, an introduction to research background on organic EL devices, TPCOs, laser oscillation, and exciton-polariton in a microcavity is stated. In Chapter 2, optical amplification

characteristics in vapor-grown single crystals of 5,5'-bis(4-biphenylyl)-2,2'-bithiophene (BP2T) and 5,5'-bis(4'-cyanobiphenyl-4-yl)-2,2'-bithiophene (BP2T-CN) were described. In Chapter 3, organic EL devices with TPCOs were investigated. In section 3.1, organic EL devices with a heterojunction of BP2T and BP2T-CN vapor-deposited films as p- and n-type, respectively, were explained. In Section 3.2, improvement of EL devices with reversed BP2T and BP2T-CN bilayer films was stated. In Section 3.3, EL devices with p-i-n double heterojunction structure using 5'''-bis(4-trifluoromethylphenyl)[2,2';5',2'';5'',2'''] quarter thiophene (P4T-CF$_3$) film as i-type were investigated. In Chapter 4, organic microcavity EL devices with TPCO vapor-deposited films were examined for evaluating exciton-photon interaction. In Chapter 5, a crystalline film growth technique for organic lasing materials is proposed and their EL properties were stated. Finally, Chapter 6, summary and future works on this thesis were described.

Chapter 1

Introduction

1.1 Research Backgrounds

Organic semiconductor materials have been intensively investigated in both fundamental science researches and optoelectronic applications such as organic electroluminescence (EL) devices, field-effect transistors (OFETs), photovoltaic cells, and biosensors. For the next step after practical commercialization of these organic devices, an organic semiconductor laser is expected to be one of next research targets because of light weight, low temperature manufacturing, and tunable emission color. Although optically pumped organic lasers have been reported, few works have demonstrated on electrically pumped ones. In order to realize electrically pumped organic lasing, it should be considered to reduce lasing threshold and avoid non-radiative excitons quenching. To overcome these issues, polariton lasing which is a coherent radiation from exciton-polaritons have been focused. Exciton-polaritons are created by the strong coupling between emissive excitons and photons confined in a microcavity. Moreover, owing to the large exciton binding energy and large oscillator strength in Frenkel excitons, molecule-based polaritons are capable of realizing room-temperature organic polariton lasing. Among a variety of organic molecular species, thipohene/phenylene co-oligomers (TPCOs) have a promising potential for organic laser media owing to their high fluorescence quantum yield, excellent semiconducting properties, and robustness. In this study, aiming at electrically excited exciton-polariton formation at room temperature, organic microcavity EL devices with vapor deposition of p-n heterojunction films of TPCO derivatives

were investigated toward development of an electrically pumped organic polariton laser.

In the following sections, fundamental properties of organic EL devices, TPCOs, laser oscillation, and exciton-polariton in a microcavity are stated. Finally, the aim of this study is described.

1.2   Organic Electroluminescence (EL) Devices

Organic EL devices are light emitting devices using EL phenomena in which the energy of electrically excited state in organic molecules is deactivated and extracted as the light energy. This device is called "a carrier injection type device" since the excited state is formed by carrier injection and recombination in organic layers. **Figure. 1.1** shows a device structure of a common organic EL device and its energy band diagram. In general, organic EL devices have a structure with organic layers consisting of a hole-transport layer (HTL), an emitting layer (EML), and an electron-transport layer (ETL) with typically 100 ~ 300 nm thickness sandwiched between metal anode and cathode electrodes. Holes are injected into the HOMO energy of HTL and electrons are injected into the LUMO energy of ETL, from the anode and cathode, respectively. In EML, excitons can be generated by the recombination of holes and electrons transported through the HTL and ETL, respectively. Then, the excitons emit light corresponding to the HOMO/LUMO gap energy when they relaxed to the ground states. In an improved device structure, hole and/or electron injection layers (HIL and/or EIL) are inserted between the anode and HTL and/or the cathode and ETL, respectively, to reduce the carrier injection barrier. Moreover, hole- and/or electron blocking layers (HBL and/or EBL) are also introduced to improve the charge balance of carriers and the confinement of excitons in the EML.

In the 1960s M. Pope *et al.* and W. Helfrich *et al.* observed blue EL from an anthracence single crystal with electrolyte electrodes.[1−3] Although the applied voltage was rather high at

(a)

(b)
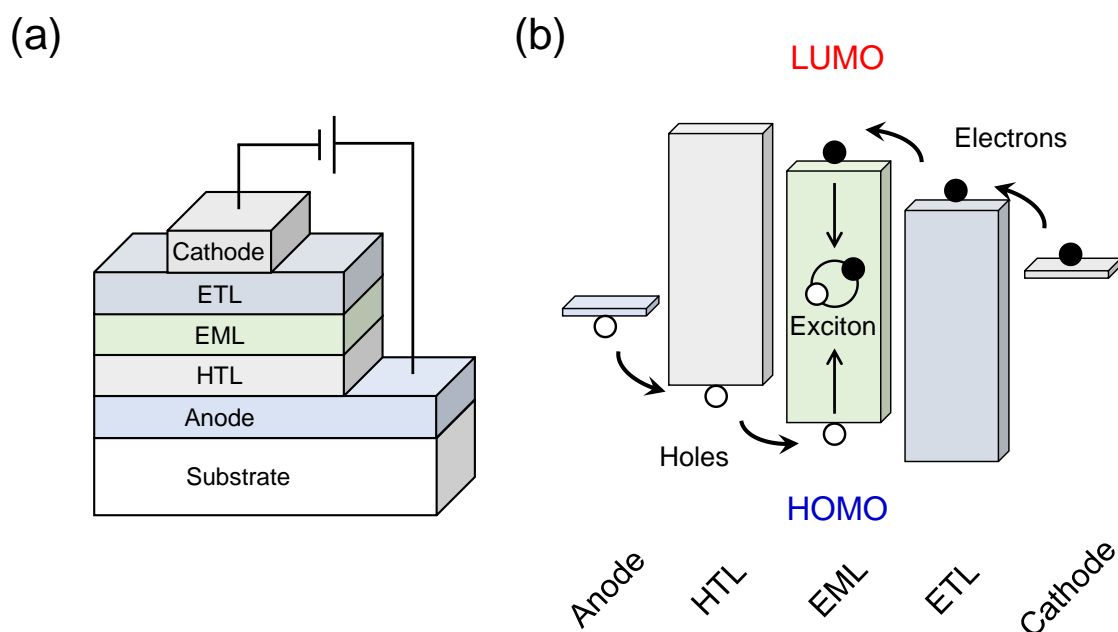
Fig. 1.1. Schematic diagrams of device structure (a) and energy band diagram (b) for common organic EL device.

100 V ~ 10 kV due to using thick crystals with 10 μm ~ 1 mm in thickness, these results open the way towards organic EL devices as the first report. In 1987, C. W. Tang and S. A. VanSlyke have reported p-n heterojunction EL devices using tris(8-hydroxyquinolinato)aluminium(III) (Alq₃) as EML/ETL and 1,1-bis[4-(N,N-di(p-tolyl)amino)phenyl]cyclohexane as HTL.[4] This device achieved a high luminescence of over 1000 cd/m^2 at below 10 V and a high external quantum efficiency (η_{ext}) of nearly 1%. In the EL process, recombined holes and electrons form singlet excitons having antiparallel spins and triplet excitons having parallel spins at a ratio of 1:3 in accordance with the spin statistics. Consequently, internal quantum efficiency (η_{int}) of EL based on radiative decay processes of fluorescence and phosphorescence are limited 25 and 75%, respectively. C. Adachi *et al.* have demonstrated high-efficiency EL devices with the nearly 100% η_{int} employing a phosphorescent molecule doped into a wide energy gap host.[5] By these studies, research and development of EL devices such as lightning and displays have been accelerated because of their light weight, low temperature manufacturing, and flexibility.

However, phosphorescent compounds consist of rare metals, e.g. Ir, Pt, and Au, and it is difficult for these devices to realize stable blue EL.[6] As solving these problems, H. Uoyama *et al.* have achieved almost 100% of η_{int} from metal-free organic electroluminescent molecules by utilizing thermally activated delayed fluorescence (TADF). In TADF molecules, electrically injected triplet excitons can be utilized by reverse intersystem crossing (RISC) due to a small energy gap between the singlet and triplet excited states (ΔE_{ST}). By optimizing molecular design for small ΔE_{ST} and large oscillator strength, TDAF based EL devices have exhibited excellent EL performance with η_{ext} of over 30% resulting in η_{int} of 100%.[7,8] Recently, R. Nagata *et al.* have reported a new way to exceed the 100% limit for exciton production.[9] This technology uses a process called singlet fission to split the energy from a single exciton to two triplet excitons, making it possible to exceed the 100% limit for the efficiency of converting charge pairs into excitons.

Thus, based on both development of new organic materials and improvement of organic EL devices, a number of researchers have been extensively studying toward next-generation electronics devices such as organic transistors, organic photovoltaic cells, and organic lasers.

1.3   Applications of Organic Lasers

In 1966, P. P. Sorokin and F. P. Schäfer have reported the stimulated emission from a dye molecule, chloro-aluminum phthalocyanine dissolved in an organic solvent under high-density optical pumping.[10] Moreover, B. Soffer and B. McFarland have observed dye-doped matrix lasing in 1967.[11] Organic dye lasers have realized practical commercialization until now owing to a wide variable wavelength range operating from the ultraviolet (UV) to infrared region. Organic laser active materials are well known to offer highly efficient laser oscillation due to a high gain coefficient. However, dye lasers require the solution circulation to prevent from fading by deterioration. Besides, the emission efficiency of laser dye molecules decreases
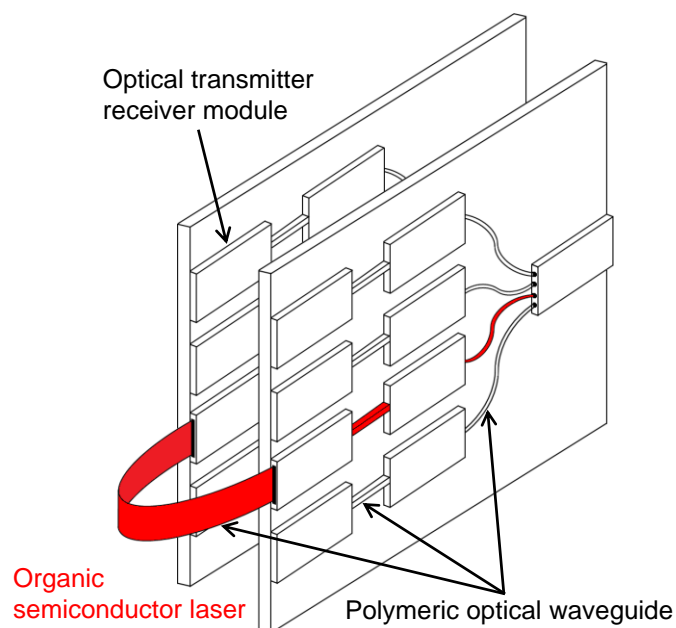
Fig. 1.2. Schematic diagram of optical interconnection system with polymeric waveguides.

significantly at high concentrations.[12] From these background, it has been demanded to develop electrically pumped organic semiconductor lasers with easily fabricated process and tunable emission wavelength without large scale equipment at high cost. Due to advantages of organic materials such as flexibility and low temperature processes, flexible semiconductor laser devices can be fabricated using plastic substrates.

Especially, many applications such as optical transmission systems[13] and bio-sensing[14,15] have been developed by using coherent sources from organic semiconductor lasers. Compared with quartz optical fibers, polymeric optical fibers enable easy and low manufacturing process and are more applicable for plug optical interconnection. Furthermore, polymer fibers can be used at small curvatures without using additional connecting devices. Flexible polymeric fibers offer chip to chip, on chip, and board to board optical interconnection at low cost and large transmission capacitance as shown in **Fig. 1.2**. As the light source of these devices, organic semiconductor lasers are useful due to their wavelength tenability and low refractive index difference with polymeric waveguides. On the other hand, bio-sensors which

detect trace substances in a wide range of fields such as blood bio-markers have been demonstrated by using organic laser source. It has been proposed that organic lasers are used as an excitation source to detect biomolecules via surface-enhanced Raman scattering (SERS).[16] Therefore, research and development of organic semiconductor laser are extremely significant in both fundamental science research and industrial application.

1.4   Thiophene/Phenylene Co-Oligomers (TPCOs)

Organic semiconductor lasers can be realized by light amplification in a resonator under much higher current density injection than organic EL devices. Thus, the development of organic molecules with high optical gain, high career mobility, and material robustness having p-and n-type semiconducting conductions for EL devices is required.

For example, *p*-sexiphenyl (*p*-6P) is a stable molecule with high luminescence efficiency, while α-sexythiophene (α-6T) is often used for organic photovoltaic cells owing to its high carrier mobility. As shown in **Fig. 1.3**, with an increase of the phenylene and/or thiophene rings in the π-conjugated oligomers, their emission wavelength is red-shifted by reduction of the $\pi-\pi$ conjugation HOMO/LUMO energies. The *p*-6P remains blue emission since the π conjugation is limited by its twisted chain structure, while the α-6T shows orange color due to delocalized π electrons over the planar chain structure. The emission intensity is reduced in the α-6T thin film by intermolecular quenching among closely packed molecules. On the other hand, *p*-6P shows a high fluorescence quantum yield even in the solid state since the intermolecular distance is moderately maintained due to the twisted structure.

From these research background, thiophene/phenylene co-oligomers (TPCOs) which consist of a variety combination of thiophene and phenylene rings have been synthesized.[17−19] **Figure. 1.3** also shows fluorescence spectra of α, ω-bis(4-biphenylyl)oligothiophene (BPnT, n = 1 ~ 4) crystals. These molecular crystals are very robust under UV excitation in air and their
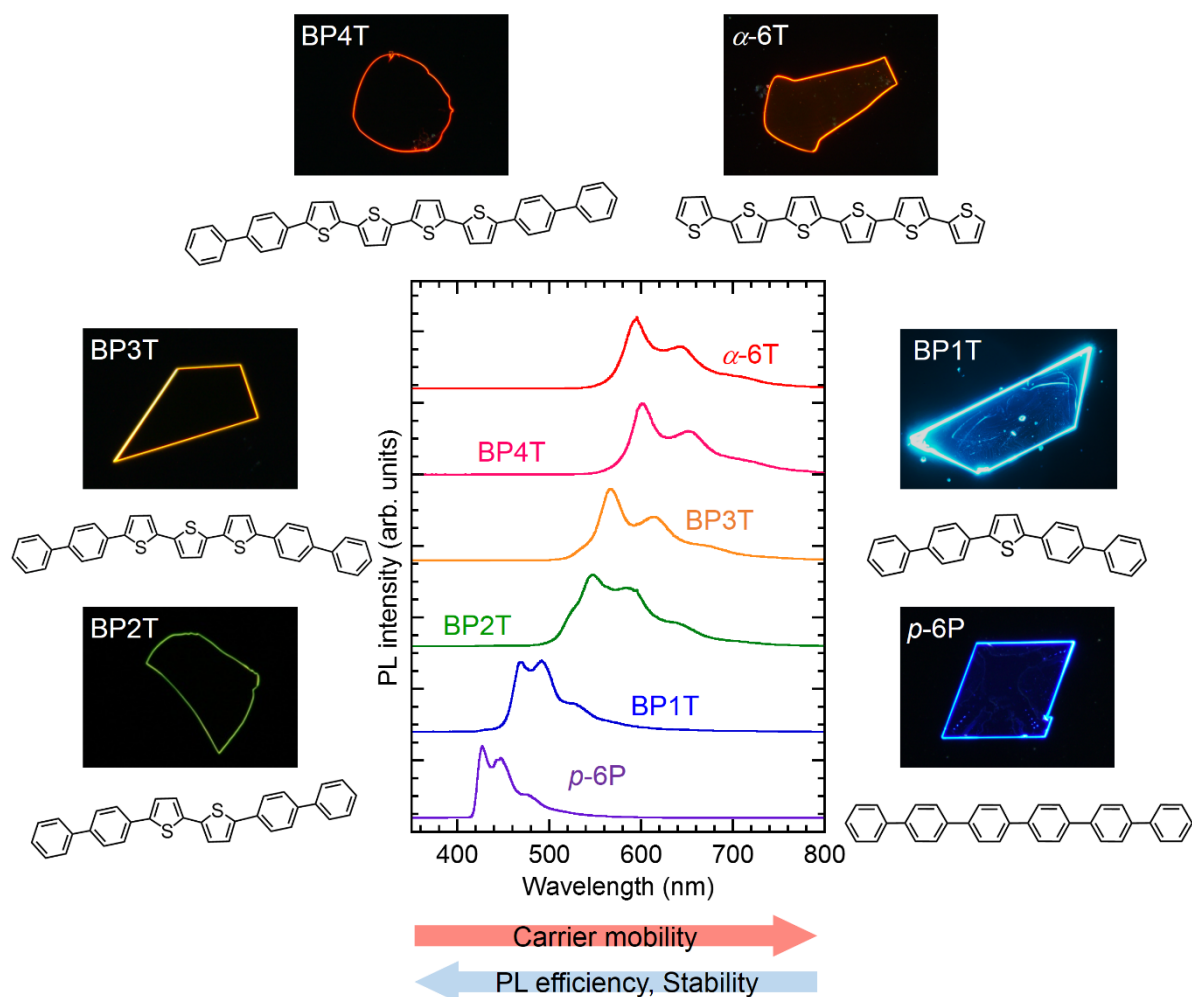
Fig. 1.3. Molecular structures of p-6P, BPnT (n = 1~4), and α-6T, and fluorescence micrographs and fluorescence spectra taken from their crystals.

luminescence color is tunable. As the number of thiophene rings increases, the emission color changes from blue to red, and generally the carrier mobility increases with increasing thiophene rings due to co-facial π–π stacking.

1.4.1 Chemically Modified TPCO Derivatives

Conduction types of TPCOs can be controlled by introduction of peripheral groups as depicted in **Fig. 1.4**. For example, by putting electron-donating methoxy groups at both ends of 2,5-bis(4-biphenylyl)thiophene (BP1T) molecule, the HOMO/LUMO energies of 2,5-
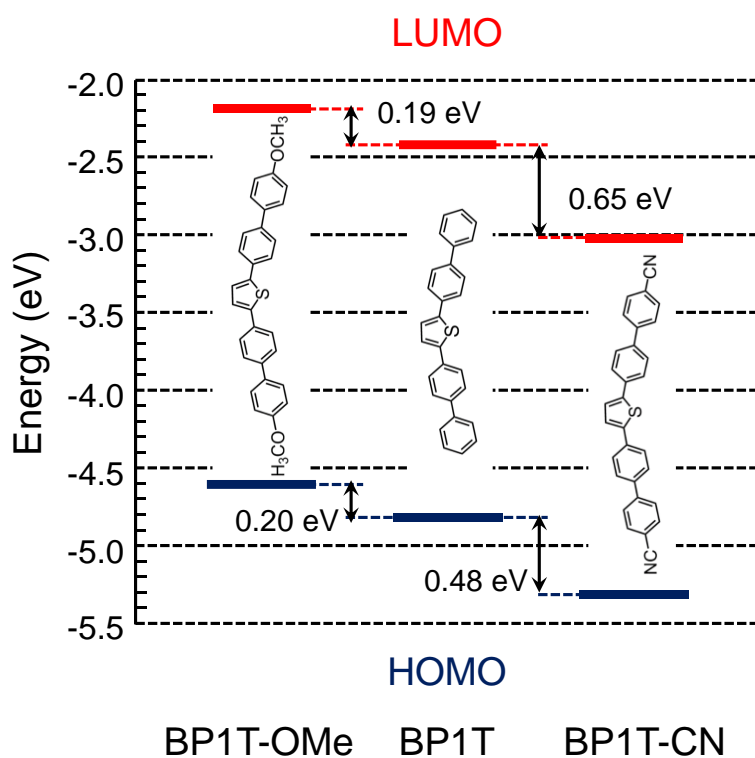
Fig. 1.4. Molecular structures and HOMO/LUMO energy levels of BP1T-OMe, BP1T, and BP1T-CN.

bis(4'-methoxybiphenyl-4-yl)thiophene (BP1T-OMe) are increased by 0.20/0.19 eV, respectively, resulting in p-type conduction. By contrast, the substitution into BP1T with electron-withdrawing cyano groups, the HOMO/LUMO energies of 2,5-bis(4'-cyanobiphenyl-4-yl)thiophene (BP1T-CN) are deepened by 0.48/0.65 eV, respectively, resulting in n-type conduction. These calculations were carried out by using density functional theory (DFT) method.[20] Such the easy control of p-n conductions is very useful for constructing EL devices using TPCO derivatives.

1.4.2   Structure of TPCO Single Crystals

Crystal data and unit-cell structures reported for BPnT (n = 1 ~ 4)[21,22] are displayed in **Table 1.1** and **Fig. 1.5,** respectively. All single crystals of BPnT belong to monoclinic forms with the space group either $P2_1/n$ or $P2_1/c$, $Z = 4$, and the unique axis of b. The BPnT molecules

Table 1.1. Crystallographic Date of BPnT (n = 1 ~ 4).

	crystal class	space group	a (Å)	b (Å)	c (Å)	β (deg)	Z
BP1T	*monoclinic*	$P2_1/n$	7.6080	5.8219	43.760	93.510	4
BP2T	*monoclinic*	$P2_1/c$	5.7081	7.6036	52.465	97.147	4
BP3T	*monoclinic*	$P2_1/c$	7.5262	5.7856	59.997	92.818	4
BP4T	*monoclinic*	$P2_1/n$	5.6824	7.5850	67.907	91.475	4
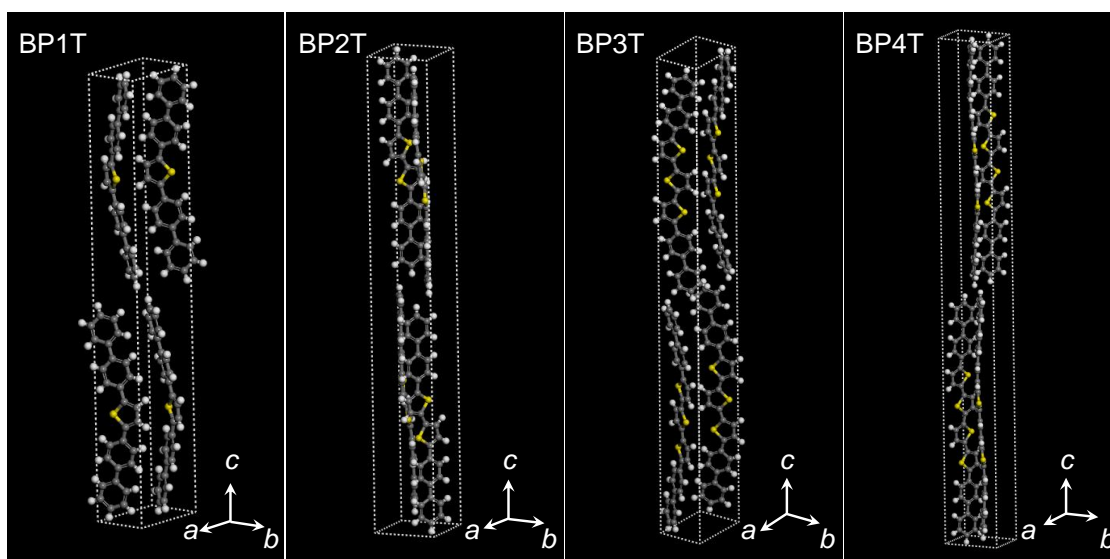
Fig.1.5. Crystal structure of BPnT (n = 1 ~ 4).[21, 22]

are crystallized with their molecular *c*-axis almost standing perpendicular to the *ab*-plane. The tilting angles of BP1T, BP2T, BP3T, and BP4T are 1.0, 1.2, 2.6, and 2.8°, respectively. The molecules form a herringbone structure in the *ab*-plane, and the herringbone angles of the BP1T, BP2T, BP3T, and BP4T molecules are 37.5, 61.0, 43.8, and 67.6°, respectively. The molecular chain of BP1T and BP3T has a bent structure belonging to the point group of C_{2v}, while those of BP2T and BP4T molecules have a zigzag shape belonging to C_{2h}. These TPCO single crystals are typically obtained in a thin platelet morphology. Since the π-electronic transition dipole moment of BPnT is almost parallel to their long molecular axis, the emitted light is propagated in the transverse magnetic (TM) mode in the platelet crystal as shown in
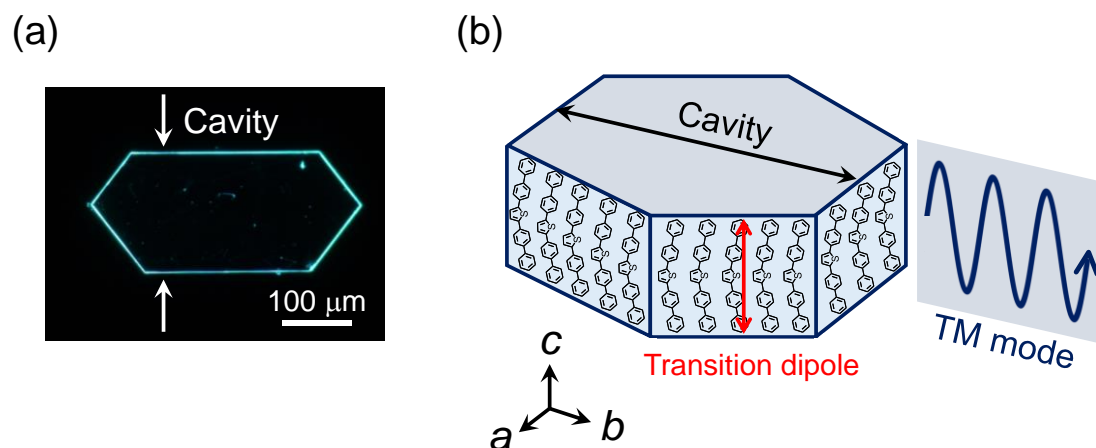
Fig. 1.6. Fluorescence micrograph (a) and model of molecular alignment (b) of BP1T single crystal.

Fig. 1.6. This TM polarization and high effective refractive index of the TPCO crystals are suitable for effective confinement of emitted light in the planar crystal cavity resulting in amplified emission. Moreover, parallel facets of the TPCO single crystal function as a Fabry−Pérot (F−P) resonator to attain the lasing action.

1.4.3　Electronic Transition and Optical Spectra of TPCO Single Crystals

　　Figure 1.7(a) shows optical absorption and fluorescence spectra of the BP1T single crystal taken under UV excitation. This crystal indicates blue emission with emission peak at around 465, 495, and 525 nm, which are assigned to 0−1, 0−2, and 0−3 vibronic progressions, respectively, of the HOMO/LUMO transition. The absorption spectrum shows bands at around 415 and 385 nm, corresponding to 0−1 and 0−2 transitions, respectively. Due to antiparallel exciton coupling between the adjacent molecules, the 0−0 transition in TPCO single crystals is basically forbidden and the 0−1, 0−2, and 0−3 transitions are allowed as depicted in **Fig. 1.7(b)**.

(a)　　　　　　　　　　　　　　　　(b)
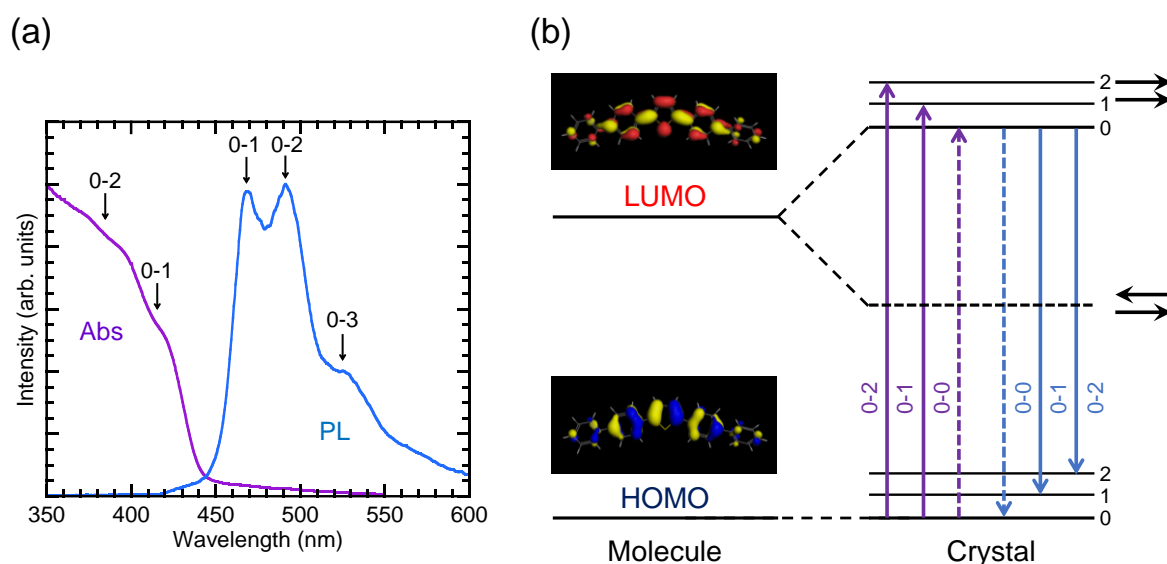
Fig. 1.7. (a) Fluorescence (blue) and absorption (purple) spectra of BP1T single crystal. (b) HOMO/LUMO of BP1T and schematic diagram of energy levels showing splitting of excited state for TPCOs single crystals.

1.5   Amplified Spontaneous Emission (ASE) and Laser Oscillation

1.5.1   Spontaneous Emission, Stimulated Absorption, and Stimulated Emission

In general, electrons exist in the lower level (ground state) in the steady state, and they are excited resulting to the unstable higher level (excited state) by energy stimulation. Absorption occurs when electrons are excite to the higher level (E_2), while emission occurs when the electrons are relaxed to the lower level (E_1) by emitting photons having an energy corresponding to the difference between those two energy levels ($h\nu = E_2 - E_1$). The latter process is called spontaneous emission as displayed in **Fig. 1.8(a)**, while the former process is called stimulated absorption as shown in **Fig. 1.8(b)**. The top spectrum in **Figure 1.9** shows a spontaneous emission taken from the BP1T single crystal. When the emitted photon is incident to the excited state, the electron existing in the E_2 level is stimulated to relax to the E_1 level, and another photon with the same energy of $h\nu = E_2 - E_1$ is emitted. In this process, the phase of emitted light is kept same as that of the incident light. Therefore, if this process called stimulated emission occurs successively, the output light is amplified as displayed in **Fig. 1.8(c)**.

(a)   (b)   (c)
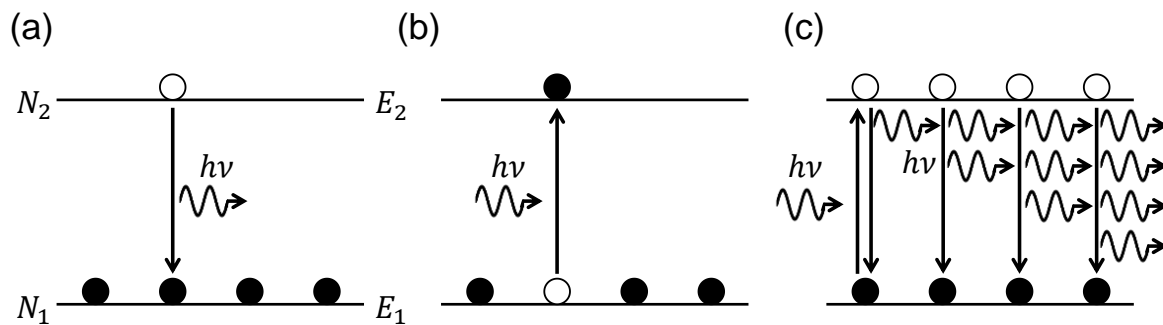
Fig. 1.8. Schematic depiction for spontaneous emission (a), stimulated absorption (b), and stimulated emission (c).
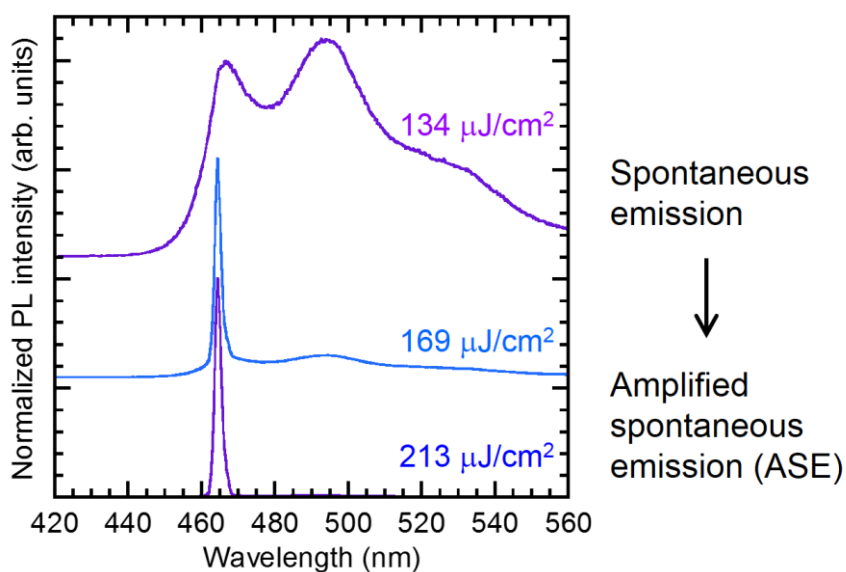
Fig. 1.9. Spontaneous emission and ASE spectra from the single crystal of BP1T.

Amplified spontaneous emission (ASE) as shown in the middle and bottom spectra in **Fig. 1.9** is based on this stimulated emission process.

The population of the ground state N_1 is larger than that of the excited state N_2 in the normal conditions of thermal equilibrium following Boltzmann distribution ($N_1 > N_2$). However, the population of the excited state N_2 can be larger than that of N_1 by giving intense energy (e. g. by optically or electrically pumping). This scheme is called population inversion ($N_2 > N_1$). In order to realize the light amplification, the formation of population inversion is necessary.

1.5.2   Laser Oscillation Conditions

For laser oscillation, an optical resonator is required to confine photons to proceed the stimulated emission. In **Fig. 1.10(a)**, a F–P type resonator is described. In this resonator, reflecting mirrors are set on both sides of the active medium so that the light wave is repeatedly reflected in the resonator. Thus, both mirrors must be located exactly in parallel.

The amplification factor of one round-trip wave electric-field along the z axis is generally described as $R_1 R_2 e^{(g-\alpha)L}$, where R_1 and R_2 are the reflectance of both mirrors (R_1, $R_2 < 1$), g is the optical gain coefficient in the resonator, α is the loss coefficient in the resonator, L is the resonator length, as shown in **Fig. 1.10(a)**. When this factor exceeds 1, the light wave is amplified by repeated round-trip reflections. Therefore, the laser oscillation condition is expressed as follows:

$$R_1 R_2 e^{(g-\alpha)L} e^{-j2kL} = 1, \tag{1.1}$$

where k is a propagation constant of the light wave. k is given by using an effective refractive index n_{eff} and the wavelength in a free space λ_0 as following equation,

$$k = \frac{2\pi n_{\text{eff}}}{\lambda_0}. \tag{1.2}$$

If the **formula (1.1)** is distributed into a real part and an imaginary part, the former and the latter correspond to the amplitude condition which determines the oscillation amplification factor and the phase condition which determines the oscillation wavelength, respectively, as represented in **formulas (1.3)** and **(1.4)**,

$$\text{amplitude condition: } R_1 R_2 e^{(g-\alpha)L} \cos(2kL) = 1 \tag{1.3}$$

$$\text{phase condition: } R_1 R_2 e^{(g-\alpha)L} \sin(2kL) = 0. \tag{1.4}$$

From **formula (1.3)**, the following relationship can be derived,

$$R_1 R_2 e^{(g-\alpha)L} = 1. \tag{1.5}$$

The **formula (1.5)** indicates that the laser oscillation is obtained when the gain of the medium

(a)

(b)

(c)
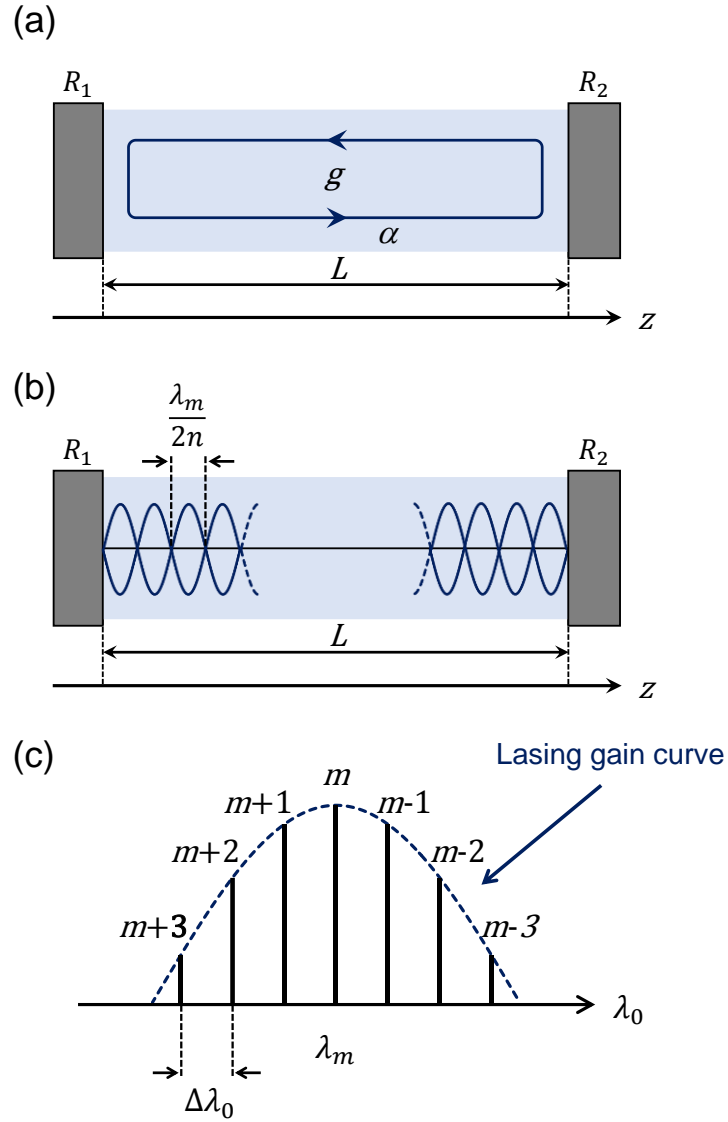
Fig. 1.10.   Schematic representations for Fabry−Pérot (F−P) resonator (a), standing wave in the resonator (b), and longitudinal mode spectrum (c).

overcomes the loss of the resonator. From this formula, threshold gain g_{th} can be expressed as,

$$g_{th} = \alpha + \frac{1}{L}\ln\left(\frac{1}{R_1 R_2}\right). \tag{1.6}$$

On the other hand, the following equation is given according to the **formula (1.4)**,

$$2kL = 2\pi m \quad (m = 0, 1, 2, \cdots), \tag{1.7}$$

where m is an integer. Therefore, the oscillation wavelength is represented by using the
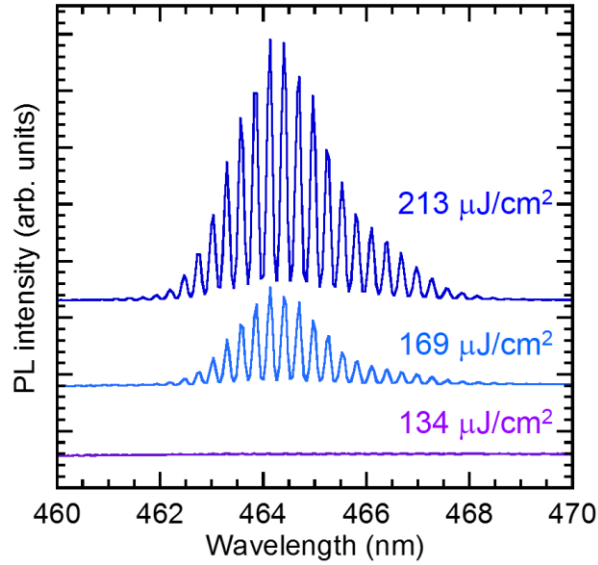
Fig. 1.11. Lasing spectra of longitudinal mode from single crystal of BP1T.

formula (1.2),

$$\lambda_{\mathrm{m}} = \frac{2nL}{m}.$$

(1.8)

When the condition of the **formula (1.8)** is satisfied, a standing wave is generated in the resonator as depicted in **Fig. 1.10(b)**. The period of a standing wave is a half wavelength $\lambda_{\mathrm{m}}/2n_{\mathrm{eff}}$ in the laser medium. Since the gain medium has a wavelength band capable of optical amplification, the laser oscillation occurs at intermittent wavelengths existing in that region and satisfying the **formula (1.8)**. This wavelength interval in a free space $\Delta\lambda^{-1}$ can be described as,

$$\Delta\lambda^{-1} = \frac{1}{2n_{\mathrm{g}}L},$$

(1.9)

where n_{g} is the group refractive index of the gain medium. This oscillation mode is called a longitudinal mode as displayed in **Fig. 1.10(c)**. Longitudinal mode lasing spectra from the BP1T single crystal under optically pumping is shown in **Fig. 1.11**.

1.6 Light-Emitting Devices with TPCO Single Crystals

Light amplification characteristics such as ASE[23,24], F–P lasing[25–28], whispering-gallery mode (WGM)[29–32], stimulated resonant Raman scattering (SRRS)[33,34], and superfluorescence (SF)[35,36] have been demonstrated from single crystals of TPCOs under optical excitation.

As the first report on single crystal-based organic EL devices with TPCOs, EL from low-dimensionally confined crystals (Al/*p*-6P/BP2T/ITO) was achieved by H. Yanagi *et al.* and co-workers.[37] Epitaxially oriented BP2T needle crystals were fabricated by vapor deposition on a cleaved (100) face of a KCl crystal at 150 °C as depicted in **Fig. 1.12(a)**. At low applied voltages, this device shows blue light emission from the vapor-deposited *p*-6P film because of carrier recombination in the Al/*p*-6P/ITO region as schematically displayed in **Fig. 1.12(b)**. By increasing the bias voltage, green EL from BP2T needle crystals was observed from the Al/*p*-6P/BP2T/ITO region. After this report, EL has also observed from platelet single crystals of TPCOs using the laminating method[38] and the template stripping technique[39,40] onto the electrode.

In addition to those organic EL devices, organic light-emitting field effect transistors (OLEFETs) have also attracted much attention as electrically excited light emission in organic semiconductors. K. Yamane *et al.* have fabricated an OLEFET with a TPCO thin film and a buffer layer of n-triacontane and an electron injection layer of pentacene and demonstrated light emission with excellent ambipolar carrier transport properties.[41] Moreover, S. Z. Bisri *et al.* have reported a high performance ambipolar OLEFET that contains a single crystal of 5,5″-bis(4-biphenylyl)-2,2′:5′,2″-terthiophene (BP3T) with both high luminescence and high carrier mobility (μ_h = 1.64 cm^2/Vs and μ_e = 0.17 cm^2/Vs),[42] as shown in **Fig. 1.13**. T. Yamao *et al.* have reported effective operation conditions of OLEFETs under AC-gate operation to promote carrier injection from source and drain electrodes into the organic single crystal.[43] Compared
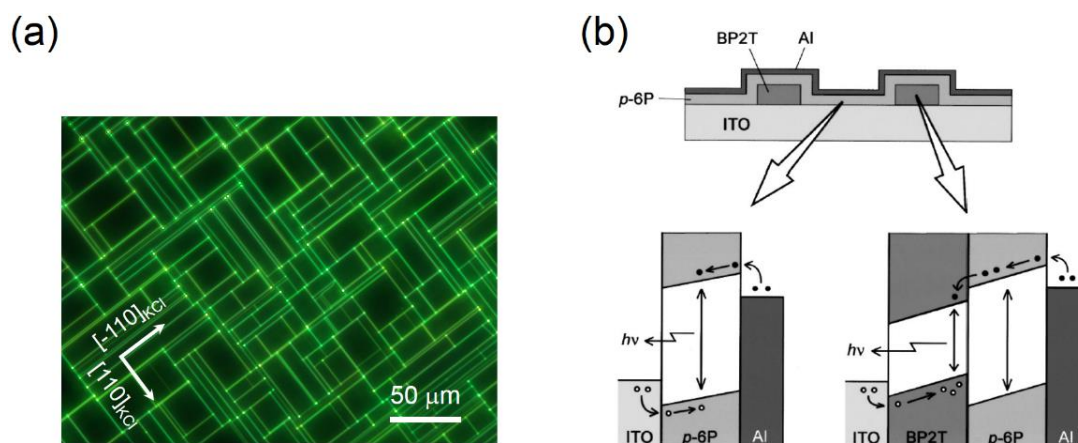
Fig. 1.12. (a) Fluorescence micrographs taken from epitaxially grown needle crystals of BP2T deposited on the KCl (001) surface. (b) Schematic diagrams for EL device structure and energy band configurations at Al/p-6P/ITO and Al/p-6P/BP2T/ITO regions. Reprinted with permission from Ref. 26. Copyright 2002 by American Institute of Physics.
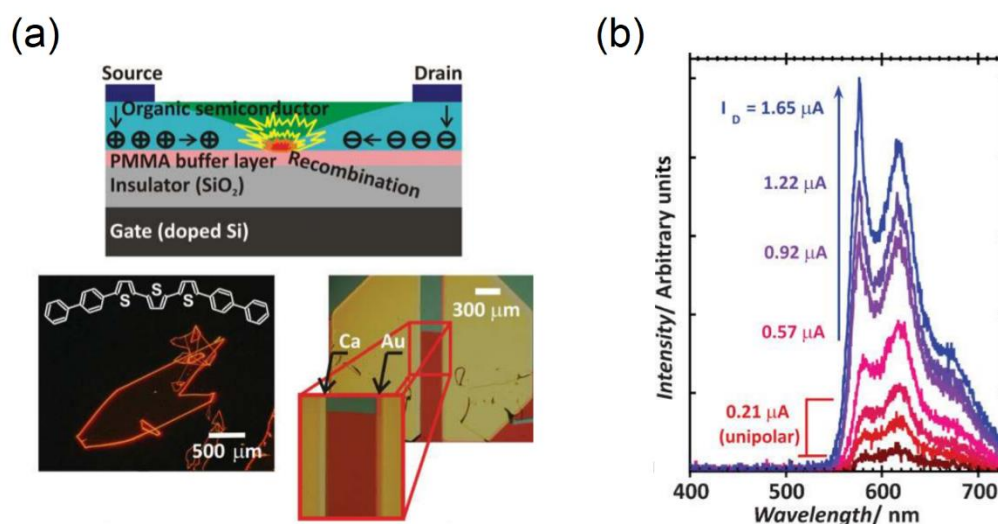
Fig. 1.13. (a) OLEFET device structure, fluorescence micrograph taken from the single crystal of BP3T, and top view micrograph of the device. (b) Excitation-density dependence of EL spectra from the BP3T single crystal-based OLEFET device. Reprinted with permission from Ref. 31. Copyright 2009 WILEY-VCH Verlag GmbH & Co. KGaA, Weinheim.

to under DC gate voltages, EL intensity was significantly enhanced. Furthermore, spectrally narrowed emission (FWHM ~1.1 nm) has been obtained from the OLEFET device by applying a square-wave gate voltage as depicted in **Fig. 1.14**.[44]
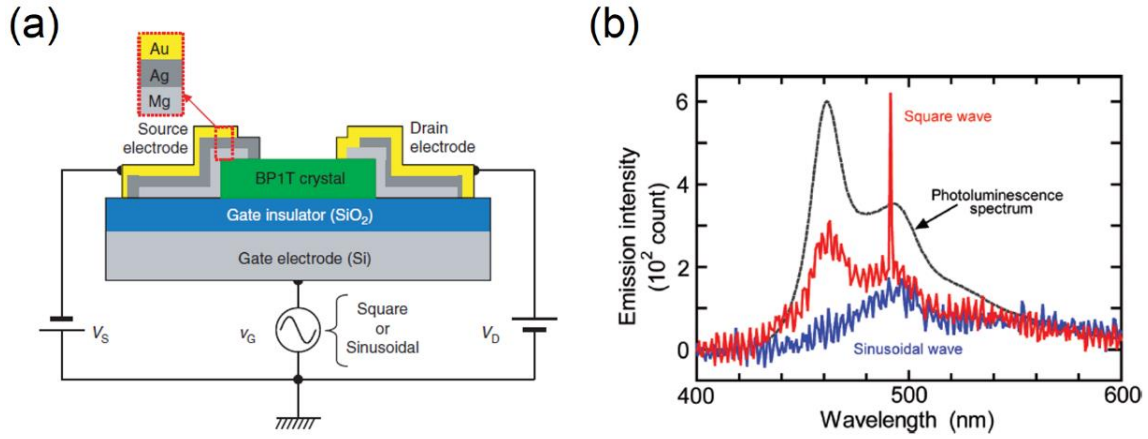
Fig. 1.14. (a) Schematic representation of the electrical circuit that operates the OLEFET. (b) EL spectra of the OLEFET devices under square (red)- and sinusoidal (blue)-wave gate operations in comparison with PL spectrum of the BP1T single crystal (black). Reprinted with permission from Ref. 32. Copyright 2010 by American Scientific Publishers.

The OLEFETs structure has some advantage such as reducing the waveguiding loss due to light absorption by electrodes and the exciton quenching aroused by metal contacts and injected polarons. However, these devices require a high gate or drain-source voltage (~250 V) to obtain EL, and their light emitting areas are limited to narrow line shape. From this viewpoint, in this study, organic EL devices are investigated and vertical cavity surface emitting structure using DBR mirrors is adopted toward electrically pumped organic semiconductor lasers.

1.7 Exciton-polariton in a Microcavity

1.7.1 Microcavity

The most common type planar microcavity is described in **Fig. 1.15**. This cavity comprises of two facing parallel mirrors placed with the cavity length L of light wavelength scale. The wavevector $\vec{k}$ of a cavity photon modes depends on the angle with respect to the surface normal θ_{int} as following formula,

$$\vec{k} = \frac{m\pi}{n_{\text{eff}}L}\frac{1}{\cos\theta_{\text{int}}},$$

(1.10)
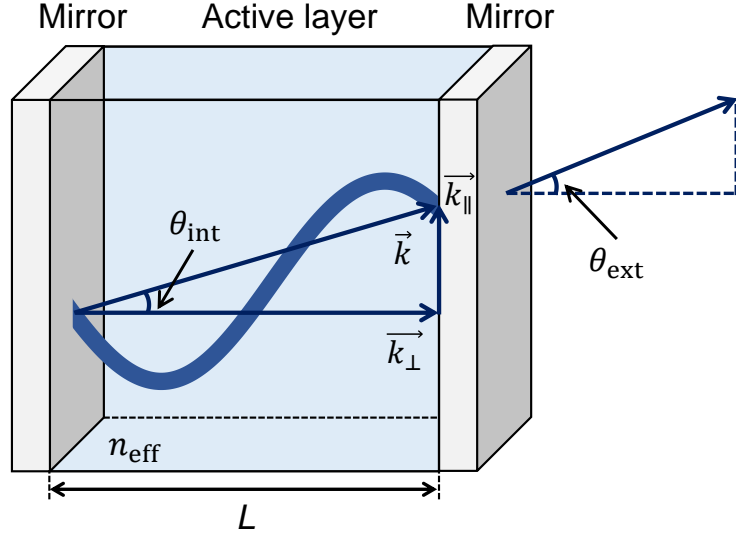
Fig. 1.15. Schematic diagrams of a microcavity.

where, m and n_{eff} are an integer and the effective refractive index in a microcavity, respectively.

The wavevector can be divided with perpendicular $\overrightarrow{k_\perp}$ and parallel $\overrightarrow{k_\parallel}$ components with respect to the mirror. The perpendicular component is quantizes by a cavity according to the **formula (1.11)**, while the parallel component depends on the angle of propagation as represented in the **formula (1.12)**,

$$\overrightarrow{k_\perp} = \frac{m\pi}{n_{\text{eff}}L},\qquad (1.11)$$

$$\overrightarrow{k_\parallel} = \vec{k}\,\sin\theta_{\text{int}}.\qquad (1.12)$$

The energy of cavity photon mode $E_{\text{ph}}(\theta)$ is given by

$$E_{\text{ph}}(\theta) = E_{\text{ph}}(0)\left(1 - \frac{\sin^2\theta}{n_{\text{eff}}^2}\right)^{-1/2}.\qquad (1.13)$$

$E_{\text{ph}}(0) = \frac{hc\,\overrightarrow{k_\perp}}{2\pi}$ is the cavity cutoff energy and $\sin\theta_{\text{ext}} = n_{\text{eff}}\sin\theta_{\text{int}}$ according to Snell's law.

Therefore, the dispersion relation of the cavity photon has angle dependence as shown in **formula (1.13)**.

The mirrors used for a microcavity generally composes of either metal or distributed

Bragg reflectors (DBRs). Metallic mirrors are easily fabricated by vapor-deposition method. However, the mode microcavity introduces optical absorption losses resulting in decrease of the Q factor of the microcavity. Since exciton-polaritons are half-matter and half-light bosonic quasi-particles as described next subsection, it collapses when the balance between them is broken due to photon lifetime. On the other hand, DBRs have a higher reflectance over a wide range of wavelengths, called stopband without the absorption loses since it consists of two dielectric material layers with alternating high and low refractive indices. In this thesis, the top metal/bottom DBR mirror structure was used for organic microcavity EL devices for evaluation of exciton-photon coupling by taking advantages of both the mirrors.

1.7.2 Exciton-polariton

Exciton-polaritons are quasi-particles defined as the mixture of excitons and photons typically confined in a microcavity and generated by the strong coupling with each other. In a microcavity, the photon energy are quantized to discrete values. When the photon energy coincides with exciton energy in the active medium, strong coupling regime called cavity polariton is created by resonance between electromagnetic field of cavity photons and excitonic polarizations.

The exciton and photon can be considered as coupled oscillators and described by a phenomenological 2×2 Hamiltonian as expressed in **formula (1.14)**,

$$\begin{pmatrix} E_{\mathrm{ph}}(\theta) & \hbar\Omega \\ \hbar\Omega & E_{\mathrm{ex}} \end{pmatrix} \begin{pmatrix} \alpha_{\mathrm{ph}}(\theta) \\ \alpha_{\mathrm{ex}}(\theta) \end{pmatrix} = E_{\mathrm{pol}} \begin{pmatrix} \alpha_{\mathrm{ph}}(\theta) \\ \alpha_{\mathrm{ex}}(\theta) \end{pmatrix}. \tag{1.14}$$

E_{ex} and $\hbar\Omega$ are the exciton energy and the exciton-photon interaction terms, respectively. The eigenvalue of this Hamiltonian corresponds to the polariton energies E_{pol} split to the upper polariton branch (UPB) and the lower polariton branch (LPB). The eigenvectors (α_{ph} and α_{ex}) indicate the polariton mixing coefficients of the photon and exciton modes contributing to the
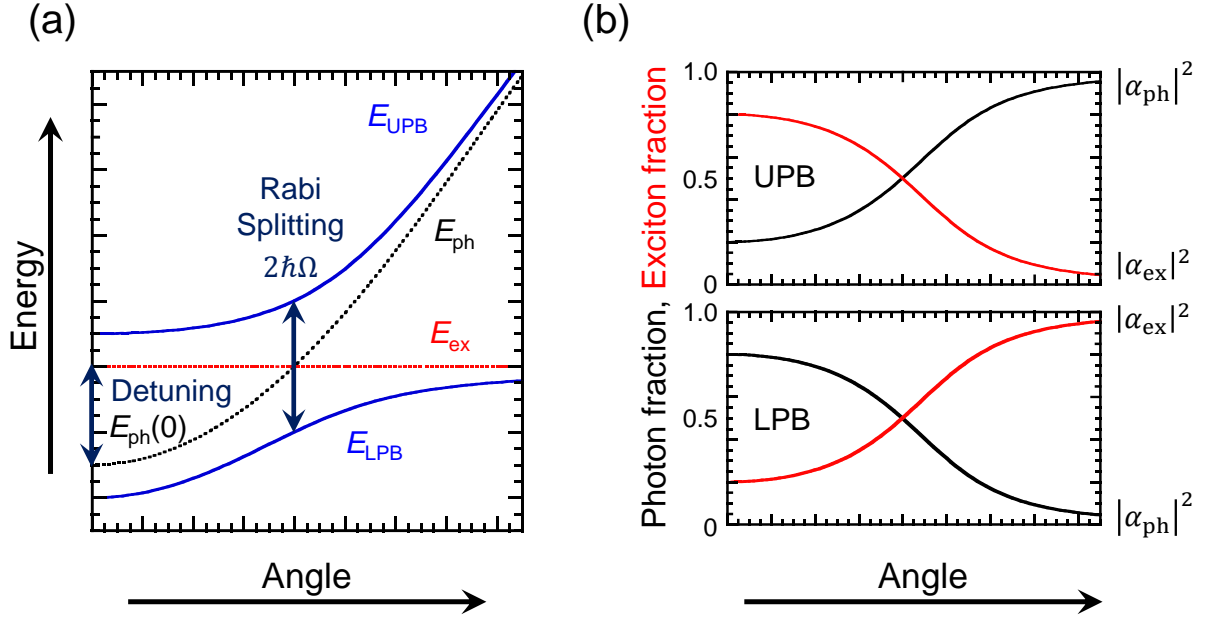
Fig. 1.16. (a) Dispersion characteristics of polariton modes for a strong coupled microcavity. The solid blue lines show dispersions of the upper and lower polariton blanches (UPB and LPB). Black and red dashed lines indicated the cavity photon (E_{ph}) and exciton (E_{ex}) modes, respectively. (b) Angle-dependence of polariton mixing fractions for UPB and LPB, respectively. Black and red solid lines are cavity photon and exciton fraction, respectively.

the polariton. Consequently, E_{pol}, α_{ph}^2, and α_{ex}^2 are described as

$$E_{pol} = \frac{1}{2}\left[E_{ph} + E_{ex} \pm \sqrt{(2\hbar\Omega)^2 + \left(E_{ph} - E_{ex}\right)^2} \right] \qquad (1.15)$$

$$\alpha_{ph}^2 = \frac{E_{ph} - E_{pol}}{E_{ph} + E_{ext} - 2E_{pol}}, \qquad (1.16)$$

$$\alpha_{ex}^2 = 1 - \alpha_{ph}^2, \qquad (1.17)$$

respectively. The blue lines in **Fig. 1.16(a)** show the dispersion relations of the cavity polaritons

calculated by **formula (1.15)**. At the angle changes, anticrossing dispersions of the UPB the

LPB appear. Corresponding to the cavity length, the energy detuning between the cavity photon

at $\theta = 0°$ and the exciton ($E_{ex} - E_{ph}(0)$) is defined as displayed in **Fig. 1.16(a)**. The energy

difference between the UPB and the LPB is called Rabi-splitting energy ($2\hbar\Omega$) at the resonance

point ($E_{ph} = E_{ex}$) which changes as a function of the oscillator strength and the mode volume.

Figure. 1.16(b) displays polariton mixing coefficients for the UPB and LPB. The UPB is exciton-like at small angle and becomes photon-like with increasing angles. The LPB has more photonic mixing fraction at small angle while the excitonic fraction increases at larger angles. At the resonance point, both the UPB and LPB show half-exciton and half-photon natures.

1.7.3 Polariton Lasing

Since the cavity polaritons generated by strong coupling between the cavity photons and exciton, the particle is united into one energy state. Largely populated polaritons are accumulated at the lowest energy level ($k = 0$) of LPB as the pumping power is increased. In spite of the thermodynamically non-equilibrium state, Bose-Einstein condensation (BEC) has been demonstrated owing to extremely small effective mass of the cavity polaritons ($\sim 10^{-4}$–10^{-5} times lighter than that of an electron).[45,46] Since the BEC is formed via stimulated relaxation phenomenon to the $k = 0$, the accumulated polaritons induce a coherent condensate. Polariton lasing is a coherent radiation of spontaneous emission from this condensate state as depicted in **Fig. 1.17**. It is distinguished from the conventional photon lasing by specific features such as lower threshold without formation of the population inversion, power-dependent spectral change and phase-transition to a BEC.[46]

In order to realize polariton lasing, active media with a large oscillator strength and a high exciton binding energy are used for microcavities for making strong coupling. The oscillator strength is defined by the electric transition dipole in materials and the intensity of light emission and absorption is proportional to the oscillator strength. The Rabi-splitting energy is proportional to the square of this parameter. The exciton binding energy is a by Coulombic potential acting between a hole and an electron. The larger this parameter, the more excitons becomes stable. Polariton lasing has so far been reported in inorganic semiconductor materials such as GaAs and CdTe microcavity.[46,48,49] However, the strong coupling has been
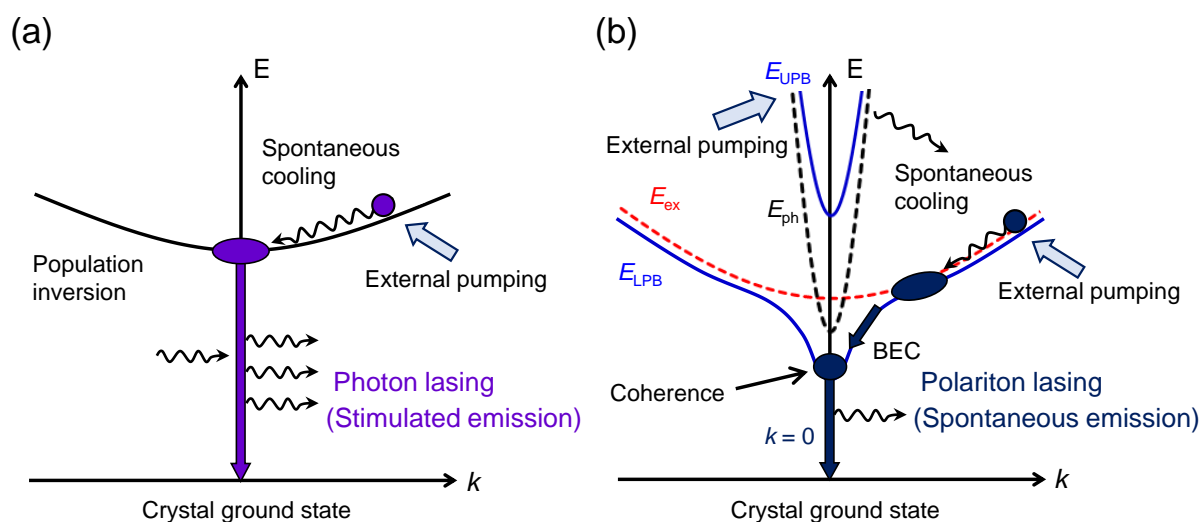
(a)

(b)

Fig. 1.17. Schematic diagrams of the photon lasing (a) and the polariton lasing (b).

demonstrated only at cryogenic temperature because of the small exciton binding energy (5–25 meV) in the Wannier-type excitons. Moreover, electrically pumped polariton lasers are required a large magnetic field (~7 T) to maintain the sufficient oscillator strength.[50,51] By contrast, organic semiconductor materials enables the formation of exciton-polaritons easier owing their large oscillator strength and high exciton binding energy (0.5–1 eV) of Frenkel-type excitons. Recently, room-temperature polariton condensations have been demonstrated using molecular crystals,[52] π-conjugated oligomer and polymer thin films,[53,54] molecular dyes dispersed in a matrix polymer,[55] and a fluorescent protein film[56] under optical excitation. Consequently, exciton-polaritons in organic microcavites are expected to realize a low threshold organic laser.

1.7.4 Organic Microcavity EL Devices

As electrically driven polariton devices using organic materials, organic microcavity EL devices have also been investigated. In 2005, J. R. Tischler *et al.* have first demonstrated electrically excited strong coupling in microcavity EL devices at room temperature.[57] The active layer of this devices is used a vapor-deposited film of cyanine dye, TDBC (5,6-dichloro-
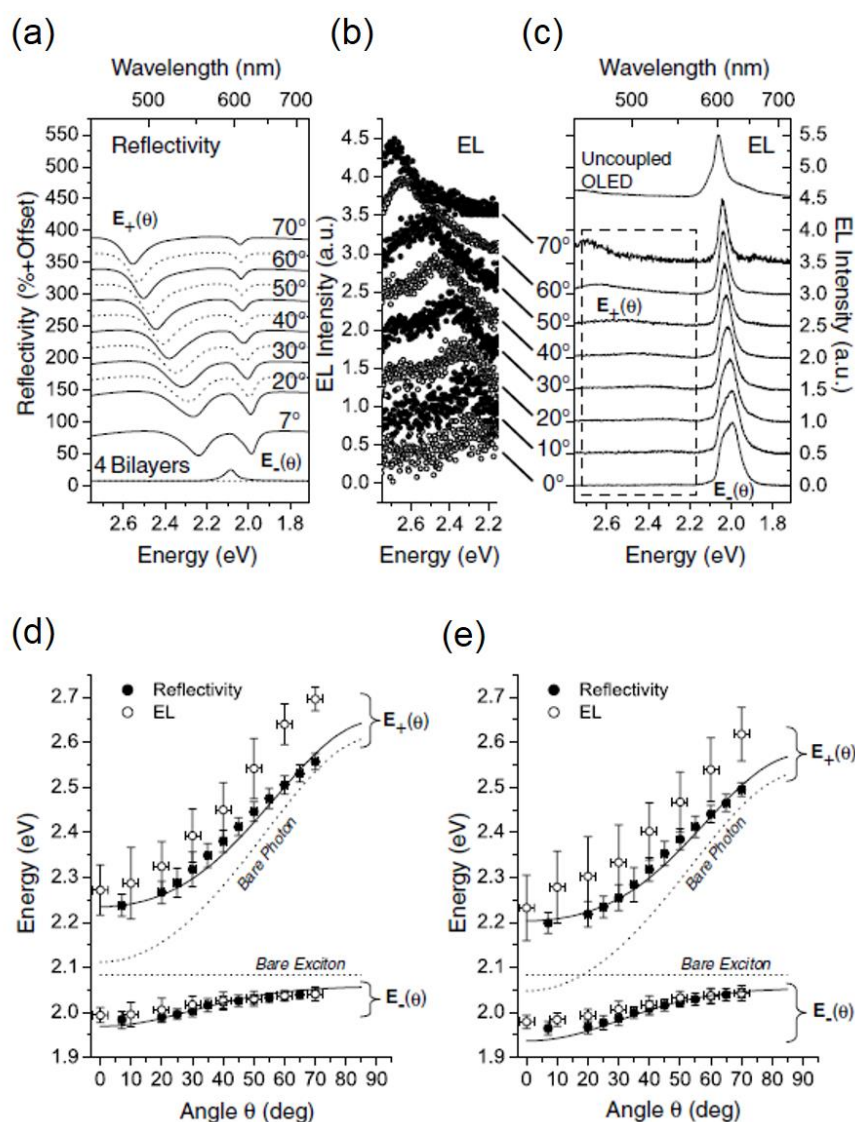
Fig. 1.18. (a) Angle-resolves reflectance spectra taken from the microcavity EL device. (b) and (c) show Angle-resolved EL spectra for the microcavity EL device. (d) and (e) indicate dispersion characteristics of polariton modes for microcavities with different thicknesses. Reprinted with permission from Ref. 46. Copyright 2005 by American Physical Society.

2-[3-[5,6-dichloro-1-ethyl-3-(3-sulfopropyl)-2(3H)-benzimidazolidene]-1-propenyl]-1-ethyl-3-(3-sulfopropyl) benzimidazolium hydroxide, inner salt, sodium salt). The microcavity was formed by the two Ag electrodes. **Figure 1.18** shows angle-resolved reflectance and EL spectra and dispersion characteristics of polariton modes of this microcavity EL devices. Anticrossing dispersions of LPB and weak UPB emission in both measurements indicate that the strong coupling regime with a large Rabi-splitting energy ($2\hbar\Omega = 265$ meV) is achieved under

electrical excitation. Moreover, the cavity length dependence of microcavity EL devices was confirmed with a detuning and a Rabi-splitting energy. After this study, some reports have achieved strong exciton-photon coupling in microcavity EL devices and LEFET devices.[58–65]

1.8   Aim of This Study

As mentioned above, TPCO crystals are promising active media for organic semiconductor laser devices. Especially, organic materials are expected to realize polariton lasing due to their large exciton binding energy and large oscillator strength of Frenkel excitons nature.

Since polariton lasing has been recognized in organic materials under optical pumping, some studies have reported microcavity EL devices to demonstrate polariton formation in current injection. The large Rabi-splitting energy in organic microcavities enables a stable existence of cavity polaritons at room temperature. However, polariton lasing has not yet been realized under electrical pumping. Several reasons such as relaxation bottleneck effect, excitation screening by carriers and nonradiative triplet excitons may impede effective relaxation of injected excitons into the bottom of the LPB.

In this thesis, toward realizing organic polariton lasers, organic microcavity EL devices by using vapor-deposited films with TPCO derivatives were fabricated and evaluated aiming formation of exciton-polariton under optical and electrical pumping at room temperature.

In Chapter 2, optically pumped lasing properties are examined for vapor-grown single crystals of BP2T and BP2T-CN. These attractive materials are chosen as p- and n-type TPCOs are apply for p-n heterojunction-type organic EL devices.

In Chapter 3, EL devices with bilayered BP2T and BP2T-CN films (Al:Li/BP2T-CN/BP2T/ITO) are first fabricated. It confirmed that BP2T and BP2T-CN layers functioned as p- and n-type, respectively. Then inverted EL device structure (Au/BP2T/BP2T-CN/ITO) is

fabricated to improve EL characteristics. Finally, EL devices with p-i-n double heterojunction structure (Al:Li/BP2T-CN/P4T-CF$_3$/BP2T/ITO and Au/BP2T/P4T-CF$_3$/BP2T-CN/ITO) are investigated using P4T-CF$_3$ as the i-layer.

In Chapter 4, organic microcavity EL devices (Au/MoO$_3$/BP2T/BP2T-CN/ITO/DBR) are fabricated based on the inverted p-n junction device structure and the formation of cavity polaritons is examined from angle-resolved reflection, PL, and EL spectra. A strong coupling regime with a large Rabi-splitting energy is observed under both optical and electrical excitations at room temperature. The excitation-density dependence of EL luminance suggests an incorporation of triplet excitons in the polariton formation.

In Chapter 5, a crystalline film growth technique called VFD method is proposed to fabricate EL devices with crystalline TPCOs. Using this method, homogeneous polycrystalline films can be grown and optically pumped lasing and EL characteristics are obtained from this film.

Finally, Chapter 6 summarizes this thesis, and gives some proposal for future works following this study.

References

[1]   M. Pope, H. P. Kallmann, P. Magnante, *J. Chem. Phys.* **1963,** 38, 2042.

[2]   W. Helfrich, W. G. Schneider, *Phys. Rev. Lett.* **1965,** 14, 229.

[3]   W. Helfrich, W. G. Schneider, *J. Chem. Phys.* **1966,** 44, 2902.

[4]   C. W. Tang, S. A. VanSlyke, *Appl. Phys. Lett.* **1987,** 51, 913.

[5]   C. Adachi, M. A. Baldo, M. E. Thompson, S. R. Forrest, *J. Appl. Phys.* **2001,** 90, 5048.

[6]   H. Uoyama, K. Goushi, K. Shizu, H. Nomura, C. Adachi, *Nature* **2012,** 492, 234.

[7]   H. Kaji, H. Suzuki, T. Fukushima, K. Shizu, K. Suzuki, S. Kubo, T. Komino, H. Oiwa, F. Suzuki, A. Wakamiya, Y. Murata, C. Adachi, *Nat. Commun.* **2015,** 6, 8476.

[8]   C. K. Moon, K. Suzuki, K. Shizu, C. Adachi, H. Kaji, J.-J. Kim, *Adv. Mater.* **2017,** 29, 1606448.

[9]   R. Nagata, H. Nakanotani, W. J. Potscavage Jr, C. Adachi, *Adv. Mater.* **2018,** 30, 1801484.

[10] P. P. Sorokin, J. Lankard, *IBM J. Res. Dev.* **1966,** 10, 162.

[11] M. D. McGehee, A. J. Heeger, *Adv. Mater.* **2000,** 12, 1655.

[12] B. Soffer, B. McFarland, *Appl. Phys. Lett.* **1967,** 10, 266.

[13] J. Clark, G. Lanzani, *Nat. Photonics* **2010,** 4, 438.

[14] A. Rose, Z. G. Zhu, C. F. Madigan, T. M. Swager, V. Bulovic, *Nature* **2005,** 434, 876.

[15] Y. Wang, P. O. Morawska, A. L. Kanibolotsky, P. J. Skabra, G. A. Turnbull, I. D. W. Samuel, *Laser Photonics Rev.* **2013,** 7, L71.

[16] X. Liu, S. Lebedkin, H. Besser, W. Pfleging, S. Prinz, M. Wissmann, P. M. Schwab, I. Nazarenko, M. Guttmann, M. M. Kappes, U. Lemmer, *ACS Nano* **2015,** 9, 260.

[17] S. Hotta, S. A. Lee, T. Tamaki, *J. Heterocycl. Chem.* **2000,** 37, 281.

[18] S. Hotta, T. Katagiri, *J. Heterocycl. Chem.* **2003,** 40, 845.

[19] T. Katagiri, S. Ota, T. Ohira, T. Yamao, S. Hotta, *J. Heterocycl. Chem.* **2007,** 44, 853.

[20] H. Mizuno, T. Maeda, H. Yanagi, H. Katsuki, M. Aresti, F. Quochi, M. Saba, A. Mura, G. Bongiovanni, F. Sasaki, S. Hotta, *Adv. Optical Mater.* **2014,** 2, 529.

[21] S. Hotta, M. Goto, *Adv. Mater.* **2002,** 7, 498.

[22] S. Hotta, M. Goto, R. Azumi, M. Inoue, M. Ichikawa, Y. Taniguchi, *Chem. Mater.* **2004,** 16, 237.

[23] M. Nagawa, R. Hibino, S. Hotta, H. Yanagi, M. Ichikawa, T. Koyama, and Y. Taniguchi, *Appl. Phys. Lett.* **2002,** 80, 544.

[24] M. Ichikawa, R. Hibino, M. Inoue, T. Haritani, S. Hotta, T. Koyama, Y. Taniguchi, *Adv. Mater.* **2003,** 15, 213.

[25] M. Ichikawa, R. Hibino, M. Inoue, T. Haritani, S. Hotta, K. Araki, T. Koyama, Y. Taniguchi, *Adv. Mater.* **2005,** 17, 2073.

[26] T. Yamao, K. Yamamoto, Y. Taniguchi, T. Miki, S. Hotta, *J. Appl. Phys.* **2008,** 103, 093115.

[27] H. Mizuno, I. Ohnishi, H. Yanagi, F. Sasaki, S. Hotta, *Adv. Mater.* **2012,** 24, 2404.

[28] H. Mizuno, U. Haku, Y. Marutani, A. Ishizumi, H. Yanagi, F. Sasaki, S. Hotta, *Adv. Mater.* **2012,** 24, 5744.

[29] S. Fujiwara, K. Bando, Y. Masumoto, F. Sasaki, S. Kobayashi, S. Haraichi, S. Hotta, *Appl. Phys. Lett.* **2007,** 91, 021104.

[30] F. Sasaki, S. Kobayashi, S. Haraichi, S. Fujiwara, K. Bando, Y. Masumoto, S. Hotta, *Adv. Mater.* **2007,** 19, 3654.

[31] H. -H. Fang, R. Ding, S. -Y. Lu, Y. -D. Yang, Q. -D. Chen, J. Feng, Y. -Z. Huang, H. -B. Sun, *Laser Photonics Rev.* **2013,** 7, 281.

[32] H. Dong, C. Zhang, X. Lin, Z. Zhou, J. Yao, Y. S. Zhao, *Nano Lett.* **2017,** 17, 91.

[33] H. Yanagi, A. Yoshiki, S. Hotta, S. Kobayashi, *Appl. Phys. Lett.* **2003,** 83, 1941.

[34] H. Yanagi, A. Yoshiki, *Appl. Phys. Lett.* **2004,** 84, 4783.

[35] T. Hiramatsu, N. Matsuoka, H. Yanagi, F. Sasaki, S. Hotta, *Phys. Status. Solidi C* **2009,** 6, 338.

[36] H. Shang, H. Shimotani, S. Ikeda, T. Kanagasekaran, K. Oniwa, T. Jin, N. Asano, Y. Yamamoto, H. Tamura, K. Abe, M. Kanno, M. Yoshizawa, K. Tanigaki, *J. Phys. Chem. C* **2017,** 121, 2364.

[37] H. Yanagi, T. Morikawa, S. Hotta, *Appl. Phys. Lett.* **2002,** 81, 1512.

[38] M. Ichikawa, K. Nakamura, M. Inoue, H. Mishima, T. Haritani, R. Hibino, T. Koyama, and Y. Taniguchi, *Appl. Phys. Lett.* **2005,** 87, 221113.

[39] R. Ding, J. Feng, X. -L. Zhang, W. Zhou, H. -H. Fang, Y. -F. Liu, Q. -D. Chen, H. -Y. Wang, H. B. Sun, *Adv. Funct. Mater.* **2014,** 24, 7085.

[40] R. Ding, J. Feng, W. Zhou, X. -L. Zhang, H. -H. Fang, T. Yang, H. -Y. Wang, S. Hotta, H. B. Sun, *Sci. Rep.* **2015,** 5, 12445.

[41] K. Yamane, H. Yanagi, A. Sawamoto, and S. Hotta, *Appl. Phys. Lett.* **2007,** 90, 162108.

[42] S. Z. Bisri, T. Takenobu, Y. Yomogida, H. Shimotani, T. Yamao, S. Hotta, Y. Iwasa, *Adv. Funct. Mater.* **2009,** 19, 1728.

[43] T. Yamao, Y. Shimizu, K. Terasaki, S. Hotta, *Adv. Mater.* **2008,** 20, 4109.

[44] T. Yamao, K. Terasaki, Y. Shimizu, S. Hotta, *J. Nanosci. Nanotechnol.* **2010,** 10, 1017.

[45] C. Weisbuch, M. Nishioka, A. Ishikawa, Y. Arakawa, *Phys. Rev. Lett.* **1992,** 69, 3314.

[46] H. Deng, G. Weihs, C. Santori, J. Bloch, Y. Yamamoto, *Science* **2002,** 298, 199.

[47] D. Bajoni, *J. Phys. D: Appl. Phys.* **2012,** 45, 313001.

[48] J. Kasprzak, M. Richard, S. Kundermann, A. Baas, P. Jeambrun, J. M. J. Keeling, F. M. Marchetti, M. H. Szymańska, R. André, J. L. Staehli, V. Savona, P. B. Littlewood, B. Deveaud, L. S. Dang, *Nature* **2006,** 443, 409.

[49] R. Balili, V. Hartwell, D. Snoke, L. Pfeiffer, K. West, *Science* **2007,** 316, 1007.

[50] C. Schneider, A. Rahimi-Iman, N. Y. Kim, J. Fischer, I. G. Savenko, M. Amthor, M. Lermer, A. Wolf, L. Worschech, V. D. Kulakovskii, I. A. Shelykh, M. Kamp, S. Reitzenstein, A. Forchel, Y. Yamamoto, S. Höfling, *Nature* **2013,** 497, 348.

[51] P. Bhattacharya, B. Xiao, A. Das, S. Bhowmick, J. Heo, *Phys. Rev. Lett.* **2013,** 110, 206403.

[52] S. Keńa-Cohen, S. R. Forrest, *Nat. Photonics* **2010,** 4, 371.

[53] K. S. Daskalakis, S. A. Maier, R. Murray, S. Keńa-Cohen, *Nat. Mater.* **2014,** 13, 271.

[54] J. D. Plumhof, T. Stöferle, L. Mai, U. Scherf, R. Mahrt, *Nat. Mater.* **2014,** 13, 247.

[55] T. Cookson, K. Georgiou, A. Zasedatelev, R. T. Grand, T. Virgili, M. Cavazzini, F. Galeotti, C. Clark, N. G. Berloff, D. G. Lidzey, P. G. Lagoudakis, *Adv. Optical Mater.* **2017,** 5, 1700203.

[56] C. P. Dietrich, A. Steude, L. Tropf, M. Schubert, N. M. Kronenberg, K. Ostermann, S. Höfling, M. C. Gather, *Sci. Adv.* **2016,** 2, e1600666.

[57] J. R. Tischler, M. S. Bradley, V. Bulović, J. H. Song, A. Nurmikko, *Phys. Rev. Lett.* **2005,** 95, 036401.

[58] G. H. Lodden, R. J. Holmes, *Appl. Phys. Lett.* **2011,** 98, 233301.

[59] N. Christogiannis, N. Somaschi, P. Michetti, D. M. Coles, P. G. Savvidis, P. G. Lagoudakis, D. G. Lidzey, *Adv. Optical Mater.* **2013,** 1, 503.

[60] C. R. Gubbin, S. A. Maier, S. Keńa-Cohen, *Appl. Phys. Lett.* **2014,** 104, 233302.

[61] S. Gambino, M. Mazzeo, A. Genco, O. D. Stefano, S. Savasta, S. Patanè, D. Ballarini, F. Mangione, G. Lerario, D. Sanvitto, G. Gigli, *ACS Photonics* **2014,** 1, 1042.

[62] M. Mazzeo, A. Genco, S. Gambino, D. Ballarini, F. Mangione, O. Di. Stefano, S. Patanè, S. Savasta, D. Sanvitto, G. Gigli, *Appl. Phys. Lett.* **2014,** 104, 233303.

[63] S. Gambino, A. Genco, G. Accorsi, O. D. Stefano, S. Savasta, S. Patanè, G. Gigli, M. Mazzeo, *Appl. Mater. Today* **2015,** 1, 33.

[64] A. Graf, M. Held, Y. Zakharko, L. Tropf, M. C. Gather, J. Zaumseil, *Nat. Mater.* **2017,** 16, 911.

[65] M. Held, A. Graf, Y. Zakharko, P. Chao, L. Tropf, M. C. Gather, J. Zaumseil, *Adv. Optical Mater.* **2018,** 6, 1700962.

Chapter 2

Light Amplification in Single Crystals of Thiophene/Phenylene Co-Oligomer Derivatives

In this chapter, optical characteristics were investigated for vapor-grown single crystal of unsubstituted and cyano-substituted thiophene/phenylene co-oligomer (TPCO) derivatives: 5,5'-bis(4-biphenylyl)-2,2'-bithiophene (BP2T), and 5,5'-bis-(4'-cyanobiphenyl-4-yl)-2,2'-bithiophene (BP2T-CN), respectively. In particular, the highest occupied and lowest unoccupied molecular orbitals (HOMO and LUMO) energies of BP2T-CN molecule were characterized as an n-type semiconductor by strong electron-withdrawing effect of the cyano groups in contrast to the p-type of unsubstituted BP2T. Optically pumped lasing based on Fabry–Pérot (F–P) resonation were observed from both BP2T and BP2T-CN crystals at room temperature owing to their efficient light confinement in the crystal cavity with high group refractive index (n_g ~5.14, ~5.20) and high quality factor (Q ~2545, ~4500). These attracted optical properties of both p- and n-type TPCO crystals are useful for constructing organic EL and laser devices using TPCO derivatives.

2.1 Introduction

Organic semiconductor materials are attracting attention in both fundamental science research and optoelectronic applications because of their light weight, low temperature manufacturing, and flexibility. Since reports on electroluminescence (EL) from organic single crystals[1] and bilayered films,[2] a number of studies have been actively conducted toward the realization of displays and light sources.[3–7] In recent years, many attempts have been carried out toward realizing an electrically pumped organic semiconductor laser from the viewpoint of both material synthesis and device structure. Compared with inorganic semiconductor lasers, organic semiconductor lasers have superior advantages because of their light weight, low temperature manufacturing and tenability of emission wavelength. In order to achieve laser oscillation, active media in which light is amplified by stimulated emission and optical resonation are necessary. Especially, thiophene/phenylene co-oligomers (TPCOs)[8–10] have a high fluorescence quantum yield at the visible light wavelength with excellent charge transport characteristics, and their emission color is easily tuned by modification into different molecular structures. So far, optically pumped lasing with TPCO single crystals has been established at room temperature owing to their efficient light confinement in the crystal cavity with high group refractive index ($n_g \sim 5.0$) and high quality factor ($Q \sim 5000$).[11–15] In addition, spectrally narrowed emission[16] and quasi-amplified emission[17] have been obtained in LEFET devices, suggesting that the TPCO crystal is one of most promising candidates for electrically pumped organic laser media.

Moreover, the p-n conduction type can be controlled by the substitution into the TPCO molecules. By introducing electron-withdrawing trifluoromethyl groups at both end of molecule, for example [1,4-bis{5-[4-(trifluoromethyl)phenyl]thiophen-2-yl}benzene, AC5-CF$_3$], the HOMO) and LUMO energies of AC5-CF$_3$ are deepened by 0.35 and 0.41 eV, respectively, compared with unsubstituted 1,4-bis(5-phenylthiophen-2-yl)benzene (AC5)
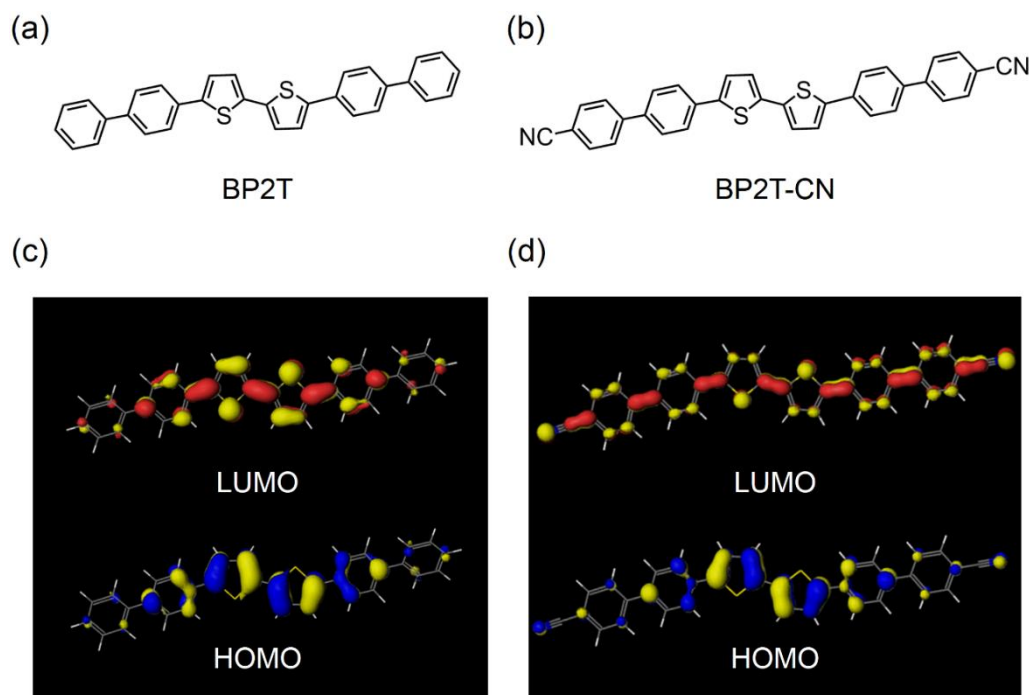
Fig. 2.1. Structural formulas of BP2T (a) and BP2T-CN (b). HOMO/LUMO of BP2T(c) and BP2T-CN (d).

molecule. Consequently, it has been reported that AC5-CF$_3$ shows an n-type conduction in light-emitting field-effect transistor (LEFET)[18–20] and heterojunction-type EL[21] devices. H. Mizuno *et al*. have reported room temperature lasing from single crystals of 2,5-bis(4'-cyanobiphenyl-4-yl)thiophene (BP1T-CN) which is a new candidate of n-type TPCO owing to the stronger electron-withdrawing cyano group.[22] By calculations using density functional theory (DFT), the HOMO and LUMO energies of BP1T-CN are deepened by 0.48 and 0.65 eV, respectively, with respect to those of unsubstituted 2,5-bis(4-biphenylyl)thiophene (BP1T).

For developing electrically pumped organic lasers, the combination of both p- and n-type conduction properties with excellent optical and electrical characteristics is required. In this chapter, for further exploration of TPCO derivatives with a different molecular symmetry and a longer π-electronic conjugation other than BP1T and BP1T-CN molecules, vapor-grown single crystals of p-type 5,5'-bis(4-biphenylyl)-2,2'-bithiophene [BP2T, **Fig. 2.1(a)**], and n-type 5,5'-bis-(4'-cyanobiphenyl-4-yl)-2,2'-bithiophene [BP2T-CN, **Fig. 2.1(b)**] were prepared,

and their optical characteristics were investigated. These molecules have the *zigzag* conformation with the point group of C_{2h}. The calculated HOMO and LUMO belong to the symmetry species of B_g and A_u, respectively, as shown in **Figs. 2.1(c)** and **(d)** by DFT calculations using a Material Studio DMol^3 program. Moreover, the HOMO/LUMO energies of BP2T (−4.86/−2.71 eV) and BP2T-CN (−5.25/−3.21 eV) were estimated, and the combination of these molecules is favorable toward constructing heterojunction-type organic EL devices.

2.2   Experimental Section

Sample preparation:

The HOMO and LUMO energies of BP2T and BP2T-CN molecule were calculated by DFT using Material Studio DMol^3 program. BP2T powder (97%) purchased from Sigma-Aldrich was subjected to purification by sublimation two times at 300°C while BP2T-CN powder (~99.9%) purchased from Sumitomo Seika Chemicals was used without further purification. Crystallization of BP2T and BP2T-CN was performed by physical vapor transport (PVT) method. 3 mg powder was heated at 285°C for BP2T and 305°C for BP2T-CN, respectively, in the tube oven (Koyo Thermo Systems KTF030N) purged with a N_2 gas at pressure of 100 mmHg. These temperatures were kept for 24 h. After cooling to 27°C in 7 h, both crystals were precipitated in the downstream of the heated tube wall according to the temperature gradient in the tube. These crystals were transferred onto a quartz substrate using a tungsten needle.

Sample characterization and optical measurement:

Morphology and fluorescence image of obtained crystals were observed using a fluorescence microscope (Olympus BX51) with a 10× objective lens and a charge-coupled
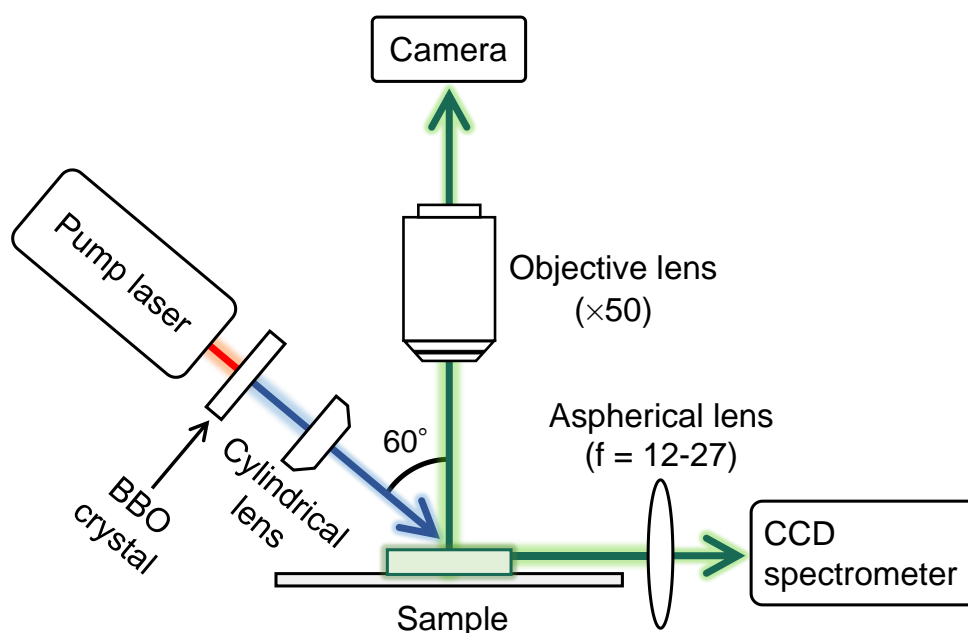
Fig. 2.2. Schematic diagram of high-density optical excitation PL measurement setup.

device (CCD) camera (Olympus DP21) under ultraviolet excitation (λ_{ex} = 365 nm). A multichannel spectrometer (Hamamatsu Photonics PMA-12) equipped in the fluorescence microscope and a UV/Vis spectrophotometer (Jasco V-530) were used for optical absorption and photoluminescence (PL) measurements. The crystal thicknesses were determined using a surface profiler (Kosaka Laboratory ET200). XRD measurements of the BP2T-CN single crystal were carried out at −150 °C by using a Micro Crystal X-ray Structure Analysis (Rigaku VariMax RAPID RA-Micro7HFM). Intensity data were collected using the ω-scan technique with Mo-Kα radiation (λ = 0.71075 Å) as an X-ray source and were corrected for usual Lorentz polarization effects. High-density optical excitation PL measurements were carried out with a excitation source of a second harmonics from a Ti:sapphire femtosecond optical amplifier ($\lambda_{2\omega}$ = 397 nm, pulse width: ~200 fs, repetition rate: 1 kHz) at room temperature in air. A stripe shaped excitation beam (spot size: 130 μm in length, 100 μm in width) was incident on the crystal surface with an angle of 60° (**Fig. 2.2**). The excitation power was varied by using two rotatable gradient neutral density (ND) filters. The emitted light was collected in the direction

parallel to the crystal plane with a liquid-N_2-cooled CCD spectrometer (Roper Scientific ST-133 series) equipped with gratings of 300 and 1800 gr/mm.

2.3 Results and Discussion

The obtained BP2T and BP2T-CN single crystals are shown in **Figures 2.3(a)** and **(b)**, respectively. BP2T crystals are grown in plate-like morphology with a size of ~3 mm. In contrast to the BP2T, the crystal of BP2T-CN grow typically small and rod-like, while some plate-like crystals with a size of ~200 μm are also found. The thicknesses of both rod-like and platelet single crystals were determined to be 1−3 μm using a surface profiler.

For BP2T single crystals, green fluorescence was exhibited at the crystal edges indicating that the emitted light is confined inside the crystal slab and waveguided along its plane. The XRD analysis of the BP2T single crystal reports that the molecules are packed in a monoclinic from with unit cell parameters of $P2_1/c$, $a = 5.7081$, $b = 7.6036$, $c = 52.465$ Å, $\beta = 97.147°$, $Z = 4$ [23] as shown in **Fig. 2.4**. The basal face of the crystal corresponds to the (002) plane and the molecular axis is standing against the crystal ab-plane. Since the π-electronic transition dipole moment between the HOMO and LUMO is parallel to the molecular axis, the emitted light dominantly propagates by transverse magnetic (TM) mode in the planar crystal. Therefore, PL spectra of the BP2T single crystal was collected from the crystal edge direction.

Figure 2.3(c) shows fluorescence and absorption spectra of the BP2T single crystal. The fluorescence spectrum of the vapor-grown BP2T crystal indicates emission peaks at 526.7 and 560.7 nm along with shoulder at around 600 nm which are assigned 0−1, 0−2, and 0−3 vibronic progressions of the $\pi-\pi^*$ transition, respectively. The 0−0 transition is basically prohibited due to the selection rule for the H aggregate which the total of transition dipole moments at the lowest excited states with antiparallel exciton coupling of the dipoles are canceled out as same as other TPCO single crystals.[24,25] This emission suffers from absorption and scattering during
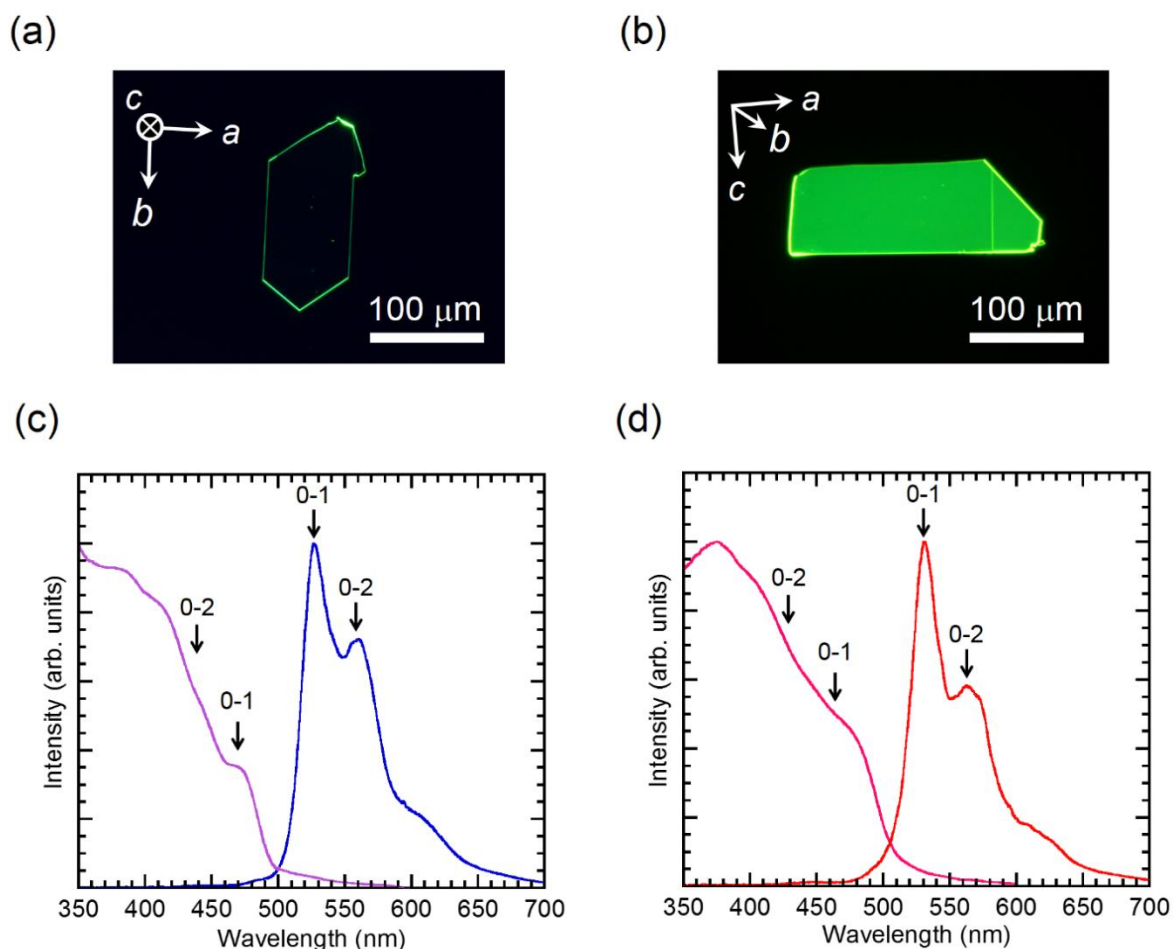
Fig. 2.3. Fluorescence micrographs of single-crystal BP2T (a) and BP2T-CN (b) under UV excitation. Fluorescence (blue and red line) and absorption (purple and pink line) spectra of BP2T (c) and BP2T-CN (d) crystals.

propagation in the crystal resulting in quenching of the shorter-wavelength side as shown in the absorption spectrum [**Fig. 2.3(c)**].

In contrast to the BP2T crystal, surface emission is observed from the single crystal of BP2T-CN as depicted in **Fig. 2.3(b)**. This factor can be explained from XRD measurements as well as the BP2T single crystal. **Fig. 2.5** shows the crystal structure of BP2T-CN determined by the XRD analysis in this study. The BP2T-CN molecules are crystalized in a monoclinic from with lattice parameters of $P2_1$, a = 18.3994, b = 7.2397, c = 18.4431 Å, β = 100.572°, Z = 4. The figure indicates that the molecules align parallel to the ac-plane and are piled up orienting in almost same direction. The basal face of the BP2T-CN single crystal is
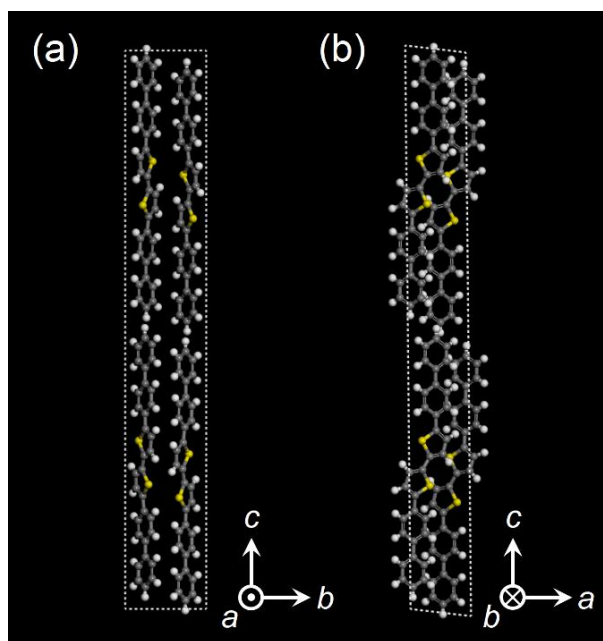
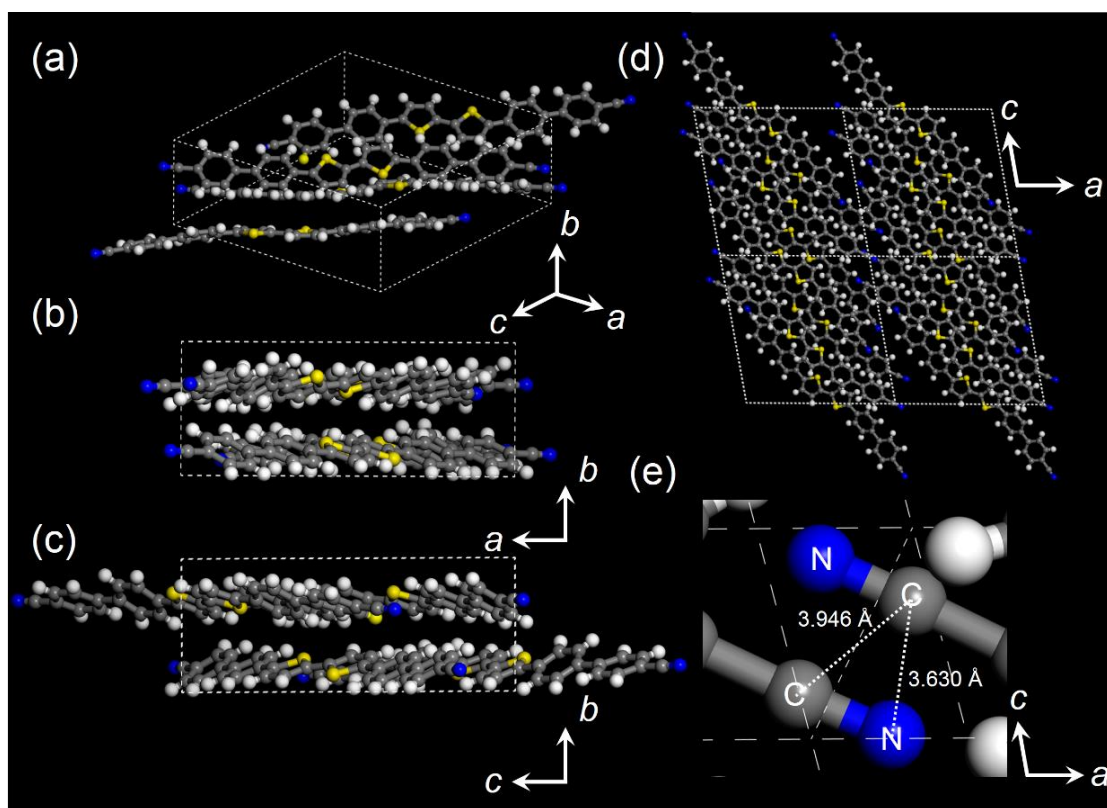*Fig. 2.4. Crystal structure of BP2T with unit-cell projections on the bc-plane (a) and ac-plane (b).*

Fig. 2.5. Molecular packing in the unit cell of BP2T-CN crystal. (a) Three-dimensional molecular packing (a). Projections on the ab- (d), bc- (c), and ac-plane (d). (e) Enlarged crystal structure showing atomic distances between carbon and nitrogen of cyano gropes.
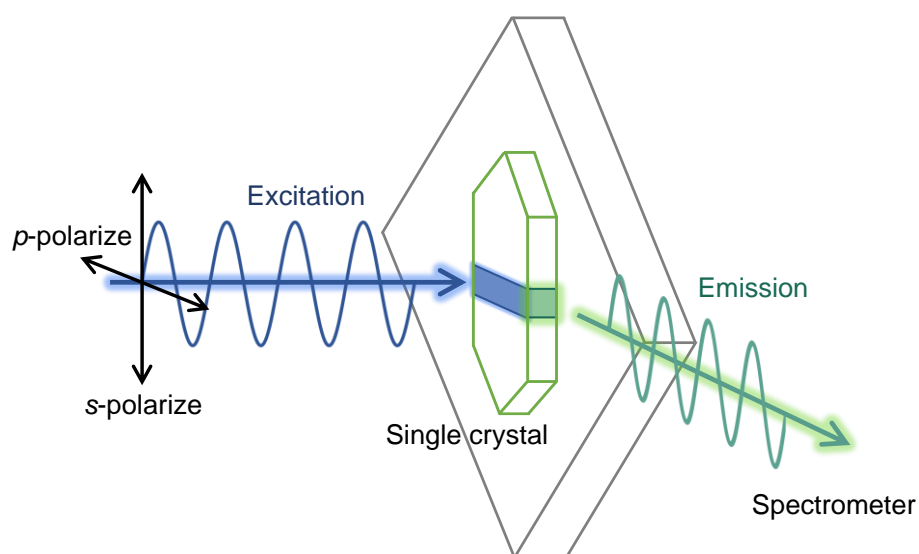
Fig. 2.6. Schematic representation of optical measurement setup. Single crystals of BP2T and BP2T-CN were excited by p- and s-polarized laser beam, respectively.

assigned to the (201) plane, and emitted light with the transverse electric (TE) mode propagates along the in-plane direction. Therefore, this lying molecular orientation results in effective surface emission from the crystal surface. As shown in **Fig. 2.5(e)**, the minimum distance between the carbon and nitrogen atoms in the cyano groups is 3.630 Å. This unique packing is caused by Coulomb interaction between the carbon and nitrogen atoms with positive and negative electron charge, respectively, in the two cyano groups of the neighboring molecules as in the case reported for the BP1T-CN single crystal.[15] The fluorescence spectrum of the BP2T-CN single crystal indicates red-shifted emissions at 530.6, 563.1, and 605.0 nm corresponding to the 0–1, 0–2, and 0–3 transitions, respectively as shown in **Fig. 2.3(d)**.

Next, high-density optical excitation PL measurements of both single crystals were performed using fs-pulsed excitation. As depicted in **Fig. 2.6**, p- and s-polarized excitation beam was incident to the crystal surface of BP2T and BP2T-CN, respectively, so that the standing and lying molecules can be optically excited. The stripe-shaped beam was irradiated in the direction perpendicular to the parallel pair of side facets of the crystal. **Figures 2.7(a)–(d)** show their PL spectra and excitation density dependence of integrated PL intensities of 0–1
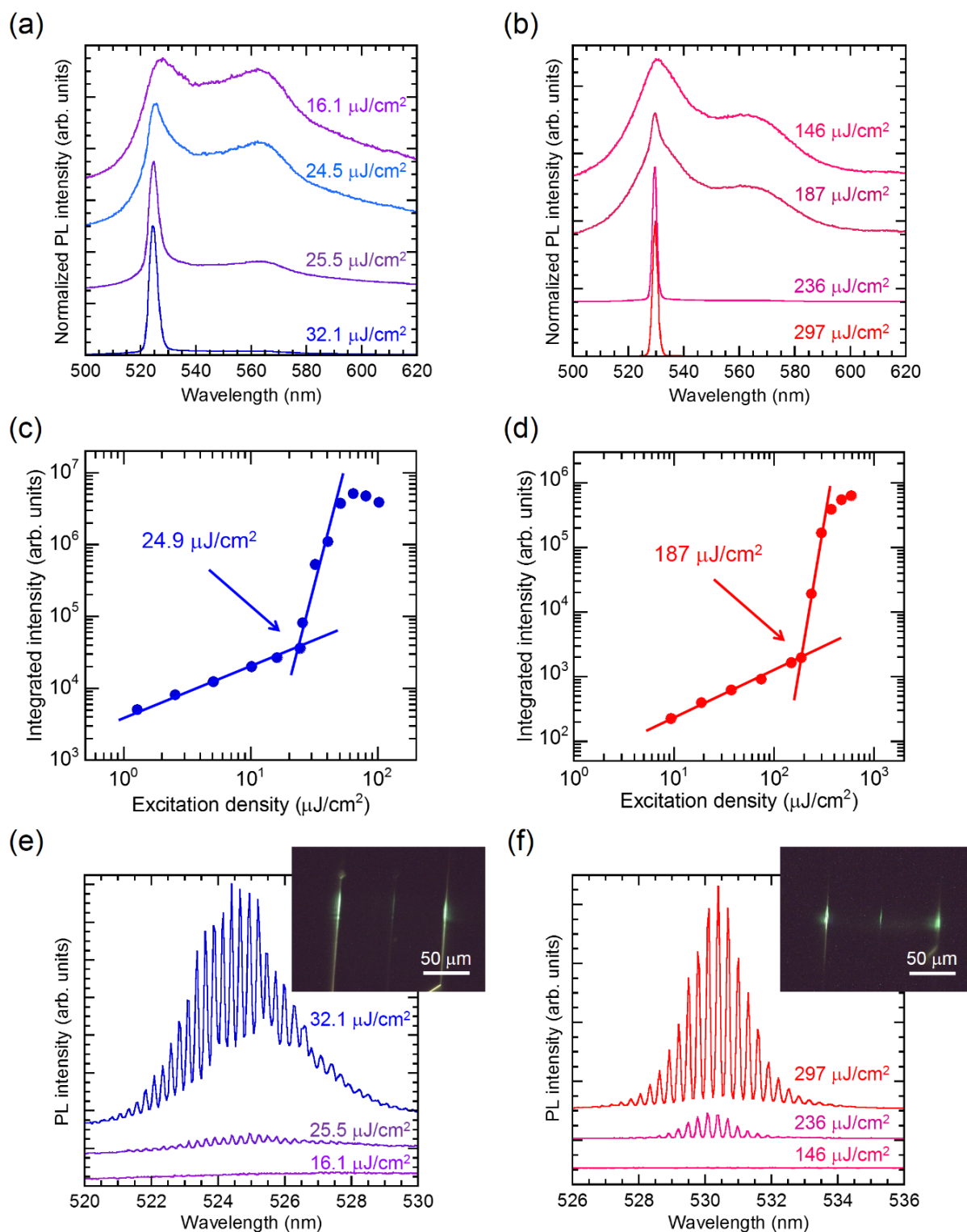
Fig. 2.7. Normalized PL spectra taken from single crystals of BP2T (a) and BP2T-CN (b) as a function of excitation density. Integrated intensities of the 0−1 band in (a) and (b) plotted as a function of excitation density for single crystals of BP2T (c) and BP2T-CN (d). Excitation density dependences of high-resolution PL spectra for single crystals of BP2T (e) and BP2T-CN (f) at the 0−1 band shown in (a) and (b). The insets show photograph of light emission from single crystals of BP2T and BP2T-CN taken above threshold excitation.

band. In weak excitation density below certain thresholds, both crystals indicate broad emission band of 0−1 and 0−2 bands as same as their fluorescence spectra [**Figs. 2.3(c)** and **(d)**]. As the excitation density is increased to 24.9 μJ/cm^2 for BP2T and 187 μJ/cm^2 for BP2T-CN, respectively, their 0−1 bands are gain-narrowed and their integrated intensity increases nonlinearly.

Figures 2.7(e) and **(f)** show high resolution PL spectra (spectral resolution: 0.04 nm) of the 0−1 bands of BP2T and BP2T-CN crystals, respectively. Above their thresholds, multimode lasing oscillations are clearly observed from both crystals indicating that the pair of parallel crystal side facets works as a F−P resonator. The insets of micrographs of both BP2T and BP2T-CN crystals exhibit light emissions at the side facets of the crystals. The frequency interval ($\Delta\nu$) and full width at half maximum (FWHM) of their lasing modes are evaluated to be 9.7 cm^{-1} and 0.17 nm for BP2T and 10.2 cm^{-1} and 0.12 nm for BP2T-CN, respectively. The group refractive index (n_g) in those crystal active media is evaluated by the following equation: [26]

$$n_g = 1/2L\Delta\nu \qquad (2.1)$$

where L is the cavity length that is the distance between a pair of the parallel crystal facets. The calculated n_g of the BP2T and BP2T-CN crystal is ~5.14 and ~5.20, respectively. The Q factor is estimated to be 2545 for the BP2T crystal and 4500 for the BP2T-CN crystal from the $\Delta\nu$ and the FWHM of the F−P lasing peaks.

These results, such as lower threshold F−P lasing, high n_g and Q factor for both BP2T and BP2T-CN single crystals, have shown a comparable or higher performance as lasing media compared with previous reports[11−15,27]. Since the BP2T-CN is crystalized in a platelet form in which the molecular axis is lying, it can be considered that the emitted light has a component in the surface direction in addition to the observed F−P mode. This surface emission and the lower n_g of the BP2T-CN crystal probably cause the higher lasing threshold in the F−P lasing

compared to the BP2T crystal. In other words, the BP2T-CN single crystal with lying molecular orientation has a potential as the vertical cavity surface emitting laser (VCSEL) other than the F–P mode laser.

2.4   Conclusions

Vapor-grown single crystals of BP2T and BP2T-CN were characterized as p- and n-type semiconductors, respectively. Especially, the XRD analysis revealed that the molecular axes of BP2T-CN oriented lying parallel to the crystal plane. Optically pumped multimode lasing was achieved for both BP2T and BP2T-CN crystals at room temperature owing to the self-cavity effect with high n_g and high Q factor and the formation of F–P resonators by parallel side facets of the crystal. These results indicate that the BP2T and BP2T-CN molecules have attractive optical properties, and are expected to be good candidates toward applications to p-n heterojunction-type organic EL devices.

References

[1] M. Pope, H. P. Kallmann, P. Magnante, *J. Chem. Phys.* **1963,** 38, 2042.

[2] C. W. Tang, S. A. VanSlyke, *Appl. Phys. Lett.* **1987,** 51, 913.

[3] C. Adachi, M. A. Baldo, M. E. Thompson, S. R. Forrest, *J. Appl. Phys.* **2001,** 90, 5048.

[4] H. Uoyama, K. Goushi, K. Shizu, H. Nomura, C. Adachi, *Nature* **2012,** 492, 234.

[5] T. Sekitani, H. Nakajima, H. Maeda, T. Fukushima, T. Aida, K. Hata, T. Someya, *Nat. Mater.* **2009,** 8, 494.

[6] T. Han, Y. Lee, M. Choi, S. Woo, S. Bae, B. H. Hong, J. Ahn, T. Lee, *Nat. Photonics* **2012,** 6, 105.

[7] S. Hotta, S. A. Lee, T. Tamaki, *J. Heterocycl. Chem.* **2000,** 37, 281.

[8] A. Sandström, H. F. Dam, F. C. Krebs, L. Edman, *Nat. Commun*. **2012,** 3, 1002.

[9] S. Hotta, T. Katagiri, *J. Heterocycl. Chem.* **2003,** 40, 845.

[10] T. Katagiri, S. Ota, T. Ohira, T. Yamao, S. Hotta, *J. Heterocycl. Chem.* **2007,** 44, 853.

[11] M. Ichikawa, R. Hibino, M. Inoue, T. Haritani, S. Hotta, K. Araki, T. Koyama, Y. Taniguchi, *Adv. Mater.* **2005,** 17, 2073.

[12] T. Yamao, K, Yamamoto, Y. Taniguchi, T. Miki, S. Hotta, *J. Appl. Phys.* **2008,** 103, 09315.

[13] H. Mizuno, I. Ohnishi, H. Yanagi, F. Sasaki, S. Hotta, *Adv. Mater.* **2012,** 24, 2404.

[14] H. Mizuno, U. Haku, Y. Marutani, A. Ishizumi, H. Yanagi, F. Sasaki, S. Hotta, *Adv. Mater.* **2012,** 24, 5744.

[15] H. Mizuno, T. Maeda, H. Yanagi, H. Katsuki, M. Aresti, F. Quochi, M. Saba, A. Mura, G. Bongiovanni, F. Sasaki, S. Hotta, *Adv. Optical Mater.* **2014,** 2, 529.

[16] T. Yamao, K. Terasaki, Y. Shimizu, S. Hotta, *J. Nanosci. Nanotechnol.* **2010,** 10, 1017.

[17] S. Z. Bisri, T. Takenobu, Y. Yomogida, H. Shimotani, T. Yamao, S. Hotta, Y. Iwasa, *Adv. Funct. Mater.* **2009,** 19, 1728.

[18] S. Hotta, Y. Shimizu, T. Yamao, M. Goto, R. Azumi, *Chem. Lett.* **2009,** 38, 294.

[19] W. Hayashi, K. Terasaki, K. Kajiwara, T. Yamao, S. Hotta, *Jpn. J. Appl. Phys.* **2012,** 51, 08HF06.

[20] T. Yamao, Y. Shimizu, H. Kuriki, T. Katagiri, S. Hotta, *Jpn. J. Appl. Phys.* **2010,** 49, 01AB01.

[21] T. Sengoku, T. Yamao, S. Hotta, *J. Non-Cryst. Solids* **2011,** 358, 2525.

[22] H. Mizuno, T. Maeda, H. Yanagi, H. Katsuki, M. Aresti, F. Quochi, M. Saba, A. Mura, G. Bongiovanni, F. Sasaki, S. Hotta, *Adv. Optical Mater.* **2014,** 2, 529.

[23] S. Hotta, M. Goto, R. Azumi, M. Inoue, M. Ichikawa, Y. Taniguchi, *Chem. Mater.* **2004,** 16, 237.

[24] K. Bando, T. Nakamura, Y. Masumoto, F. Sasaki, S. Kobayashi, S. Hotta, *J. Appl. Phys.* **2006,** 99, 013518.

[25] K. Bando, T. Nakamura, S. Fujiwara, Y. Masumoto, F. Sasaki, S. Kobayashi, Y. Shimoi, S. Hotta, *Phys. Rev. B* **2008,** 77, 045205.

[26] T. Yamao, Y. Okuda, Y. Makino, S. Hotta, *J. Appl. Phys.* **2011,** 110, 053113.

[27] J. Gierschner, S. Varghese, S. Y. Park, *Adv. Optical Mater.* **2016,** 4, 348.

Chapter 3

Organic Electroluminescence Devices with Thiophene/Phenylene Co-Oligomer Derivatives

In Chapter 2, single crystals of TPCO derivatives were demonstrated as promising media from the optical characteristics. In this Chapter, organic EL devices with vapor-deposited films of those TPCO derivatives are investigated.

In Section 3.1, EL devices were fabricated by p-n heterojunction of using BP2T and BP2T-CN. Al:Li/BP2T-CN/BP2T/ITO devices were examined using vapor-deposited films, and their doping effect was examined by co-deposition of MoO_3 and Cs_2CO_3 into the BP2T and BP2T-CN, respectively. Strong electron-withdrawing cyano-groups in BP2T-CN changes the p-type of BP2T into n-type. Moreover, the current density and EL intensity were significantly increased by carrier doping with MoO_3 and Cs_2CO_3 into the BP2T and BP2T-CN films, respectively. However, PL and EL from their bilayered films dominantly result from the BP2T-CN layer since the lying molecular orientation of BP2T-CN facilitates surface emission, while the standing orientation of BP2T is not suitable for the device configuration.

In order to solve this problem, improvement of device structure was carried out in Section 3.2. Two types of EL devices, Al:Li/BP2T-CN/BP2T/ITO and Au/BP2T/BP2T-CN/ITO were fabricated using vapor-deposited films BP2T and BP2T-CN by changing the deposition order onto the ITO/glass substrate. The EL performance was significantly improved for the latter device in which the two molecules had lying orientation suitable for efficient carrier injection and transport as well as surface emission.

In Section 3.3, aiming at optimization of the device structure which enable to allocate carrier transport and exciton accumulation regions to the respective layers, p-i-n double-heterojunction type EL devices were fabricated by adding an active layer of 5'''-bis(4-trifluoromethylphenyl)[2,2';5',2'';5'',2''']quaterthiophene (P4T-CF$_3$). As designed from their expected frontier orbital energies, electroluminescence was obtained from the P4T-CF$_3$ layer. When the BP2T layer was first deposited on ITO/glass substrate, the device (Al:Li/BP2T-CN/P4T-CF$_3$/BP2T/ITO) showed homogeneous EL. On the other hand, the device having opposite deposition order (Au/BP2T/P4T-CF$_3$/BP2T-CN/ITO) showed dotted EL with higher efficiency at lower bias voltages. By decreasing deposition rate of the P4T-CF$_3$ layer in the latter device, its morphological change resulted in homogeneous EL with increased density of dotted emission. Towards organic lasing for the future work, single-crystal P4T-CF$_3$ was prepared by liquid phase growth for the i-layer. Thin rhombus-shaped crystals of P4T-CF$_3$ exhibited amplified spontaneous emission under optical excitation.

Section 3.1

Fabrication of p-n Heterojunction EL Devices and Doping Effect on EL Characteristics

3.1.1　Introduction

Towards electrical pumped organic lasing, the development of highly emissive organic molecules having both p- and n-type semiconducting properties is necessary for p-n heterojunction-type organic EL devices. In Chapter 2, optical characteristics of vapor-grown single crystals of TPCO derivatives were investigated. Optically pumped lasing with BP2T and BP2T-CN single crystals were observed at room temperature owing to their efficient light confinement in the crystal cavity with high group refractive index and high quality factor. These results indicate that BP2T and BP2T-CN crystals have a promising potential as p- and n-type gain medium for an electrically pumped organic semiconductor laser.

In this Section, p-n heterojunction-type organic EL devices were fabricated by bilayered vacuum-deposited films of BP2T and BP2T-CN. Semiconducting properties of those materials were evaluated by photoelectron yield spectroscopy (PYS) and molecular orbital calculations. Thin film structure and molecular orientation were investigated by the X-ray diffraction and PL spectroscopy to discuss EL behaviors of the heterojunction device.

In order to increase their EL characteristics, doping techniques for organic semiconductor layers[1,2] is effective to reduce the carrier injection barrier and improve carrier mobility by controlling their electronic characteristics. When an acceptor molecule is doped to an organic semiconductor molecule, the electron transfer to the dopant is formed at the ground state results in p-type conduction. On the other hand, by doping of a donor molecule into an organic semiconductor results in n-type. Conduction-type control of fullerene (C_{60}) films to p- and n-

type have been demonstrated by co-deposition doping of MoO_3[3] and Cs_2CO_3[4], respectively. Kelvin vibrating capacitor measurements reported that the Fermi level (E_F) of C_{60} (−4.60 eV) shifted to −5.88 and −4.40 eV by p- and n- doping, respectively, at a concentration of 3300 ppm (3.6%). Moreover, these doping phenomena by means of extreme-UV excited photoelectron spectroscopy (EUPS) have also been observed for TPCOs.[5] The E_F of BP1T doped with MoO_3 (2%) was shifted from −4.0 to −4.3 eV and that of AC5-CF$_3$ doped with Cs_2CO_3 (2%) was shifted from −4.8 to −3.9 eV. In the present study, this doping effect has been examined by co-deposition of MoO_3 and Cs_2CO_3 into the BP2T and BP2T-CN layers, respectively.

3.1.2   Experimental Section

Device fabrication and EL measurements:

Heterojunction-type organic EL devices were fabricated by bilayered vapor-deposited films of BP2T and BP2T-CN. **Figure 3.1** shows a schematic of the device structure and molecular structures of BP2T and BP2T-CN. A glass substrate (20×20 mm^2) coated with stripe-shaped patterns (3×18 mm^2, 150 nm-thick) of indium-tin-oxide (ITO) was used as an anode. After ultrasonic cleaning in neutral detergent, acetone and methanol for 15, 15 and 30 min, respectively, the substrate surface was treated with UV-ozone exposure for 20 min. On this ITO/glass substrate, BP2T was first vapor-deposited from a resistively-heated quartz crucible in a vacuum of ~2.0×10^{-4} Pa. Then, BP2T-CN was vapor-deposited as well successively without breaking the vacuum. The deposition rate and film thicknesses of each layers were adjusted to ~0.5 Å/s and 100 nm, respectively, by monitoring with a quartz microbalance. Finally, stripe-shaped cathodes (3×18mm^2, 50 nm-thick) of Al-Li alloy (99:1) was deposited so as to be orthogonally across the ITO anode beneath the BP2T-CN/BP2T film. The thickness of each deposited layer was measured by a surface profiler (Kosaka Laboratory
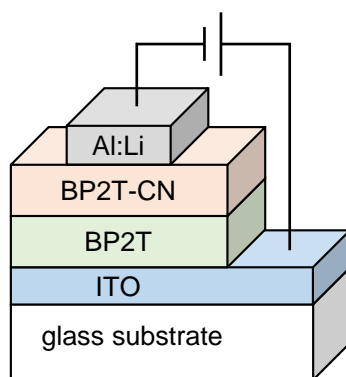
Fig. 3.1. Schematic diagram for the fabricated organic EL device.

ET200). In order to investigate the doping effects into BP2T/BP2T-CN layers, MoO_3 and Cs_2CO_3 were co-deposited as p- and n-dopant materials, respectively. In this study, both dopant concentration was set at 1% due to their low sublimation rate even at high temperature. The resulting devices were set up in an evacuated glass chamber (~1.0×10^3 Pa), and current-voltage characteristics were measured with a source-measure unit (Agilent B2902A). EL spectra were recorded with a CCD spectrometer (Hamamatsu Photonics PMA-12) from the back side of the ITO/glass substrate.

Characterizations:

For the purpose of exploring molecular p- and n-type semiconducting abilities, the HOMO and LUMO of BP2T and BP2T-CN were estimated. Ionization potentials of BP2T and BP2T-CN films vapor-deposited on ITO/glass substrates were measured by photoelectron yield spectroscopy in air (Riken Keiki AC-3). Their LUMO energies were experimentally estimated from optical band gaps by measuring their absorption and fluorescence spectra using a UV/Vis spectrophotometer (Jasco V-530) and a fluorescence microscope (Olympus BX51) equipped with a CCD spectrometer (Hamamatsu Photonics PMA-12), respectively. Surface morphology of those films was observed with an atomic force microscope (Seiko Instruments SPA400) by tapping mode. In order to investigate crystalline structure and molecular orientation in those

50

films, X-ray diffraction (XRD) measurements were performed in $\theta/2\theta$ scans using a X-ray diffractometer (Rigaku RINT-TTIII/NM).

3.1.3　Results and Discussion

Figures 3.2 and **3.3** show AFM images and PL spectra, respectively, of the BP2T, BP2T-CN and BP2T/BP2T-CN films. Their film thicknesses were estimated to be 140, 140 and 260 nm, respectively. All these films are composed of fine grains with a size of 0.2−0.3 μm. Their average surface roughness is 5.79, 5.16 and 11.6 nm for the BP2T, BP2T-CN and BP2T/BP2T-CN films, respectively, showing that these films are homogeneously deposited and their surfaces are flat. The PL spectrum of the BP2T film shows emission peaks at 539 and 582 nm which are assigned to the 0−1 and 0−2 vibronic progressions, respectively, of the HOMO-LUMO transition. Weak emissions observed at 490 and 635 nm are attributed to the 0−0 and 0−3 transitions, respectively. For the BP2T-CN film, the 0−0, 0−1, 0−2 and 0−3 transitions appear at 500, 559, 594, and 660 nm, respectively. Their peak positions of both vapor-deposited BP2T and BP2T-CN films shift to the longer wavelength side as compared to those of single crystals having *H* aggregate-like molecular alignment [**Fig. 2.3(c)** and **(d)**].[6,7] Note that the PL intensity of the BP2T-CN film is about 63 times higher than that of the BP2T film, despite their film thicknesses are controlled to be same. According to this enhanced PL intensity of the BP2T-CN film, the PL spectrum of the bilayered BP2T/BP2T-CN film resembles that of the BP2T-CN film. However, the emission intensity of the BP2T/BP2T-CN film is significantly lower than that of the BP2T-CN film, the reason of which will be discussed later.

Figure 3.4(a) shows current-voltage characteristics of organic EL devices fabricated with the undoped and doped BP2T-CN/BP2T films. These devices show rectifying *I−V* characteristics where the currents increase under positive biases application to the ITO anode. When each BP2T and BP2T-CN layer is doped with 1% MoO_3 and Cs_2CO_3, respectively, the
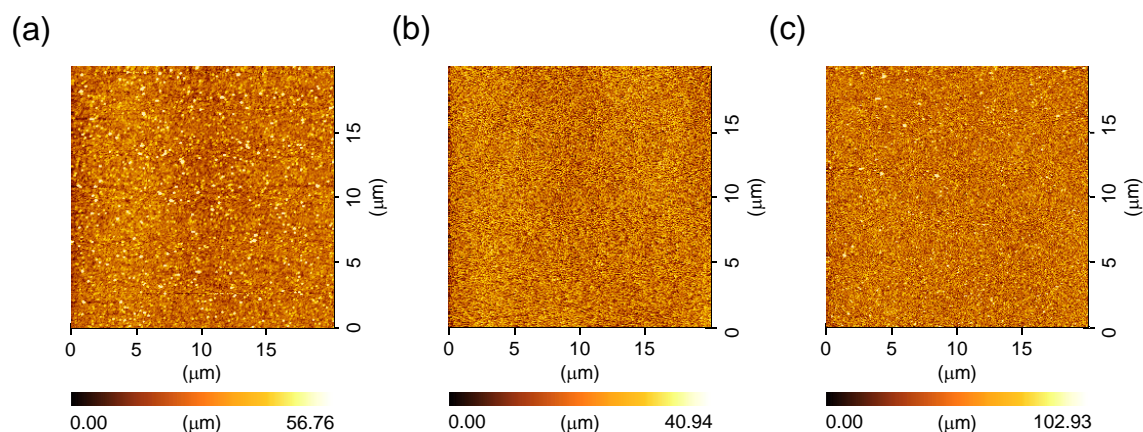
51

(a)   (b)   (c)

Fig. 3.2. AFM images taken from (a) BP2T (140 nm), (b) BP2T-CN (140 nm) and (c) BP2T-CN/BP2T (130/130 nm) films vapor-deposited on ITO/glass substrate.
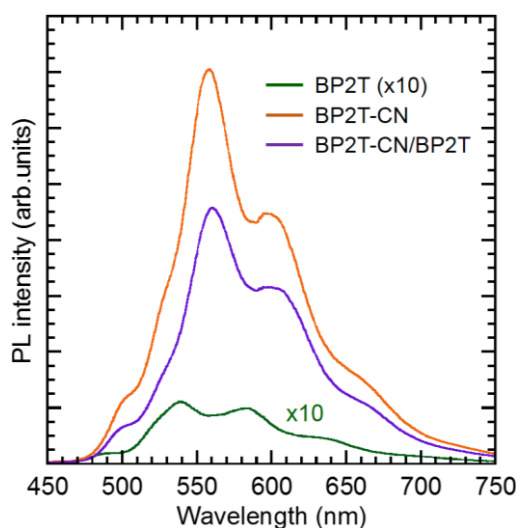

Fig. 3.3. PL spectra taken from BP2T (140 nm, green), BP2T-CN (140 nm, orange) and BP2T-CN/BP2T (130/130 nm, purple) films vapor-deposited on ITO/glass substrate.

current density considerably increased 15 times as high as that of the undoped device at 25 V.

During their *I−V* measurements, EL was observed from the backside of the ITO/glass substrate

when the voltage is increased beyond 15 V for the undoped device. This EL onset voltage is

decreased to around 10 V for the doped device. **Figure 3.4(b)** shows a comparison of EL

spectra for those doped and undoped devices operated at 25 V. As shown in the inset images,

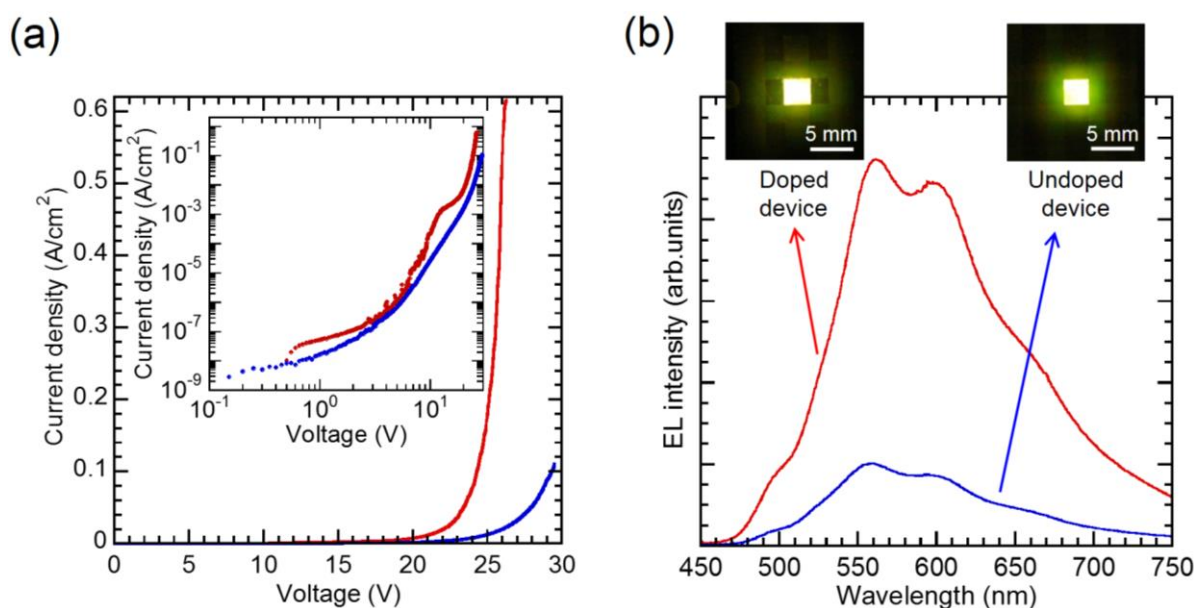green emissions are visible at the active area of orthogonally crossed ITO and Al:Li

Fig. 3.4. (a) Current−voltage characteristics of organic EL devices with undoped BP2T-CN/BP2T film (blue) and doped BP2T-CN/BP2T film with 1% MoO₃/Cs₂CO₃ (red). The inset shows logarithmic plot. (b) EL spectra of EL devices with undoped BP2T-CN/BP2T film (blue) and doped BP2T-CN/BP2T film with 1% MoO₃/Cs₂CO₃ (red). The insets show photographs of EL from both devices.

electrodes. Both devices show identical EL spectra having emission peaks at around 560 and 596 nm. These emission bands are consistent with the 0−1 and 0−2 transitions observed in the PL spectrum of the BP2T-CN film (**Fig. 3.3**). According to the current increase in **Fig. 3.4(b)**, the EL intensity of the doped device is about 4.5 times higher than that of the undoped device.

The rectifying *I−V* and EL results observed for organic EL devices using bilayered BP2T/BP2T-CN films demonstrate that the cyano-substituted BP2T-CN functions as n-type and forms a heterojunction with the p-type BP2T. In order to examine HOMO/LUMO energies of BP2T and BP2T-CN, PYS measurements of each films were performed. As a result, photoelectrons are emitted when the UV excitation energy is beyond 5.40 eV for the BP2T film, and 5.94 eV for the BP2T-CN film as shown in **Figs. 3.5(a)** and **(b)**. **Figure 3.5(c)** shows absorption spectra of the BP2T and BP2T-CN films. The absorption spectrum of the BP2T film shows absorption peak at 461.5 and 426.0 nm which are assigned to the 0−1 and 0−2
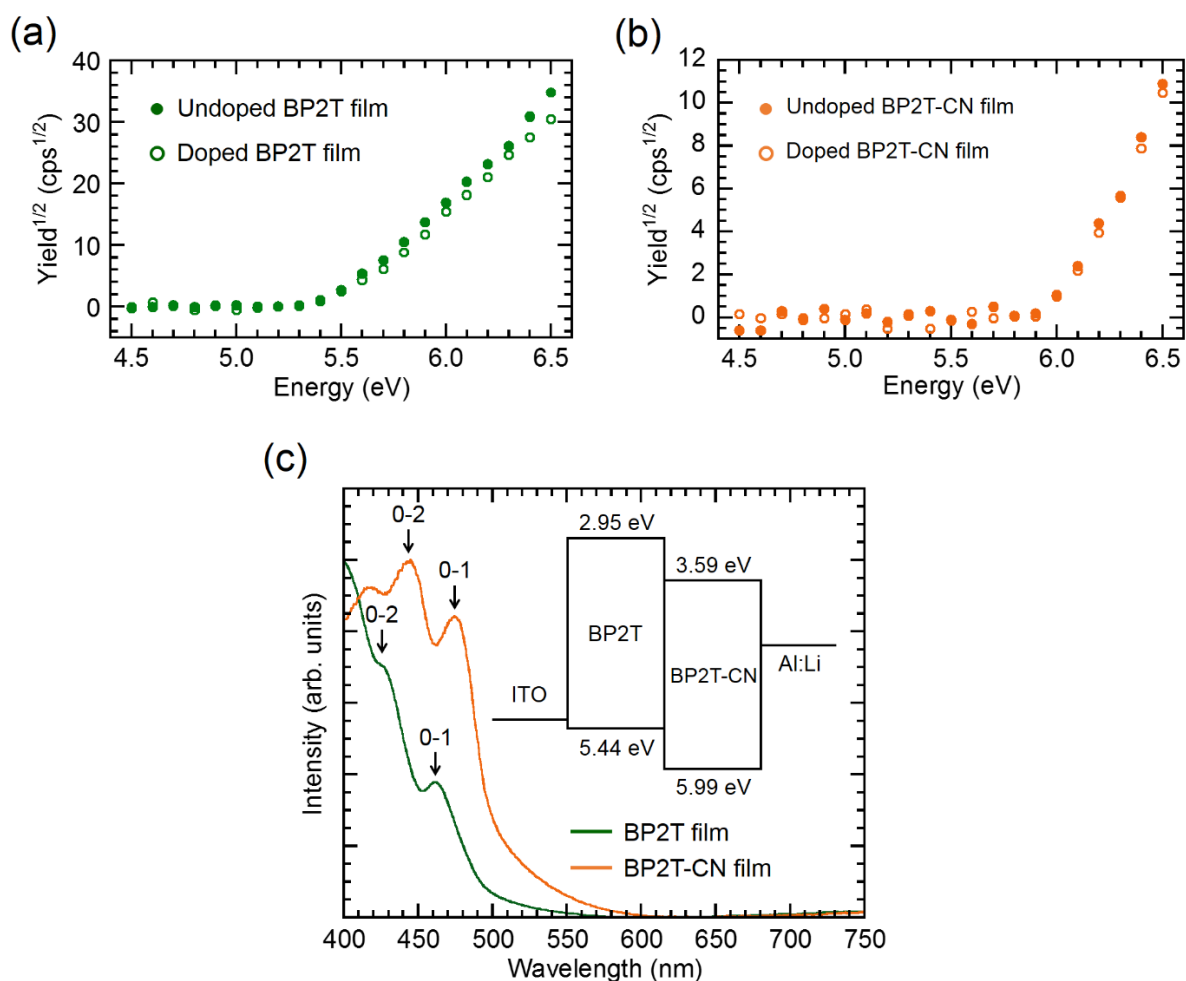
Fig. 3.5. Photoelectron yield plots of BP2T (a) and BP2T-CN (b) films vapor-deposited on ITO substrate. The open and closed circles indicate plots for undoped and doped films, respectively. (c) Absorption spectra of BP2T (green) and BP2T-CN (orange) films on ITO substrate. The inset shows estimated energy diagram of the BP2T/BP2T-CN device.

vibronic progressions. For the BP2T-CN film, corresponding 0−1 and 0−2 vibronic progressions appear at 475.0 and 446.5 nm. From measurements of these absorption and PL spectra, the optical band gaps for the BP2T and BP2T-CN films were estimated to be 2.49 and 2.42 eV, respectively. Consequently, the energy band diagram of the BP2T-CN/BP2T heterojunction is approximately depicted as shown in the inset of **Fig. 3.5(b)**. It reveals that the HOMO and LUMO energies of cyano-substituted BP2T-CN are lower by 0.55 eV and 0.64 eV respectively, than those of BP2T. These energy changes due to molecular modification were confirmed by DFT calculations as mentioned in Chapter 2. The HOMO/LUMO energies of

BP2T and BP2T-CN were calculated to be −4.86/−2.71 eV and −5.25/−3.21 eV, respectively.

As mentioned above, the doping into the BP2T-CN/BP2T film considerably improved $I−V$ characteristics and EL intensity as compared with the undoped film. When each BP2T and BP2T-CN layers were doped with 1% MoO_3 and 1% Cs_2CO_3, respectively, there was no apparent change in their onset energies in the PYS measurements: 5.44 eV for the doped BP2T and 5.99 eV for the doped BP2T-CN film, as shown in **Figs. 3.5(a)** and **(b)**. The EL spectra of the doped device was also as same as that of the undoped device. These results suggest that their HOMO/LUMO energies are not modulated, but the carrier density increased by doping.

The EL spectrum of the BP2T-CN/BP2T device was similar to the PL spectrum of the BP2T-CN layer, suggesting that luminescent recombination dominantly occurred in the BP2T-CN film. Due to the higher electron barrier (0.64 eV) at the BP2T-CN/BP2T interface, the electrons injected from the Al:Li cathode accumulate in the BP2T-CN layer and recombine with the holes transported from the BP2T layer. Moreover, another reason is also considered for the dominant luminescence from the BP2T-CN layer. In **Fig. 3.3**, the PL intensity of the BP2T-CN film is about 63 times higher than of the BP2T film despite their film thicknesses are the same. Furthermore, the PL intensity of the bilayered BP2T/BP2T-CN film is lower than that of the BP2T-CN film. These results suggest that their luminescence intensities depend on differences in molecular orientations in the BP2T and BP2T-CN films.

As shown in **Fig. 3.6**, XRD measurements were performed for the BP2T, BP2T-CN and BP2T-CN/BP2T films vapor-deposited on the ITO/glass substrate. For the BP2T film, a strong diffraction peak is observed at 3.16° corresponding to the spacing of $d = 2.79$ nm. According to the crystal structure of BP2T (monoclinic, $P2_1/c$, $a = 0.571$, $b = 0.760$, $c = 5.287$ nm, $\beta = 97.1°$),[8] this peak is assigned to the (002) plane, suggesting that the molecular axis of BP2T is almost perpendicular to the substrate surface. For the BP2T-CN film, on the other hand, weak diffraction peak is observed at 23.7° corresponding to the spacing $d = 0.38$ nm which is
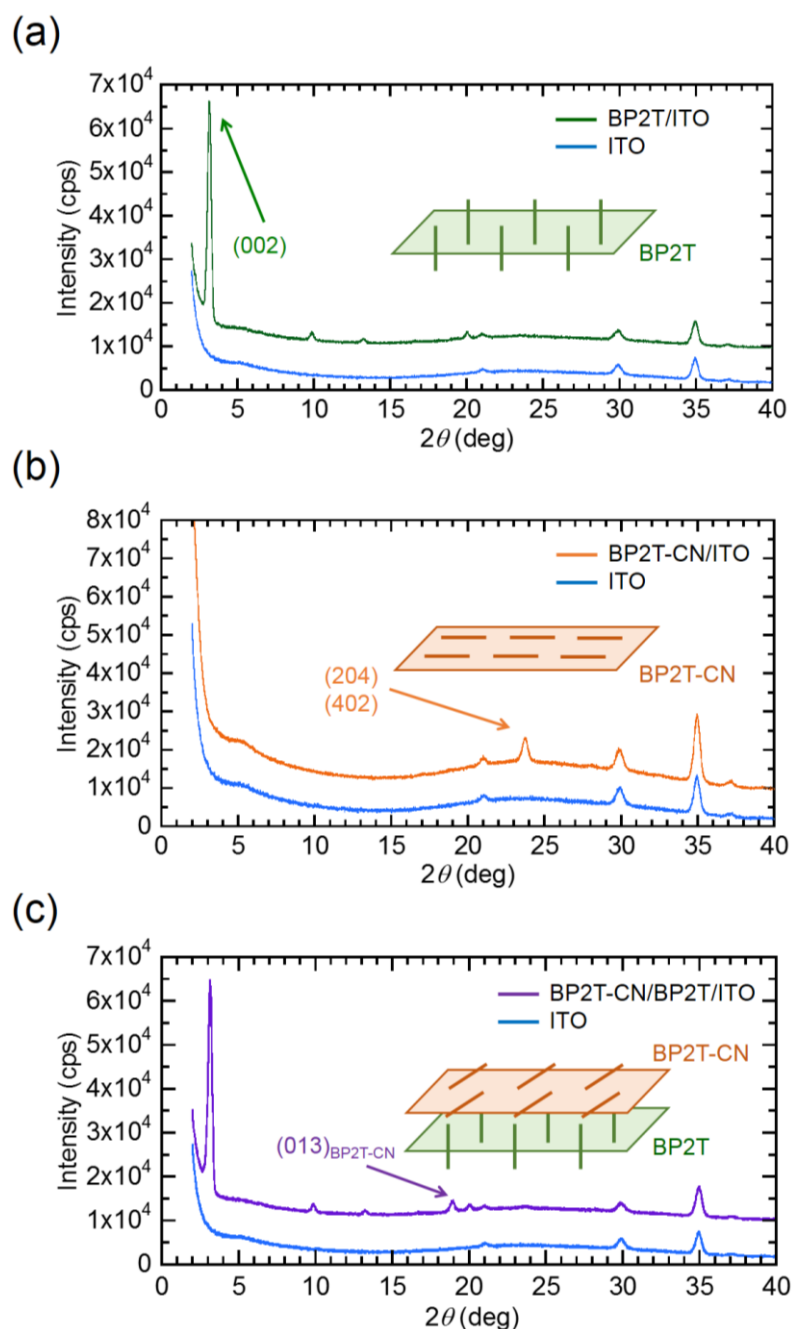
Fig. 3.6. XRD patterns of BP2T (100 nm) (a), BP2T-CN (100 nm) (b), and BP2T-CN/BP2T (100/100 nm) (c) films vapor-deposited on ITO/glass substrate. XRD patterns of ITO are indicated as reference. The insets show schematic diagrams for molecular orientation in each films.

assigned to the (204) or (402) planes. In these crystal planes, the molecular axes of BP2T-CN are lying with an angle less than 20° with respect to the substrate surface according to the crystal structure of BP2T-CN (monoclinic, $P2_1$, $a = 1.834$, $b = 0.724$, $c = 1.8446$ nm, $\beta =$

100.5°). Since the HOMO/LUMO transition dipole moment of BP2T and BP2T-CN are parallel to the molecular axis, the standing molecular orientation in the BP2T film results in weak surface-emitting luminescence while the lying orientation in the BP2T-CN film is favorable for the surface emission. The XRD pattern of the bilayered BP2T-CN/BP2T film exhibits a diffraction peak at 18.9° in addition to the (002) plane of the standing BP2T. This peak is assigned to the (013) plane of the BP2T-CN crystal in which the molecular axis of BP2T-CN makes an angle of 25° against the substrate surface. Although possibility of a non-emissive exciplex formation[9] and a charge separation at the BP2T-CN/BP2T interface are also considered, this oblique orientation of BP2T-CN in the film deposited on the BP2T film results in lower PL intensity than in the single-layered BP2T-CN film in which the molecules are lying with smaller angles. Nevertheless, the obliquely lying orientation of BP2T-CN deposited on the BP2T film results in the EL spectrum resembling to the PL spectrum of the BP2T-CN film due to higher surface-emitting intensity from the BP2T-CN layer than from the BP2T layer.

3.1.4   Conclusions

Heterojunction-type organic EL devices using BP2T and its cyano-substituted derivative, BP2T-CN, were fabricated, and their EL characteristics in relation to the film structure in each layers were examined. Since rectifying $I-V$ curves and EL were observed when applying negative voltages to the Al:Li/BP2T-CN cathode, it demonstrated that the BP2T-CN layer functioned as n-type. XRD measurements revealed that the molecular axes were standing almost perpendicular in the BP2T layer while they were obliquely lying in the BP2T-CN layer deposited on top of the BP2T layer. Due to this different molecular orientation, the surface-emission from the BP2T-CN film dominated the EL characteristics of the device. When the BP2T and BP2T-CN films were chemically doped, the current density and EL intensity were significantly increased. However, the EL intensity was still low at 4 cd/m^2 even for the doped

EL devices at 26.5 V. It was probably due to the microcrystalline structure and standing molecular orientation in the BP2T layer which deteriorated the carrier transport and light-emitting recombination in the device.

Section 3.2

Improved Electroluminescence Devices with Reversed Bilayers of Thiophene/Phenylene Co-Oligomer Derivatives

3.2.1 Introduction

In the previous Section, p-n heterojunction EL devices using vapor-deposited films of BP2T and BP2T-CN were investigated. It was concluded that BP2T-CN was characterized as n-type from the rectifying *I−V* curves and EL was observed when a positive voltage was applied to this anode. The PYS measurements indicated that the substitution with strong electron-withdrawing cyano groups in BP2T-CN changed the p-type of BP2T to n-type. Optically pumped edge-emitting F−P Lasing was confirmed for both BP2T and BP2T-CN crystals in Chapter 2. These studies have revealed that the cyano-substituted TPCOs crystallize in a unique structure in which the molecular axes are parallel to the crystal plane. This is in marked contrast to other TPCOs in which the molecular axes are standing. It has been found that such a lying orientation is also predominant in the BP2T-CN film vapor-deposited on top of the standing BP2T film deposited onto ITO electrode. This lying BP2T-CN film is favorable for surface-emitting EL and vertical cavity laser devices. Indeed, the electroluminescence dominantly resulted from the BP2T-CN layer in the EL device.

Recently, the importance of the thin film state has increasingly attracted attention for organic devices. A number of studies on organic EL devices have revealed a marked influence of the molecular orientation.[10−14] Moreover, ionization potential (IP) of organic films depends on molecular orientation and packing structure.[15−17] This section describes that the deposition

59

order of p-type BP2T and n-type BP2T-CN remarkably affects their molecular orientation and HOMO/LUMO energies. Consequently, the EL performance is considerably improved by making both lying bilayered p-n junction TPCO films in the reversed bilayer structure of BP2T/BP2T-CN films.

3.2.2   Experimental Section

Device fabrication:

Figure 3.7 shows cross-sectional schematics for two types of heterojunction-type EL devices: Al:Li (99:1)/BP2T-CN/BP2T/ITO (device A) and Au/BP2T/BP2T-CN/ITO (device B). The device A used in Section 3.1 was fabricated as reference sample for the reversed device B in this Section. Glass substrates (20×20 mm^2) coated with a stripe pattern (3×18 mm^2, 150 nm-thick) of ITO were used. The substrates were cleaned with a neutral detergent, pure water, and isopropyl alcohol for 5, 15, and 15 min, respectively, in an ultrasonic bath. This substrate was exposed to UV ozone for 20 min for the device A, but not for the device B since it was known that this exposure lowers the work function of ITO due to surface oxidation.[18] In the device A, p-type BP2T and n-type BP2T-CN were successively vapor-deposited in this order on the ITO substrate from a resistively heated quartz crucible under a vacuum of ~2.0×10^{-4} Pa, whereas the deposition order was reversed in the device B. The deposition rate and film thickness of each layer were held at ~0.5 Å/s and 150 nm, respectively, by monitoring with a quartz oscillator. The deposited thickness was confirmed with a surface profiler (Kosaka Laboratory ET200). Next, striped metal electrodes (3×18 mm^2, 50 nm-thickness) of Al:Li (as a cathode) in the device A and Au (as an anode) in the device B were vacuum-deposited under a vacuum of ~2.0×10^{-4} Pa such that this top electrode was orthogonally across the ITO electrode underneath the organic active layer.

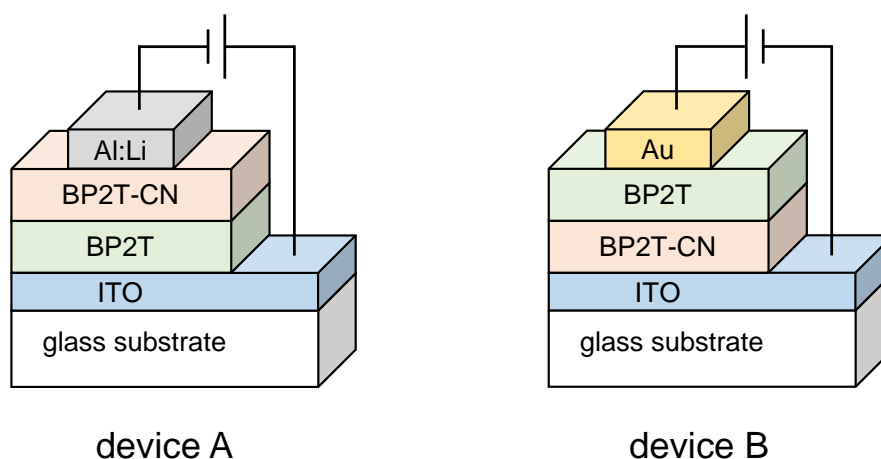<center>device A   device B</center>

<center>*Fig. 3.7. Schematic representations for fabricated organic EL devices.*</center>

Device characterizations:

The surface morphology, the crystalline structure, photoelectron spectra, and PL spectra for these films and electrical characteristics for both EL devices were described in Section 3.1. In addition to these characterizations, luminance of both EL devices was recorded from the normal of the substrate surface with a luminance meter (TOPCON BM-8).

3.2.3 Results and Discussion

Figure 3.8 displays AFM images of single-layered BP2T, single-layered BP2T-CN, bilayered BP2T-CN/BP2T (BP2T-CN deposited on BP2T/ITO/glass), and bilayered BP2T/BP2T-CN (BP2T deposited on BP2T-CN/ITO/glass) films. The film thicknesses were controlled to be 150 nm for the single-layer films and 150/150 nm for the bilayered films. These thicknesses were confirmed with a surface profiler. **Figure 3.9** indicates PL spectra of those films taken under UV excitation at $\lambda_{ex} = 365$ nm. All the films consist of very small fine grains are homogeneously formed and their surfaces are flat. Their grain sizes are 269, 121, 125, and 242 nm and their average surface roughnesses are 7.2, 11, 20, and 7.6 nm, respectively, for the BP2T, BP2T-CN, BP2T-CN/BP2T, and BP2T/BP2T-CN films. The PL spectrum for the single-layered BP2T film shows emission peaks at around 539, 582, and 635 nm, which are assigned

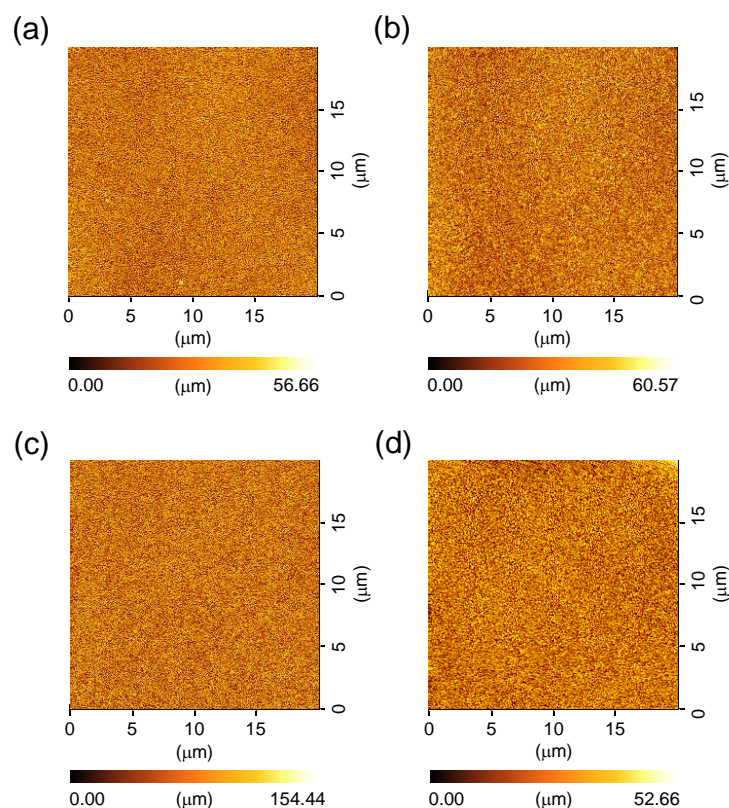<center>61</center>

(a)

(b)

(c)

(d)

Fig. 3.8. AFM images taken from (a) BP2T (150 nm), (b) BP2T-CN (150 nm) (c) BP2T-CN/BP2T (150/150 nm), and (d) BP2T/BP2T-CN (150/150 nm) films vapor-deposited on ITO/glass substrate.
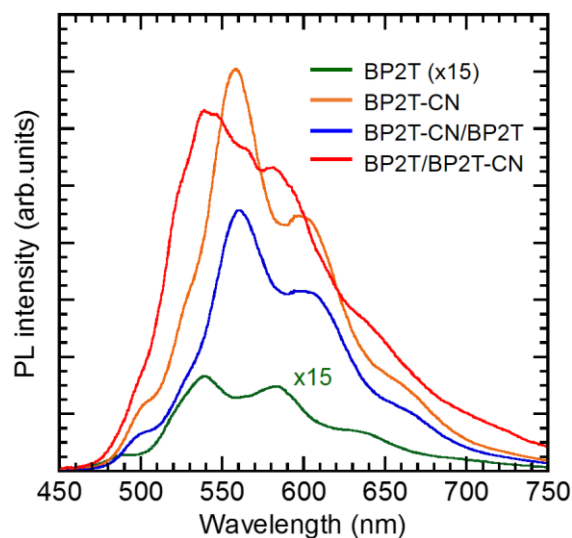
Fig. 3.9. PL spectra taken from BP2T (150 nm, green), BP2T-CN (150 nm, orange), BP2T-CN/BP2T (150/150 nm, blue), and BP2T/BP2T-CN (150/150 nm, red) films vapor-deposited on ITO/glass substrate.

to the 0−1, 0−2, and 0−3 vibronic progressions of the $\pi-\pi^*$ transition, respectively. Similarly, the single-layered BP2T-CN film shows the 0−1, 0−2, and 0−3 transitions at around 559, 595, and 659 nm, respectively. These peaks are shifted to longer wavelengths than those of the single-layered BP2T film. The PL spectrum of the bilayered BP2T-CN/BP2T film is almost consistent with that of the single-layered BP2T-CN film. On the other hand, that of the bilayered BP2T/BP2T-CN film resembles superposed normalized spectra of the single-layered BP2T and BP2T-CN films. The comparison of the single-layered BP2T and BP2T-CN film indicates that the PL intensity of the BP2T-CN film is about 60 times higher than that of the BP2T film, despite their film thicknesses being the same. The PL intensity of the bilayered BP2T/BP2T-CN is higher than that of the bilayered BP2T-CN/BP2T, but its peak intensity is lower than that of the single-layered BP2T-CN film.

These differences in PL intensity could be explained by their molecular orientation in vapor-deposited films onto the ITO substrate. The XRD measurements in the previous Section demonstrated that the molecular axis of BP2T is standing almost perpendicular to the substrate surface in the BP2T film while the BP2T-CN molecules is parallel to the substrate surface in the of BP2T-CN film. Thus, the PL intensity of the single-layered BP2T-CN film is about 60 times higher than that of the BP2T film since the lying BP2T-CN orientation is preferable for efficient surface emission.

By contrast, the XRD pattern of the bilayered BP2T-CN/BP2T film presented in Section 3.1 indicated that the BP2T-CN molecules obliquely lie on top of the standing BP2T film, in contrast to the single-layered BP2T-CN film as shown in **Fig. 3.10(a)**. This oblique orientation of BP2T-CN against the film/substrate plane is not suitable for surface emission from the EL device since the HOMO-LUMO transition dipole moments of the BP2T and BP2T-CN molecules are parallel to the molecular axis. On the other hand, the XRD pattern of the bilayered BP2T/BP2T-CN film indicates a diffraction peak at 21.1° in addition to the (204) or
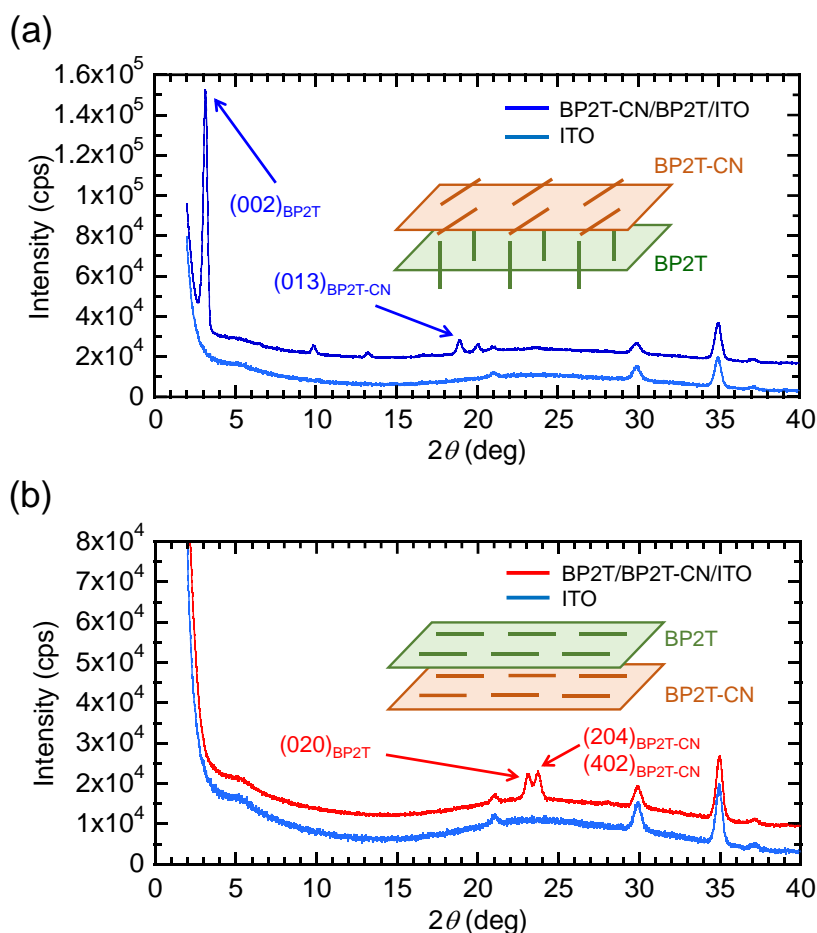
63

Fig. 3.10. XRD patterns of BP2T/BP2T-CN (150/150 nm) (a), and BP2T/BP2T-CN (150/150 nm) (b) films vapor-deposited on ITO/glass substrate. XRD patterns of ITO are indicated as reference. The insets show schematic representations for molecular orientation in each films.

(402) peak of the parallelly lying BP2T-CN film, as depicted in **Fig. 3.10(b)**. Since this peak is

assigned to the (020) plane of the BP2T crystal, it is considered that the BP2T molecules also

lie parallel on top of the BP2T-CN film. In this reversed BP2T/BP2T-CN film, surface emission

is efficiently obtained from both BP2T and BP2T-CN films because both types of molecules

are lying on the substrate. This lying orientation is suitable for surface-emitting EL

performance.

$I-V$ characteristics of fabricated EL devices are shown in **Fig. 3.11(a)**. The rectifying

currents increase when the forward bias is applied to the bottom ITO electrode for the device

A while the top Au anode is forward-biased for the device B. Compared with the device A, the
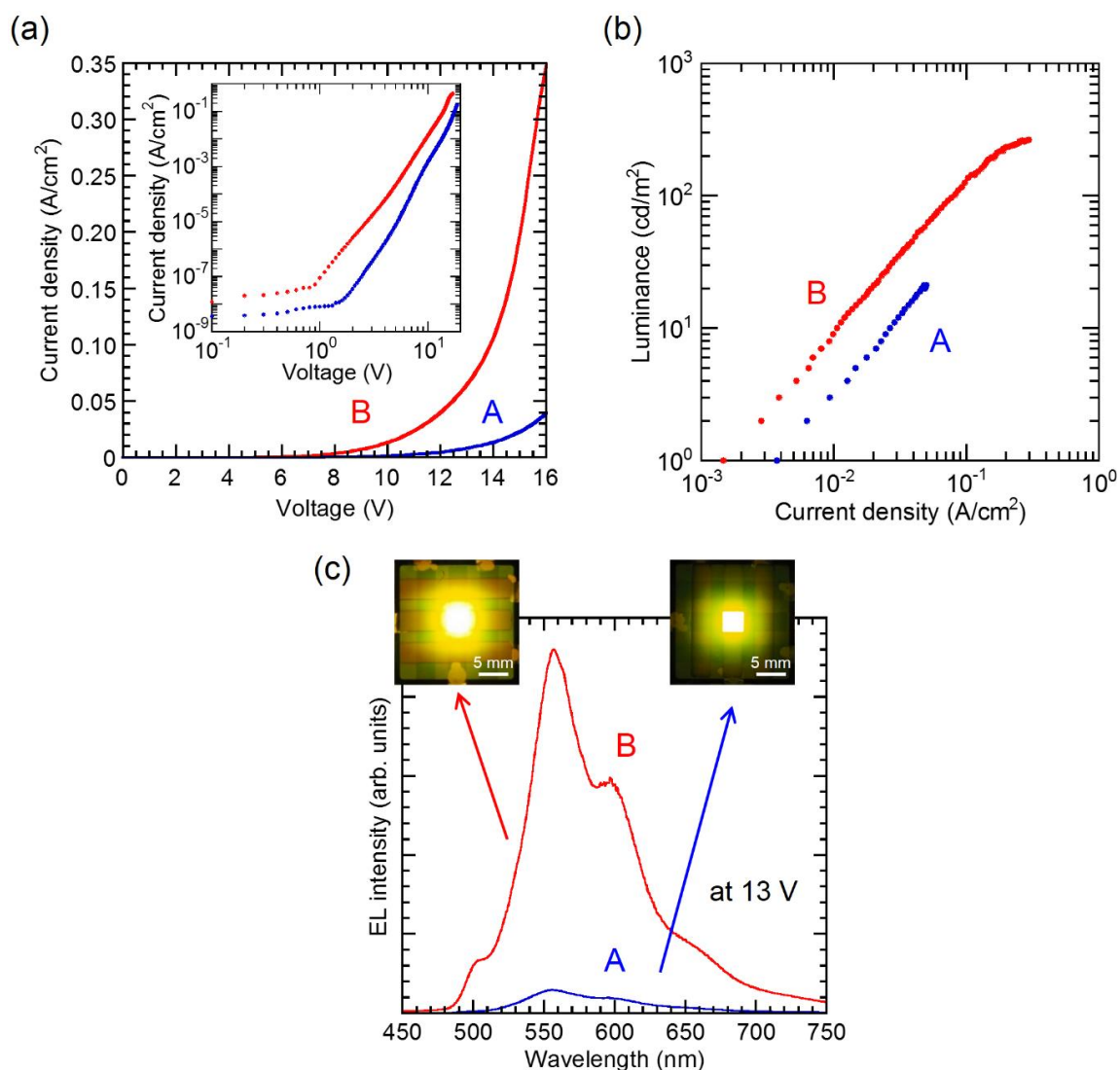
Fig. 3.11. (a) Current-voltage characteristics of device A (Al:Li/BP2T-CN/BP2T/ITO, blue) and device B (Au/BP2T/BP2T-CN/ITO, red). The inset shows their double logarithmic plots. (b) Luminance-current characteristics of device A (blue) and device B (red). (c) EL spectra of device A (blue) and device B (red) at 13 V. The insets show photographs of EL from each device.

current density of the device B increases greatly more than 6.8 times as high as that of the device A above 13 V. In these $I-V$ measurements, light emissions were observed from the orthogonally crossed area of top/bottom electrodes for devices A and B above 8.5 and 6 V, respectively. **Figure 3.11(b)** displays EL spectra and photographs of devices A and B at 13 V. Both devices show identical EL spectra with emission peaks at around 559 and 595 nm. These EL spectra are consistent with the PL spectral feature of the single-layered BP2T-CN film (**Fig.**

3.9). Note that the EL intensity of the device B is about 17 times higher than that of the device A. As shown in current-luminance characteristics in **Fig. 3.11(c)**, the maximum luminance value of the device B (783 cd/m^2 at 503.5 mA/cm^2) is considerably improved as compared with that of the device A (28 cd/m^2 at 47.9 mA/cm^2). From the obtained rectifying $I-V$ characteristics and EL emission, it is concluded that a heterojunction is formed between the p-type BP2T and n-type BP2T-CN in the bilayered BP2T-CN/BP2T and BP2T/BP2T-CN devices. Moreover, the $I-V$ characteristics are significantly improved by the device B owing to improved carrier injection and transport in those bilayered films with molecules lying on the substrate. In the current-luminance characteristics [**Fig. 3.11(b)**], the deviation from the ideal straight line in the high-voltage range is probably due to the reduced emission efficiency caused by heating and exciton quenching by injected carriers at the high electric field.

The observed EL spectra for the two EL devices are consistent with the PL spectra of the single-layered BP2T-CN film, indicating that the light emission is caused by carrier recombination in the BP2T-CN layer. **Figure 3.12** shows an energy band diagram for the EL devices. The HOMO/LUMO energies of BP2T (−4.86/−2.71 eV) and BP2T-CN (−5.25/−3.21 eV) were obtained by DFT calculations using Material Studio DMol^3 as mentioned in Chapter 2. The result indicates that the electrons injected from the ITO electrode are accumulated in the BP2T-CN layer and recombined with the holes transported from the BP2T layer since the electron barrier of LUMO (0.50 eV) is higher than the hole barrier of HOMO (0.39 eV). To further elucidate this mechanism, PYS measurements were carried out for BP2T and BP2T-CN films in different molecular orientations. **Figure 3.13** displays photoelectron spectra taken from the single-layered BP2T, single-layered BP2T-CN, bilayered BP2T-CN/BP2T, and bilayered BP2T/BP2T-CN films. When the molecular orientations changes from perpendicular to parallel on the substrate surface, the IP corresponding to the HOMO energy of the vapor-deposited BP2T film is deepened from 5.44 to 5.72 eV, respectively. In the BP2T-CN films, a
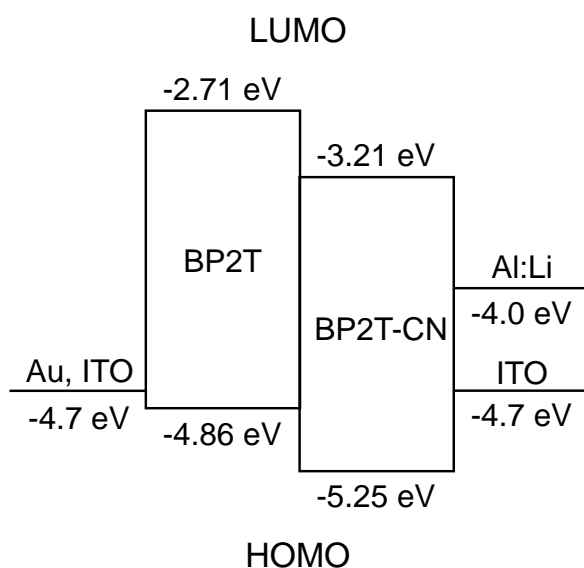
LUMO

Fig. 3.12. Energy band diagram for device A and B. HOMO/LUMO energies of BP2T and BP2T-CN were determined by DFT calculations.
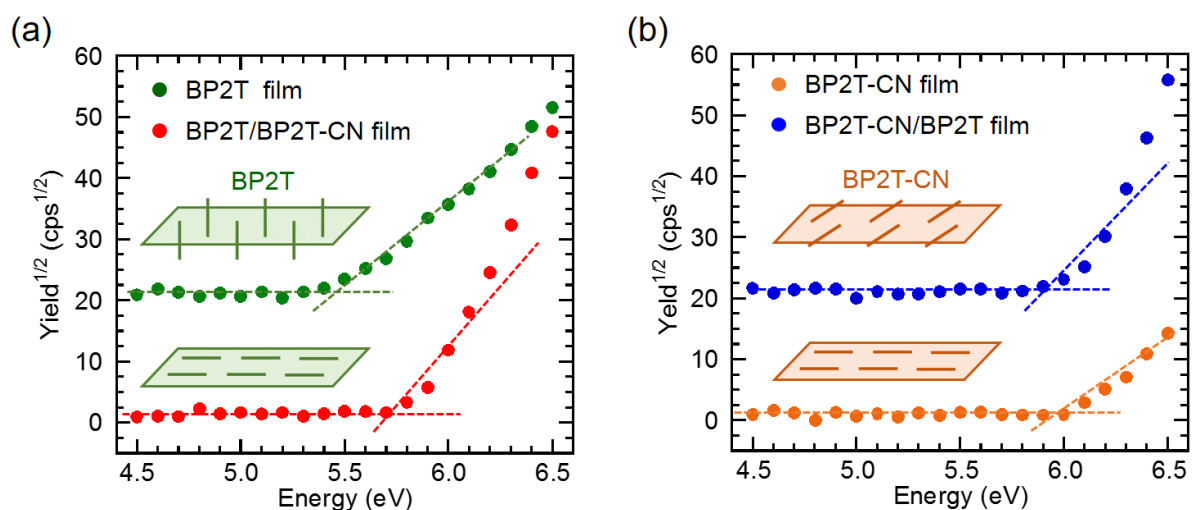

Fig. 3.13. Photoelectron yield plots of BP2T and BP2T/BP2T-CN (a) and BP2T-CN and BP2T-CN/BP2T (b) films vapor-deposited on ITO substrate. The insets show schematic representations for molecular orientation in each films.

small shift of IP is observed from 5.91 eV for obliquely lying to 5.99 eV for lying molecular orientations. Therefore, it is considered that the electron injection in the device B is improved by reduced energy barrier at the BP2T-CN/ITO interface. Moreover, the hole injection from the BP2T layer is improved by lying orientation of this film, and recombination for the BP2T-CN

layer is also promoted. In the platelet BP2T-CN single crystal, the n_g in the surface direction is higher than that in the in-plane direction as described in Chapter 2 because of molecule density for the lying molecular orientation.[19] This increased luminance of the surface emission is also ascribed to the improvement of optical confinement by lying BP2T-CN molecular orientation on the substrate. Consequently, the surface-emitting EL performance is significantly improved in the device B, owing to both lying molecular orientations of the p- and n-type TPCO derivatives which are favorable for effective carrier injection and transport.

3.2.4   Conclusions

Organic EL devices with bilayered films of TPCO derivatives which are promising as active media for organic semiconductor lasers were investigated. Two types of devices were fabricated by vapor deposition, Al:Li/BP2T-CN/BP2T/ITO (device A) and Au/BP2T/BP2T-CN/ITO (device B), by changing the deposition order of p-type BP2T and n-type BP2T-CN onto the ITO/grass substrate. Both devices exhibited rectifying $I-V$ characteristics and their EL was dominantly obtained from the surface-emitting BP2T-CN layer. Compared with the device A, the current onset and density, EL intensity, and luminance were significantly improved for the device B. The XRD measurements revealed that both BP2T and BP2T-CN molecules were lying on the substrate surface in the device B. As a result, the improved carrier injection and transport as well as surface-emitting efficiency in the device B contributed to its superior EL performance compared to the device A in which the BP2T molecules took a standing orientation. Furthermore, towards the realization of organic semiconductor lasers, the introduction of microcavity structures into the EL devices is a reburied as studied in Chapter 4.

Section 3.3

Organic Electroluminescence Devices with p-i-n Double Heterojunction of Thiophene/Phenylene Co-Oligomer Derivatives

3.3.1 Introduction

In the previous Section, p-n heterojunction type EL devices were fabricated using vapor-deposited films of TPCO derivatives, BP2T as p-type and BP2T-CN as n-type, and EL was observed from the surface-emitting BP2T-CN layer. Moreover, the deposition order of BP2T and BP2T-CN markedly affected their current density and EL intensity. When the BP2T-CN was first deposited onto the ITO/glass substrate then the BP2T layer was deposited, both molecules oriented preferably lying on the substrate. This molecular orientation improved carrier injection and transport as well as surface-emitting efficiency. However, EL intensity was rolled off when the applied voltage was elevated, probably due to exciton quenching by injected carriers at high current density in the present bilayered p-n structure. Therefore, the device structure having heterojunctions which enable to allocate carrier transport and exciton accumulation regions to the respective layers[20–24] should be optimized.

For this purpose in this section, double-heterojunction type organic EL devices with multi-layered p-i-n structure were fabricated by adding an active layer of 5'''-bis(4-trifluoromethylphe nyl)[2,2';5',2'';5'',2''']quaterthiophene [P4T-CF$_3$, **Fig. 3.14**]. P4T-CF$_3$ has a narrow bandgap and a lower HOMO/LUMO energies due to the quaterthiophene chain and the strong electron-withdrawing effect of trifluoromethyl groups.[25,26] As studied in the previous p-n device, the influence of p-n deposition order on their molecular orientation and EL
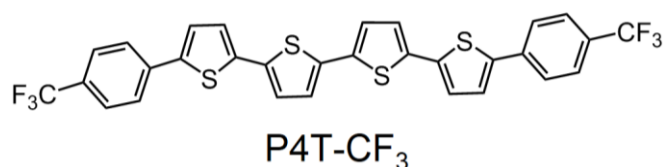
Fig. 3.14. Chemical structures of P4T-CF₃ molecule.

performances are important. The deposition rate of P4T-CF₃ is also varied to optimize this active layer morphology. The device characteristics of organic semiconductors strongly depend on the crystallinity in thin films. Improved crystalline growth without grain boundaries and/or cracks results in better device performances. In this study, from this point of view, single crystals of P4T-CF₃ were prepared, and a preliminary p-i-n device was fabricated using this single-crystal i-layer.

3.3.2 Experimental Section

Material characterization of P4T-CF₃:

For examining molecular semiconductor type of P4T-CF₃, the HOMO and LUMO energies were estimated by DFT calculations using the Material Studio DMol^3 program. In order to determine crystal structure by XRD measurements, crystallization of P4T-CF₃ was carried out by the following method. 3 mg of P4T-CF₃ powder (~99.9%) purchased from Sumitomo Seika Chemicals was dissolved in 20 g of 1,2,4-trichlorobenzene (Nakarai Tesque) by heating at 153 °C for 1 hour. Then by cooling slowly to 40 °C in 12 hours, crystals were precipitated in the solution. After filtration, rhombus-shaped single crystals with different sizes were obtained. A well-shaped single crystal was selected, and transferred onto a quartz substrate using a tungsten needle. XRD measurements of the P4T-CF₃ single crystal were carried out with Mo-Kα radiation (λ = 0.71075 Å) at −150 °C by using a X-ray diffractometer (Rigaku VariMax RAPID RA-Micro7HFM).

Optical measurements:

Fluorescence images of P4T-CF$_3$ single crystals as well as vapor-deposited films were observed under ultraviolet excitation (λ_{ex} = 365 nm) using a fluorescence microscope (Olympus BX51) with a × 10 objective lens and a CCD camera (Olympus DP21). PL and absorption spectra for P4T-CF$_3$ single crystals were carried out as described in Section 3.1. Optically pumped PL measurements using a Ti:sapphire femtosecond optical amplifier (λ_{ex} = 397 nm, pulse width: ~200 fs, repetition rate: 1 kHz) were described in Chapter 2. The excitation beam (spot size: 130 μm in length, 120 μm in width) was incident with an angle of 60° against the sample plane. The emitted light from the crystal edge was collected in the direction parallel to the crystal plane with a liquid-N$_2$-cooled CCD spectrometer.

Device fabrication with p-i-n structure:

Two type of organic EL devices, Al:Li/BP2T-CN/P4T-CF$_3$/BP2T/ITO (device A) and Au/BP2T/P4T-CF$_3$/BP2T-CN/ITO (device B) were fabricated using vapor-deposited films of BP2T, BP2T-CN, and P4T-CF$_3$, as schematically shown in **Fig. 3.15**. A glass slide (20 × 20 mm^2) coated with a stripe pattern (3 × 18 mm^2, 150 nm-thick) of ITO was used as substrate. The ITO/glass substrate cleaning process was performed as described in Section 3.2. In the device A, p-type BP2T (100 nm), i-type P4T-CF$_3$ (100 nm), and n-type BP2T-CN (100 nm) were consecutively vapor-deposited in this order on the ITO/glass substrate with a rate of 0.5 Å/s under a vacuum of ~2.0 × 10^{-4} Pa. The device B was fabricated in the same manner but by changing the deposition order to n-i-p. Finally, metal electrodes (3 × 18 mm^2, 50 nm-thick) of Al:Li (as a cathode for the device A) or Au (as an anode for the device B) was deposited through a stainless steel shadow mask aligned orthogonally across to the ITO electrode under a vacuum under a vacuum of ~2.0 × 10^{-4} Pa. The surface morphology, the crystalline structure, and PL spectra for these films and electrical characteristics for both EL devices were carried
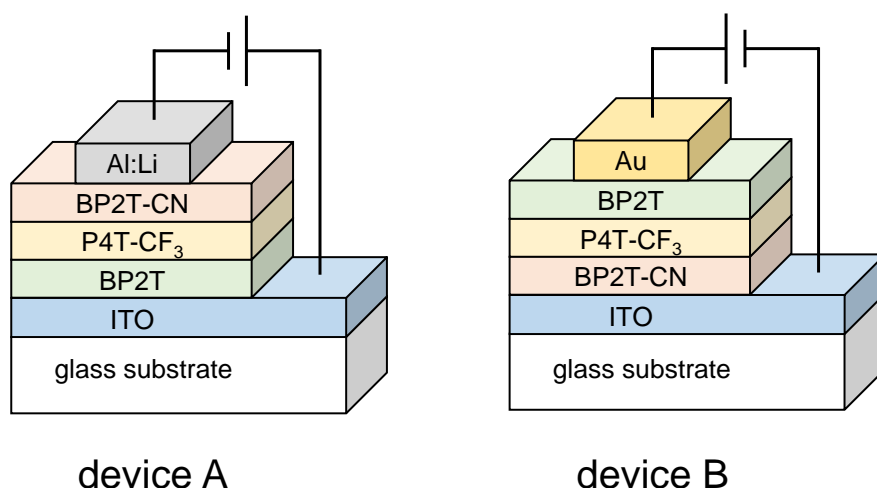
Fig. 3.15. Schematic diagrams for fabricated organic EL devices of Al:Li/BP2T-CN/P4T-CF₃/BP2T/ITO (device A) and Au/BP2T/P4T-CF₃/BP2T-CN/ITO (device B).

out as described in Section 3.1 and 3.2.

Device applications with single crystal for i-layer:

Substrate preparation and vapor-deposition of the p- and n-layers were carried out by as described for the device B as shown in **Fig. 3.16**. The insertion of the P4T-CF$_3$ i-layer was performed by dropping and casting a suspension P4T-CF$_3$ single crystals in methanol onto the BP2T-CN/ITO surface. After evaporation of the solvent, an amorphous fluoropolymer CYTOP (AGC TTX-801A) film was spin-coated on the surface of P4T-CF$_3$ single crystal/BP2T-CN/ITO at 500 rpm for 5 s, 700 rpm for 20 s, and 2000 rpm for 2 s under a nitrogen atmosphere. The sample was annealed at room temperature for 30 min, at 80 °C for 60 min, and 180 °C for 60 min to remove the solvent. This CYTOP film performs a role as an insulator layer to prevent the direct contact between BP2T and BP2T-CN layers. Electrical measurements of this device with crystal P4T-CF$_3$ i-layer was carried out in the same way as described above.
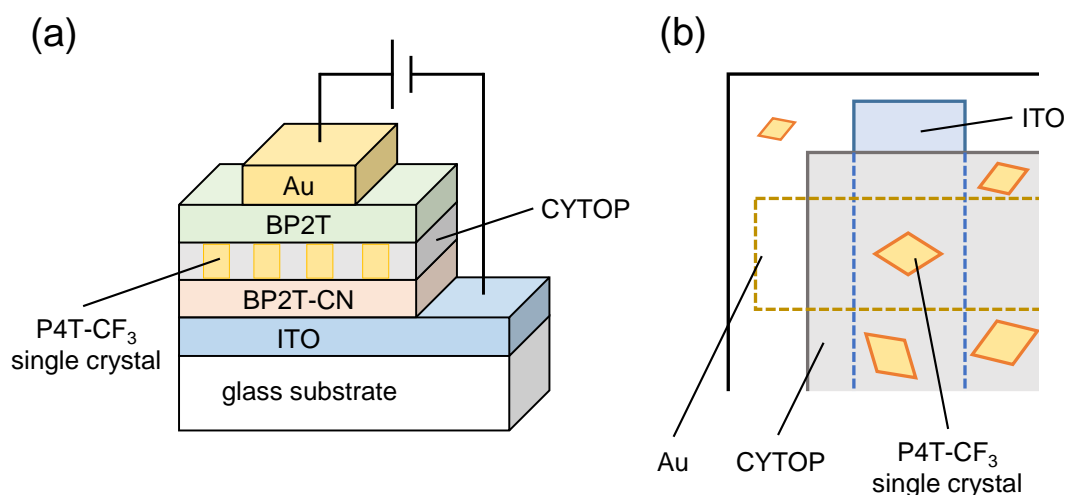
Fig. 3.16. (a) Schematic diagrams for fabricated organic EL devices of Au/BP2T/P4T-CF₃ and CYTOP/BP2T-CN/ITO with P4T-CF₃ single crystals for i-layer. (b) Top-view Schematic diagrams for fabricated devices.

3.3.3   Results and discussion

The HOMO/LUMO energy levels of P4T-CF$_3$ were estimated to be −4.77/−3.17 eV by DFT calculations as shown in **Fig. 3.17(a)**. By introducing trifluoromethyl groups, the HOMO and LUMO energy levels of P4T-CF$_3$ are deepened by 0.37 and 0.41 eV, respectively, with respect to those of unsubstituted 5,5'''-biphenyl-2,2':5',2'':5'',2'''-quaterthiophene (P4T). According to this result, the multilayered EL device structure of BP2T-CN/P4T-CF$_3$/BP2T or BP2T/P4T-CF$_3$/BP2T-CN was adopted for formation of p-i-n heterojunction by using all TPCO derivatives. The P4T-CF$_3$ molecule belongs to the point group of C_{2h} and the HOMO and LUMO have B_g and A_u symmetry, respectively, as same as BP2T and BP2T-CN molecules [**Fig. 3.17(b)**].

A fluorescence micrograph of a solution-grown single crystal of P4T-CF$_3$ is shown in **Fig. 3.18(a)**. The crystal grows in a thin rhombus-shaped platelet with a size of ~150 μm and a thickness of 1−5 μm. The crystal structure determined by the XRD analysis is that P4T-CF$_3$ molecules are packed in a monoclinic from *P2$_1$/c*, *a* = 26.4615, *b* = 7.6530, *c* = 6.1162 Å, *β* = 91.796°. **Figures 3.18(b)** and **(c)** show unit cell projections on the *ab*- and *bc*-planes,
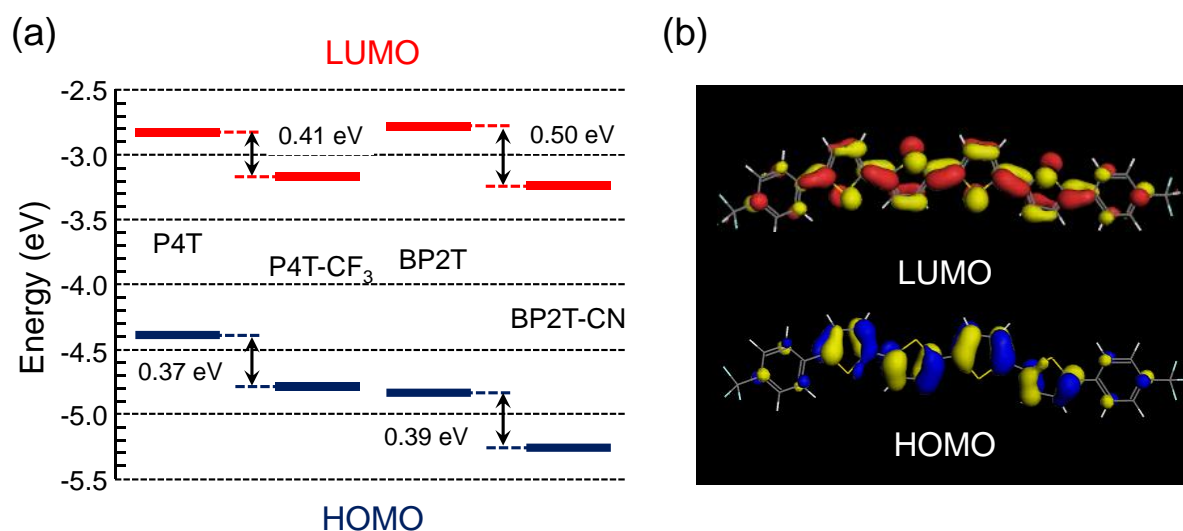
Fig. 3.17. HOMO/LUMO energy levels of P4T, P4T-CF₃, BP2T, and BP2T-CN (a) and frontier molecular orbitals of P4T-CF₃ (b) estimated by DFT calculations.
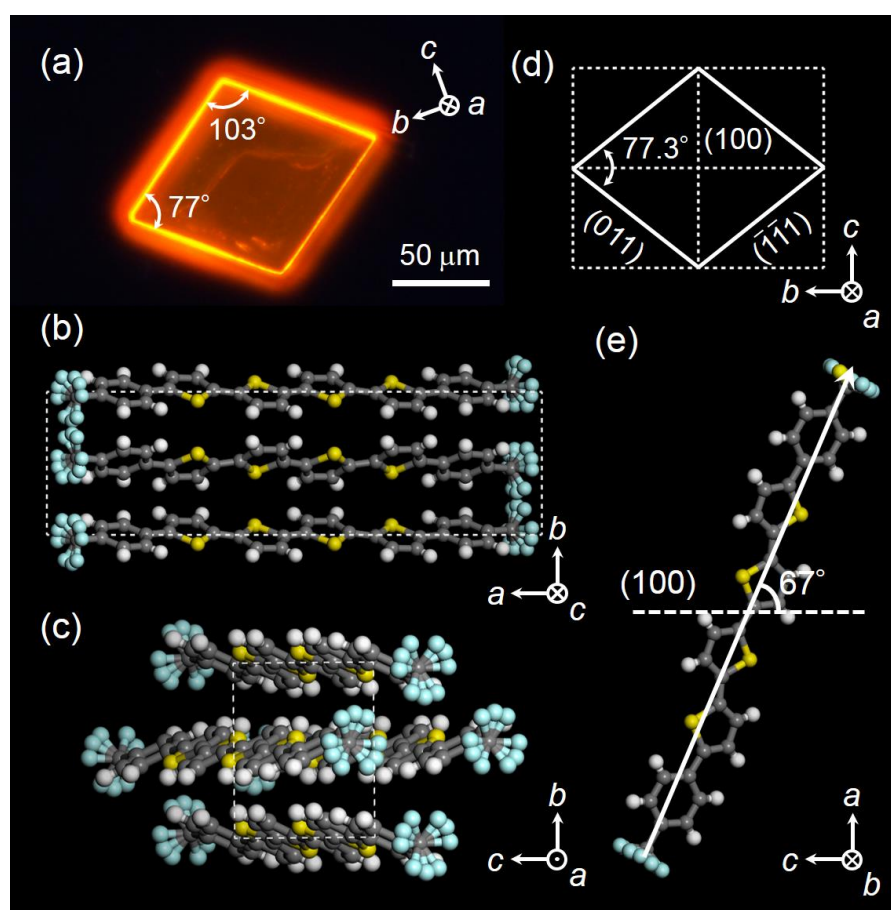

Fig. 3.18. (a) Fluorescence micrograph of P4T-CF₃ single crystal under UV excitation. Crystal structures of P4T-CF₃ projected on the ab- (b) and bc-plane (c). (d) Crystal lattice in the bc-plane. (e) Molecular orientation against the (100) plane.

pulsed excitation. In weak excitation density below 200 μJ/cm^2, broad emission band of the

respectively. **Figure 3.18(d)** displays the crystal lattice in the *bc*-plane indicating that the lattice

angle between the (011) and (−1−11) face is 77.3°. This angle is consistent with the edge angle

of the rhombus shape in **Fig. 3.18(a)**. The basal face of the single crystal is assigned to the

(100) plane against which the molecular axis tilts by 67° as shown in **Fig. 3.18(e)**. Since the π-

electronic transition dipole moment between the HOMO and LUMO is parallel to the molecular

axis, this molecular orientation enhances light propagation in the planar direction and light

leakage from the crystal surface is limited. Therefore, intense emission is observed at the crystal

edges as seen in **Fig. 3.18(a)**.

Toward exploring a possibility of laser diodes with the p-i-n structure, optically pumped

lasing with single-crystal P4T-CF$_3$ was examined. **Figure 3.19(a)** shows PL and optical

absorption spectra of a solution-grown P4T-CF$_3$ single crystal. This crystal has orange emission

with a fluorescence maximum at around 620 nm assigned to the vibronic progression of the

0−2 transition under ultraviolet excitation. The 0−0 transition is basically forbidden due to

antiparallel exciton coupling between the adjacent molecular. **Figures 3.19(b)** and **(c)** display

excitation density dependence of PL spectra and integrated PL intensity, respectively, under fs-

0−2 transition appears at 620 nm. With increasing excitation density to 400 μJ/cm^2, the 0−2

band is first gain-narrowed and its integrated intensity increased nonlinearly. With further

increase at 1300−1500 μJ/cm^2, the 0−1 emission at 575 nm is also amplified since self-

absorption effect is not significant at higher excitation density. High resolution PL spectra

(spectral resolution: 0.04 nm) of the 0−2 emission band are shown in **Fig. 3.19(d)**. In the

amplified emission band, interference fringes are observed with increasing excitation density

above the threshold. Considering the fringe intervals ($\Delta\nu = 8.81-10.7$ cm^{-1}) and the cavity

length of the rhombus crystal, this interference spectra are not ascribed to a simple F-P lasing

but based on multiple reflection of emitted light inside the crystal [**Fig. 3.19(d)** inset]. These
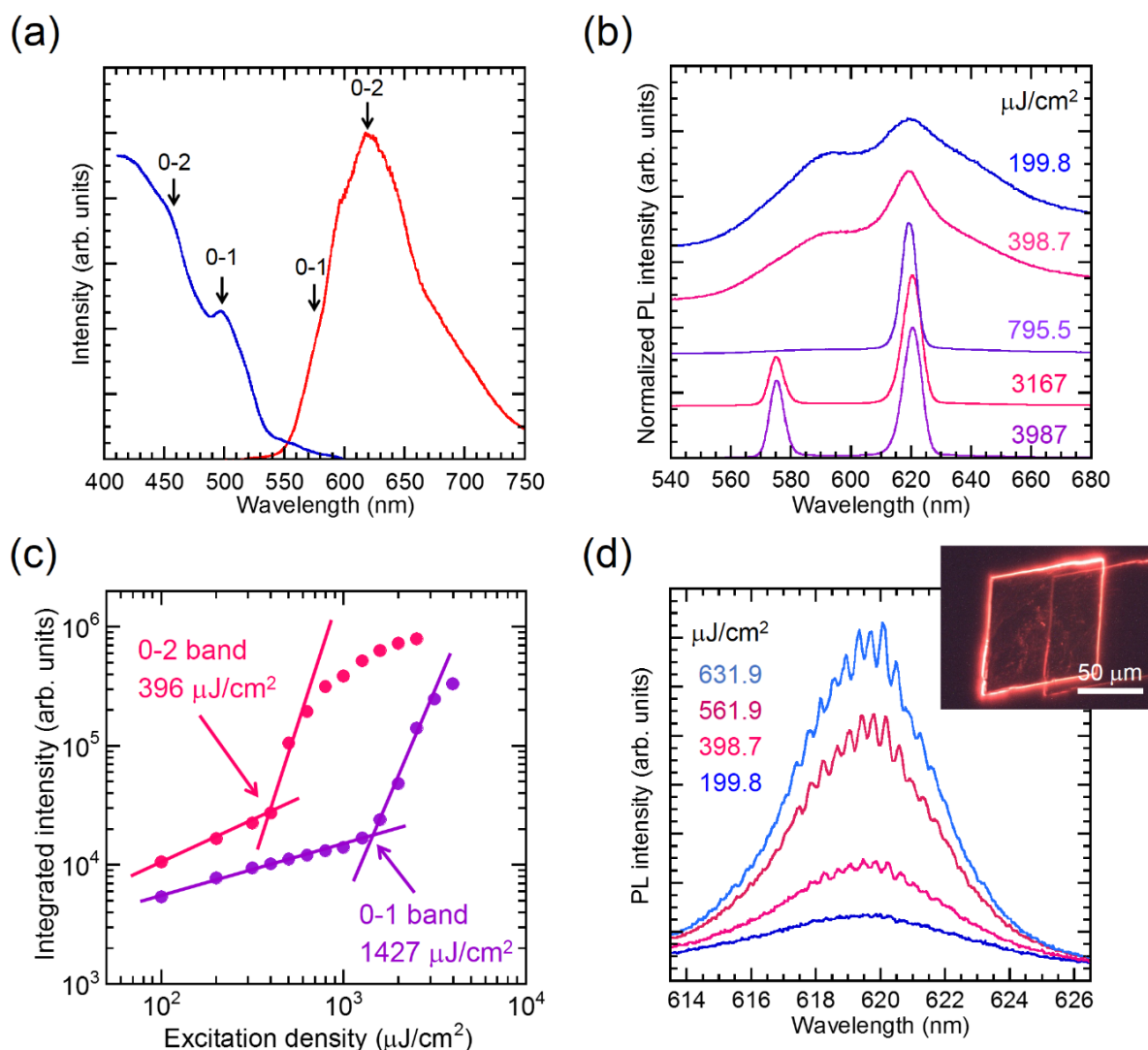
Fig. 3.19. (a) Optical absorption (blue) and PL (red) spectra of single-crystal P4T-CF₃. (b) Normalized PL spectra of single-crystal P4T-CF₃ as a function of excitation density. (c) Excitation density dependence of integrated intensity of the 0−1 and 0−2 bands. (d) Excitation density dependence of high-resolution PL spectra at the 0−2 band. The inset shows photograph of light emission from the P4T-CF₃ single crystal taken above threshold excitation of the amplified 0−2 emission.

results suggest that the P4T-CF₃ crystal has an attractive potential for organic semiconductor laser medium.

The fabricated organic EL devices using vapor-deposited films of both device A and device B indicated rectifying current increase under positive bias application to the bottom ITO and top Au anodes, respectively [**Fig. 3.20(a)**]. The current onset voltage is slightly higher for

the device B [see inset in **Fig. 3.20(a)**] probably due to higher energy barrier for electron injection from the ITO cathode compared to the Al:Li cathode for the device A [**Fig. 3.20(b)**]. However, the current increase is considerably higher for the device B when the bias voltage is increased above 10 V. During these $I-V$ measurements, light emission was observed from the bottom ITO/glass substrate for both devices. **Figure 3.20(c)** displays EL spectra for both devices at a bias voltage of 22 V. For reference, the PL spectrum of a vapor-deposited P4T-CF$_3$ film shows emission peaks at 571.4 and 616.7 nm which are assigned to the 0−1 and 0−2 vibronic progressions of the HOMO/LUMO transitions, respectively. Shoulder peaks appeared at around 536 and 664 nm are assigned to the 0−0 and 0−3 transitions, respectively. Both devices show EL spectra with emission peaks at 572 and 617 nm. Especially, the EL spectrum of the device B is almost consistent with the PL spectral feature of the reference film. Thus, these results indicate that holes and electrons, respectively injected from the BP2T and BP2T-CN layers, are accumulated and recombined in the P4T-CF$_3$ layer which functions as an active layer in the p-i-n devices. Current density-luminance characteristics of both devices are presented in **Fig. 3.20(d)**. It reveals that the EL efficiency of the device B is about 3 times as high as that of device A. However, the luminance is rolled off at lower current density for the device B. Consequently, the maximum luminance reached 421 cd/m^2 at 547 mA/cm^2 for the device A and 177 cd/m^2 at 46.9 mA/cm^2 for the device B.

In order to discuss those difference in devices A and B depending on the deposition order of the p- and n-layers, EL photographs and AFM images were taken for both p-i-n devices. The device A in which the p-type BP2T layer is first deposited shows homogeneous EL, whereas the device B with inverted structure shows dotted EL as compared in **Figs. 3.21(a)** and **(b)**.

AFM images taken for P4T-CF$_3$/BP2T/ITO and P4T-CF$_3$/BP2T-CN/ITO samples are shown in **Figs. 3.21(c)** and **(d)**, respectively. The average surface roughness (R_a) of the latter sample is 15.0 nm considerably larger than 9.8 nm of the former sample. Since the latter sample
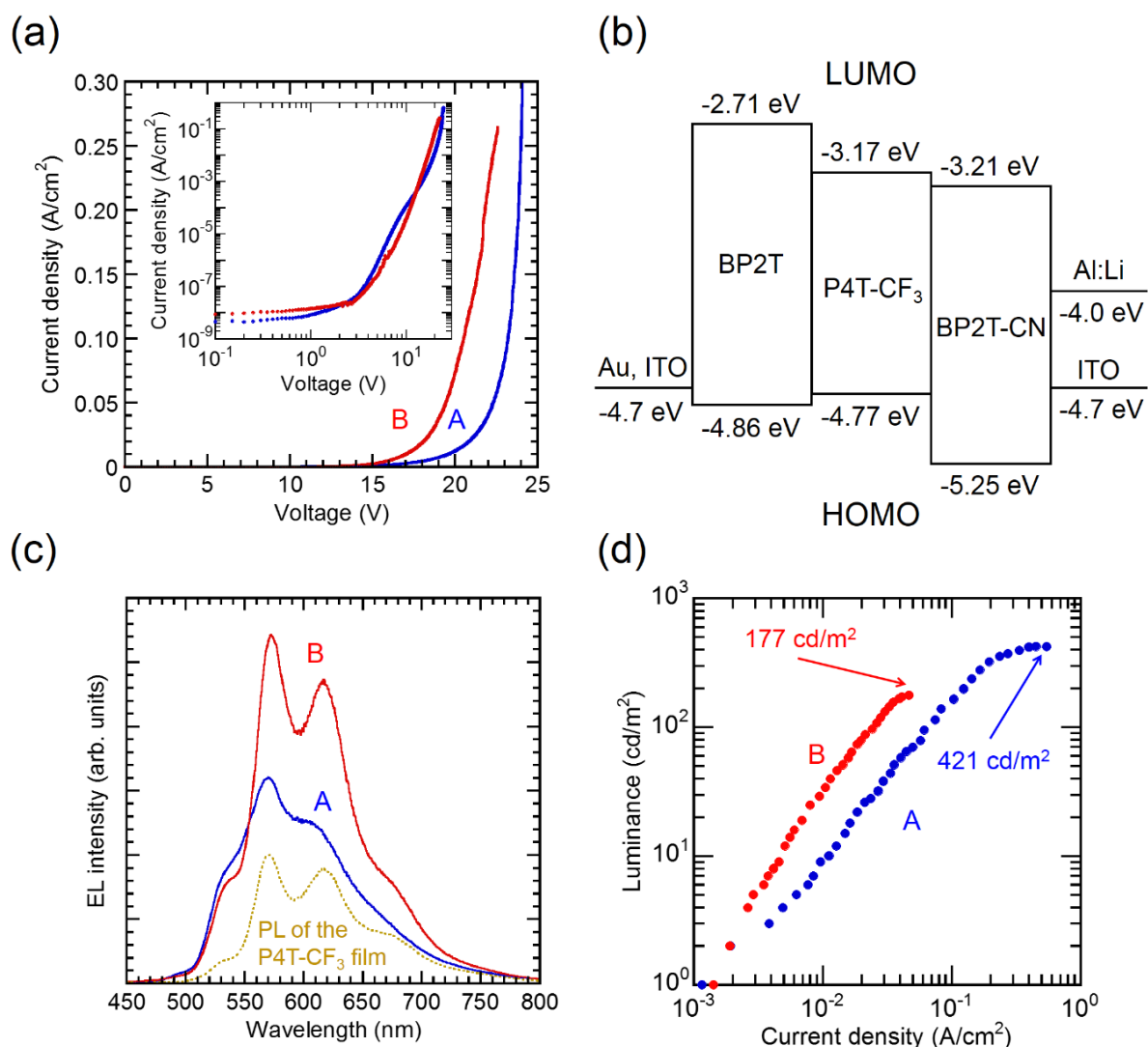
Fig. 3.20 (a) Current−voltage characteristics of the device A (blue solid line) and the device B (red solid line). The inset shows their double logarithmic plots. (b) Energy diagrams of fabricated organic EL devices. (c) EL spectra of the device A (blue solid line) and the device B (red solid line). PL spectrum of P4T-CF$_3$ film (yellow dashed line) is indicated as reference. (d) Luminance-current characteristics of the device A (blue solid line) and the device B (red solid line).

exhibits dotted morphology in its AFM image [**Fig. 3.21(d)**], the dotted EL observed for the device B is ascribed to the inhomogeneous morphology of the P4T-CF$_3$ layer deposited on the BP2T-CN film. On the other hand, the homogeneous P4T-CF$_3$ layer deposited on the BP2T layer results in homogeneous EL.

To compare the film crystallinity and molecular orientation in both p-i-n devices, XRD
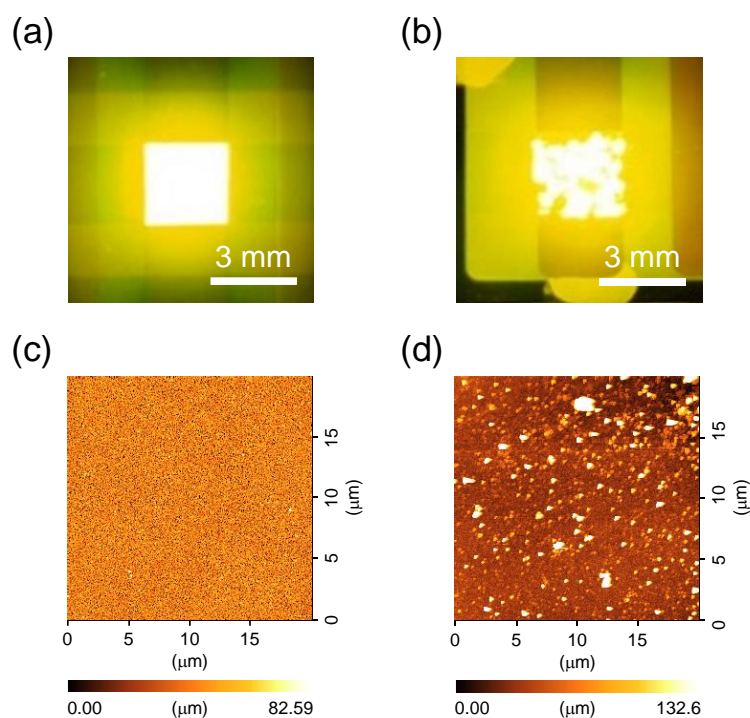
Fig. 3.21. Photographs of EL from the device A (a) and the device B (b). AFM images of P4T-CF₃ (100 nm)/BP2T (100 nm) (c) and P4T-CF₃ (100 nm)/BP2T-CN (100 nm) (d) films vapor-deposited on ITO/glass substrate. The deposition rate of all films is 0.5 Å/s.

measurements were performed in $\theta/2\theta$ scans. The XRD pattern of a single-layered P4T-CF$_3$ film [**Fig. 3.22(a)**] indicates no diffraction peaks other than those assigned to ITO, indicating that it forms an amorphous film on ITO/glass substrate. It has been reported for the unsubstituted P4T film that diffraction peaks are observed up to sixth order corresponding to standing molecular alignment on the substrate[27,28]. Therefore, the introduction of bulky trifluoromethyl groups hinders the crystallization by intermolecular π–π stacking and it may affect the film morphology of P4T-CF$_3$ depending on the underlying layers. When P4T-CF$_3$ is deposited on the BP2T layer (the case of the device A), the XRD pattern is identical to the single-layered BP2T film which shows the (002) reflection at 3.24° (spacing of d = 2.72 nm) corresponding to standing orientation of BP2T molecules [**Fig. 3.22(b)**]. On the other hand, when P4T-CF$_3$ was deposited on the BP2T-CN layer (the case of the device B), diffraction peaks are observed at 22.5° (d = 0.39 nm) assigned to the (020) plane of P4T-CF$_3$ crystal and
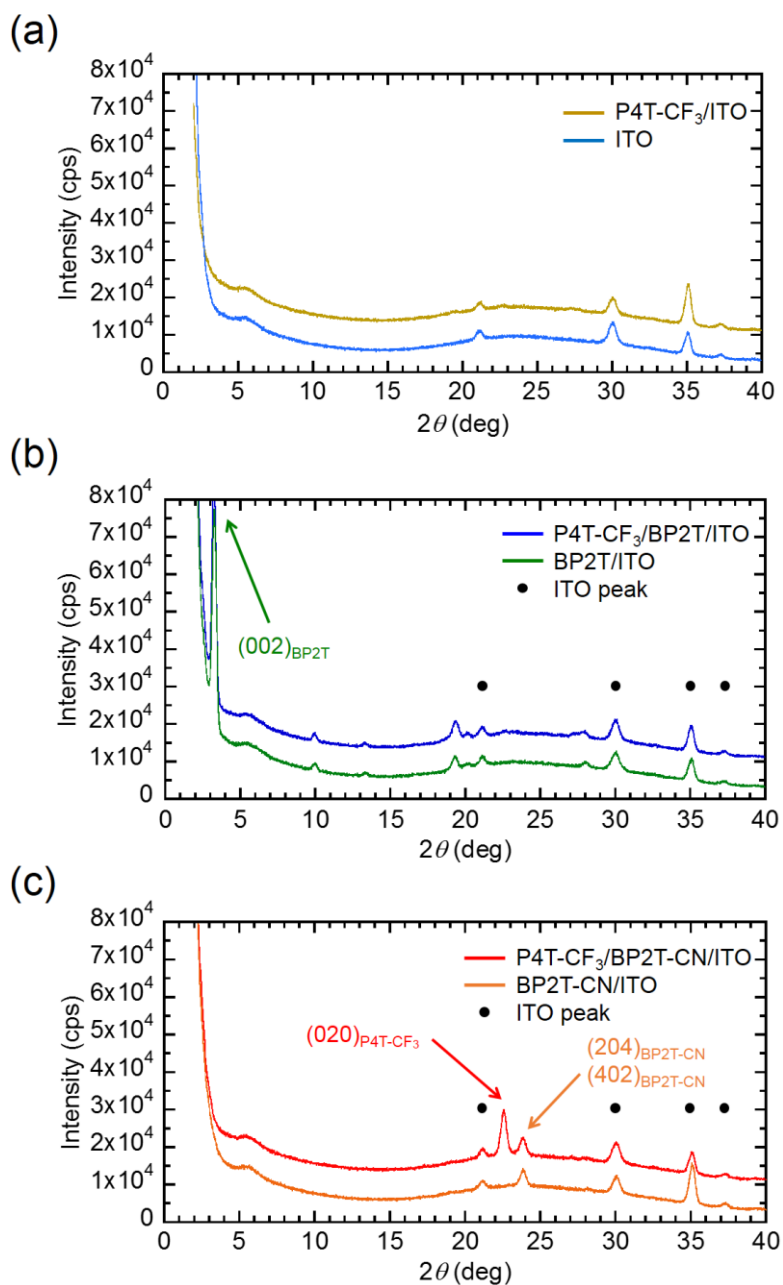
Fig. 3.22. *XRD patterns of P4T-CF₃ (100 nm) (a), P4T-CF₃ (100 nm)/BP2T (100 nm) (b) and P4T-CF₃ (100 nm)/BP2T-CN (100 nm)/ITO (c) films vapor-deposited on ITO substrate. XRD patterns of ITO, BP2T (100 nm)/ITO and BP2T-CN (100 nm)/ITO are indicated as reference in (a), (b) and (c), respectively.*

at 23.8° ($d = 0.37$ nm) corresponding to the (204) or (402) reflection from the BP2T-CN layer

[**Fig. 3.22(c)**]. Those reflection planes reveal that the both P4T-CF₃ and BP2T-CN molecular

axes orient preferably lying on the substrate. These XRD results suggest that the dotted

morphology in the device B is caused by crystallization of lying P4T-CF$_3$ molecules on the BP2T-CN layer in which intermolecular π–π stacking and electrostatic interaction between electron-withdrawing cyano and trifluoromethyl groups may play a significant role. On the other hand, the standing BP2T layer has less effect on the crystallization of P4T-CF$_3$ molecules in the device A.

As mentioned above, the EL efficiency was higher for the device B having dotted P4T-CF$_3$ layer than for the device A having homogeneous P4T-CF$_3$ layer [**Fig. 3.20(d)**]. It is probably due to effective carrier confinement into the P4T-CF$_3$ grains in the i-layer. However, the maximum current density and luminance are decreased in the device B which can be ascribed to inhomogeneous p-i-n double-hetero structure. In order to improve the uniformity of dotted emission in the device B, the dependence of the P4T-CF$_3$ layer morphology on deposition rate was examined. **Figures 3.23(a)** and **(b)** show EL photographs of the device B fabricated with the P4T-CF$_3$ layer vapor-deposited at rate of 1.1 and 0.11 Å/s, respectively. Corresponding AFM images of the P4T-CF$_3$/BP2T-CN/ITO surface are shown in **Figs. 3.23(c)** and **(d)**, respectively. The faster deposition rate of 1.1 Å/s results in more discrete dotted EL and larger surface roughness (R_a = 23.2 nm) compared to the aforementioned results at 0.5 Å/s [**Figs. 3.23(b)** and **(d)**]. When the deposition rate is decreased to 0.11 Å/s, the surface roughness is reduced to R_a = 10.0 nm and homogeneous EL with increased dot density was obtained. The slower deposition may help the P4T-CF$_3$ molecules migrate on the BP2T-CN layer and the π–π chain interaction between them could promote the homogeneous nucleation of P4T-CF$_3$ crystallites.

Finally, an organic EL device (Au/BP2T/P4T-CF$_3$/BP2T-CN/ITO) with single-crystal P4T-CF$_3$ was fabricated. In order to form p-i-n heterojunction structure, a CYTOP insulator layer was inserted between the vapor-deposited films of BP2T-CN and BP2T. Although this p-i-n structure deteriorates the current value compared to the devices using all vapor-deposited

(a)   (b)
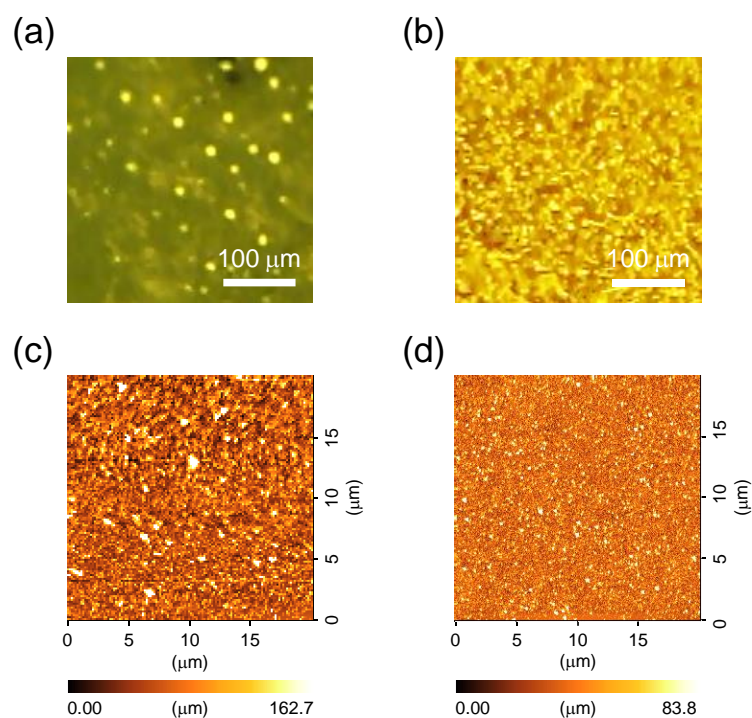
(c)   (d)

Fig. 3.23. Photographs of EL taken for the device B with P4T-CF₃ layers deposited at rate of 1.1 (a) and 0.11 Å/s (b). AFM images of P4T-CF₃ (100 nm, 1.1 Å/s)/BP2T (100 nm, 0.5 Å/s) (c) and P4T-CF₃ (100 nm, 0.11 Å/s)/BP2T-CN (100 nm, 0.5 Å/s) (d) films vapor-deposited on ITO substrate.

films, rectification *I−V* curve and EL characteristic were obtained as shown **Fig. 3.24(a)**.

However, the emission is observed only at the contour edges of the rhombus P4T-CF₃ crystal and the EL spectrum resembles to the PL spectrum of BP2T-CN layer showing 0−1 and 0−2 bands at 559 and 595 nm, respectively [**Fig. 3.24(b)**]. It suggests that carriers are not injected into the single-crystal P4T-CF₃ but the recombination occurs at the BP2T/BP2T-CN interface caused by imperfect insulation with CYTOP along the crystals edges of P4T-CF₃. In order to improve the carrier injection into the P4T-CF₃ crystal, a better construction of p-i-n structure using thinner crystals should be tried, e.g. by introducing template stripping technique.[29−32]
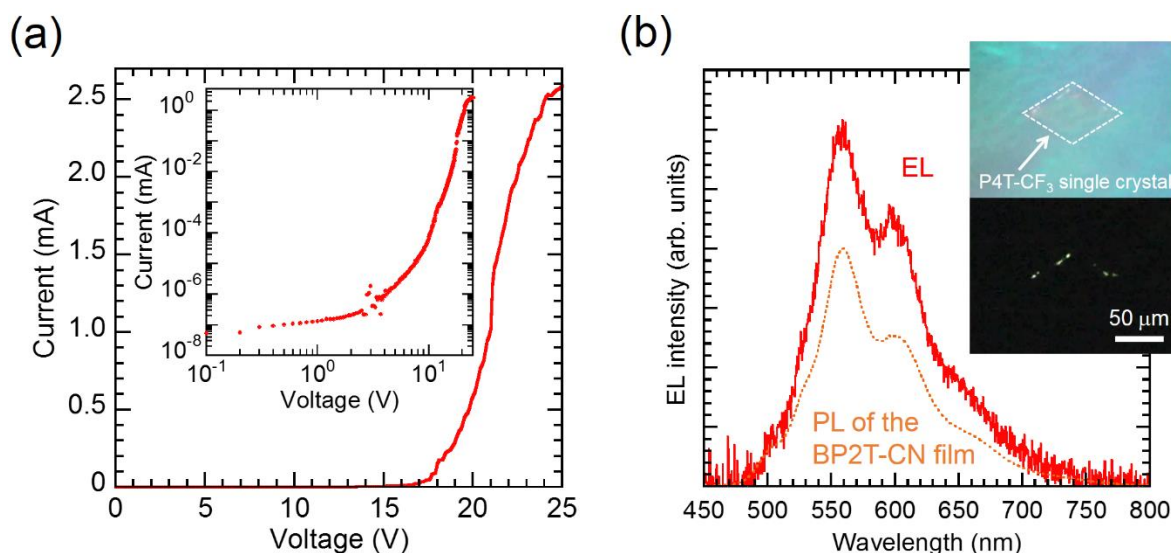
Fig. 3.24. Current-voltage characteristics of the device B with single-crystal P4T-CF3. The inset shows its double logarithmic plot. (b) EL spectra of the device B with single-crystal P4T-CF3. The insets show photographs of the device B with P4T-CF3 single crystal before (top) and under bias application.

3.3.4   Conclusions

Organic EL devices with trilayered p-i-n structures using vapor-deposited film of all TPCO derivatives, BP2T, P4T-CF3, and BP2T-CN, were fabricated. Both devices with opposite deposition order of the p (BP2T) and n (BP2T-CN) layers exhibited electroluminescence from to the i-(P4T-CF3) layer. In particular, the Au/BP2T/P4T-CF3/BP2T-CN/ITO device showed dotted EL with higher emission efficiency at lower bias voltages. The lying orientation of both BP2T-CN and P4T-CF3 in this device is preferable for the carrier injection and transport, and the dotted morphology of crystalline P4T-CF3 may enhance the carrier confinement and recombination in the i-layer. On the other hand, the Al:Li/BP2T-CN/P4T-CF3/BP2T/ITO device with the homogeneous i-layer of amorphous P4T-CF3 showed uniform EL which was sustained at higher current density. Moreover, optically pumped lasing was observed for solution-grown single crystal of P4T-CF3 as and an EL device with this single-crystal i-layer was preliminary fabricated.

References

[1]   N. Ishiyama, M. Kubo, T. Kaji, M. Hiramoto, *Appl. Phys. Lett.* **2012,** 101, 233303.

[2]   H. Hiramoto, M. Kikuchi, S. Izawa, *Adv. Mater.* **2019,** 31, 1801236.

[3]   M. Kubo, K. Iketani, T. Kaji, M. Hiramoto, *Appl. Phys. Lett.* **2011,** 98, 073311.

[4]   N. Ishiyama, T. Yoshioka, T. Kaji, H. Hiramoto, *Appl. Phys. Express* **2013,** 6, 012301.

[5]   F. Sasaki, Y. Kawaguchi, H. Mochizuki, S. Haraichi, T. Ishitsuka, T. Ootsuka, T. Tomie, S. Watanabe, Y. Shimoi, T. Yamao, S. Hotta, *Mol. Cryst. Liq. Cryst.* **2014,** 17, 20.

[6]   K. Bando, T. Nakamura, Y. Masumoto, F. Sasaki, S. Kobayashi, S. Hotta, *J. Appl. Phys.* **2006,** 99, 013518.

[7]   K. Bando, T. Nakamura, S. Fujiwara, Y. Masumoto, F. Sasaki, S. Kobayashi, Y. Shimoi, S. Hotta, *Phys. Rev. B* **2008,** 77, 045205.

[8]   S. Hotta, M. Goto, R. Azumi, M. Inoue, M. Ichikawa, Y. Taniguchi, *Chem. Mater.* **2004,** 16, 237.

[9]   N. Matsumoto, M. Nishiyama, C. Adachi, *J. Phys. Chem.* **2008,** 112, 7735.

[10] M. Era, T. Tsutsui, S. Saito, *Appl. Phys. Lett.* **1995,** 67, 2436.

[11] Y. Toda, H. Yanagi, *Appl. Phys. Lett.* **1996,** 69, 2315.

[12] H. Yanagi, S. Okamoto, *Appl. Phys. Lett.* **1997,** 71, 2563.

[13] D. Yokoyama, *J. Mater. Chem.* **2011,** 21, 19187.

[14] T. Matsushima, H. Murata, *J. Appl. Phys.* **2012,** 112, 024503.

[15] H. Yamane, S. Nagamatsu, H. Fukagawa, S. Kera, R. Friedlein, K. K. Okudaira, N. Ueno, *Phy. Rev. B* **2005,** 72, 153412.

[16] H. Fukagawa, H. Yamane, T. Kataoka, S. Kera, M. Nakamura, K. Kudo, N. Ueno, *Phy. Rev. B* **2006,** 73, 245310.

[17] S. Kera, N. Ueno, *J. Electron Spectrosc. Relat. Phnom.* **2015,** 204, 2.

[18] K. Sugiyama, H. Ishii, Y. Ouchi, K. Seki, *J. Appl. Phys.* **2000,** 87, 295.

[19] R. Hatano, K. Goto, K. Yamashita, F. Sasaki, H. Yanagi, *Jpn. J. Appl. Phys.* **2017**, 56, 04CL02.

[20] C. Adachi, S. Tokito, T. Tsutsui, S. Saito, *Jpn. J. Appl. Phys.* **1988,** 27, L 269.

[21] C. Adachi, S. Tokito, T. Tsutsui, S. Saito, *Jpn. J. Appl. Phys.* **1988,** 27, L 713.

[22] M. Ikai, S. Tokito, Y. Sakamoto, T. Suzuki, Y. Taga, *Appl. Phys. Lett.* **2001,** 79, 156.

[23] H. Yan, B. J. Scott, Q. Huang, T. J. Marks, *Adv. Mater.* **2004,** 16, 1948.

[24] Y. Kijima, N. Asai, S. Tamura, *Jpn. J. Appl. Phys.* **1999,** 38, 5274.

[25] S. Ando, R. Murakami, J. Nishida, H. Tada, Y. Inoue, S. Tokito, Y. Yamashita, *J. Am. Chem. Soc.* **2005,** 127, 14996.

[26] T. Katagiri, S. Ota, T. Ohira, T. Yamao, S. Hotta, *J. Heterocycl. Chem.* **2007,** 44, 853.

[27] S. A. Lee, Y. Yoshida, M. Fukuyama, S. Hotta, *Synth. Met.* **1999,** 106, 39.

[28] S. Hotta, Y. Ichino, Y. Yoshida, M. Yoshida, *J. Phys. Chem. B.* **2000,** 104, 10316.

[29] R. Ding, J. Feng, X. -L. Zhang, W. Zhou, H. -H. Fang, Y. F. Liu, Q. D. Chen, H. Y. Wang, H. -B. Sun, *Adv. Funct. Mater.* **2014,** 24, 7085.

[30] R. Ding, J. Feng, W. Zhou, X. -L. Zhang, H. -H. Fang, T. Yang, H. -Y. Wang, S. Hotta, H. -B. Sun, *Sci. Rep.* **2015,** 5, 12445.

[31] R. Ding, J. Feng, F. X. Dong, W. Zhou, Y. Liu, X. -L. Zhang, X. P. Wang, H. -H. Fang, B. Xu, X. B. Li, H. Y. Wang, S. Hotta, H. -B. Sun, *Adv. Funct. Mater.* **2017,** 27, 1604659.

[32] R. Ding, X. -P. Wang, J. Feng, X. -B. Li, F -X. Dong, W. -Q. Tian, J. -R. Du, H. -H. Fang, H. -Y. Wang, T. Yamao, S. Hotta, H. -B. Sun, *Adv. Mater.* **2018,** 30, 1801078.

Chapter 4

Fabrication and Characterization of Organic Electroluminescence Devices with Microcavity Structure

Exciton-polariton is a hybrid light-matter quasi-particle defined as a mixture of excitons and photons created by strong coupling with each other. One of its intriguing applications is a polariton laser, which is a coherent radiation from polariton condensation at a low excitation energy. In this Chapter, organic EL devices with surface-emitting microcavity structure are fabricated using vapor-deposited films of a cyano-substituted TPCO, aiming at polariton formation under electrical excitation. Confinement of excitons and photons in the device result in the formation of cavity polaritons with a large Rabi-splitting energy ($2\hbar\Omega = 250$ meV). Furthermore, efficient relaxation into the bottom of lower polariton branch (LPB) is confirmed from angle-resolved EL spectra. In excitation-density dependences, the luminance of microcavity EL devices shows a superlinear increase with an elevation of current density which might be attributed to incorporation of triplet excitons into the polariton formation.

86

4.1 Introduction

As mentioned in the previous Chapters, the realization of electrically pumped organic lasers requires high-density carrier injection (over 10 kA/cm^2), reduced waveguiding loss due to light absorption by electrodes, and prevention of non-radiative triplet excitons and polarons. To overcome these issues, this Chapter focuses on organic polariton lasing as an alternative to ordinary photon lasing. Polariton lasing is coherent radiation from exciton-polaritons created by strong coupling between emissive excitons and photons typically confined in a microcavity.[1–6] A low threshold polariton lasing is possible due to the strong coupling regime in semiconductor microcavities without formation of the conventional population inversion scheme.[7] Owing to the large oscillator strength and high exciton binding energy in Frenkel excitons, molecule-based excitons enable polariton formation at room temperature. Recently, polariton condensation and coherent light emission at room temperature have been reported for microcavities filled with molecular crystals,[8] π-conjugated oligomer and polymer thin films,[9,10] molecular dyes dispersed in a matrix polymer,[11] and a hybrid structure of organic J-aggregate dye as well as inorganic GaAs quantum well[12] under optically pumped excitation. Moreover, some extensive studies have achieved strong and ultrastrong exciton-photon coupling in microcavity EL devices[13–17] and LEFET devices.[18,19] Those previous studies suggest the importance of exploring advanced functional materials and development of optimal device structures for the realization of organic polariton lasing especially under electrical excitation.

Previous studies have reported the formation of exciton-polaritons in cyano-substituted TPCO crystals under optical excitation using VCSEL structure with distributed Bragg reflector (DBR) resonators.[20–24] In contrast to unsubstituted TPCO crystals in which the oligomer molecules are mostly oriented perpendicular to the crystal plane, those cyano-substituted

TPCO molecules lay in their platelet-shaped crystals as mentioned in the previous Chapters. This lying orientation is suitable for the VCSEL structure since the transition dipole moments being parallel to the linear molecular axis enhance the strong coupling between the cavity photons and the confined excitons. These studies using single-crystal TPCO microcavities have reported a high exciton-photon coupling strength (namely Rabi splitting energy) of ~100 meV, demonstrating a stable formation of exciton-polaritons at room temperature. Since TPCO crystals typically grown with a thickness of 1−2 μm give rise to multiple cavity photon modes, it could be further improved by thinning the crystal thickness to confine a single cavity photon mode. However, their precise thickness control is difficult, and such thin crystals are not easily handled to construct electrically driven VCSELs. Since the TPCO crystals are so far unable to directly grow in the multilayered EL structure, vapor- or solution-grown crystals should be transferred onto the device which results in contamination and electrical contact failure.

In this Chapter, therefore, organic microcavity EL devices were fabricated by using conventional vapor deposition of p-n junction films with TPCO derivatives aiming at electrically excited exciton-polariton formation at room temperature. While these films are inferior to single crystal media with perfect molecular orientation, the cyano-substituted TPCO molecules tend to orient lying on the substrate in vapor-deposited thin films as mentioned in Chapter 3. By precisely controlling the multilayered cavity thickness in the device, a strong coupling regime with a large Rabi-splitting energy (~250 meV) is obtained under both optical and electrical excitations. It is also noted that efficient relaxation into the bottom of lower polariton branch (LPB) is confirmed from angle-resolved reflectance, PL and EL spectroscopies. Moreover, nonlinear increase of EL intensity with an elevation of injected current density, deduces incorporation of triplet excitons into polariton formation.

4.2   Experimental Section

Device Fabrication:

Heterojunction type organic microcavity EL devices were fabricated by vapor-depositing BP2T-CN (emission and electron transport layer), BP2T (hole transport layer), MoO$_3$ (hole injection layer) and Au (anode) onto an ITO (63 nm) coated DBR mirror as shown schematically in **Fig. 4.1**. The bottom DBR mirror used for the microcavity fabrication consists of 53 alternating pairs of SiO$_2$/Ta$_2$O$_5$ quarter-wavelength-thick layers on a glass substrate (10 × 10 mm^2). 63 nm-thick ITO was sputtered onto the DBR surface. The ITO was etched to form a stripe pattern (3 × 10 mm^2) by a laser processing system (V-Technology VL-C30) with a pulse duration of 5 ns and a repetition rate of 30 Hz at λ_{ex} = 532 nm. The ITO/DBR substrate was cleaned with a neutral detergent, pure water and isopropyl alcohol in an ultrasonic cleaning bath, then the substrate surface was treated with UV-ozone exposure.

BP2T-CN (125 nm), BP2T (90 nm), and MoO$_3$ (10 nm) were vapor-deposited on the ITO/DBR substrate with a rate of 5 Å/s by monitoring with a quartz oscillator under a vacuum of ~2.0 × 10^{-4} Pa. In this Chapter, MoO$_3$ layer was added to improve hole injection and prevent Au incursion into organic layers. This MoO$_3$ layer was successively vapor-deposited onto the BP2T/BP2T-CN/ITO/DBR surface without breaking the vacuum. Finally, a 35 nm-thick Au electrode was deposited through a shadow mask (1.5 × 10 mm^2) to orthogonally across the ITO cathode with a rate of 15 Å/s under a vacuum of ~2.0 × 10^{-4} Pa. The deposited thicknesses were confirmed by a surface profiler (Kosaka Laboratory ET200). A fluorescence spectrum of the BP2T-CN film was observed under ultraviolet excitation (λ_{ex} = 365 nm) using a high-pressure mercury light source (Olympus BH2-RFL-T3) equipped with a fluorescence microscope (Olympus BX51) and a CCD multichannel spectrometer (Hamamatsu Photonics PMA-12). Transmission and absorption spectra of the bottom DBR mirror and the BP2T-CN
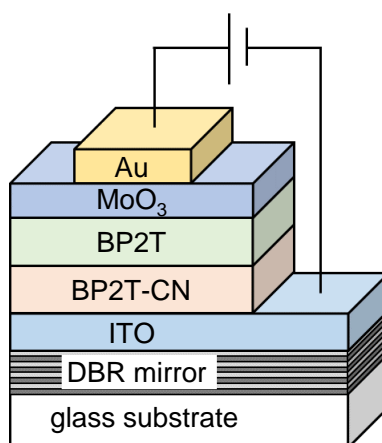
Fig. 4.1. Schematic diagram of the fabricated microcavity EL device.

films were measured with a UV-Vis spectrophotometer (JASCO V-530).

Device Characterization:

Angle-resolved PL measurements were carried out using an excitation source of a *Q* switched solid state laser (CryLaS FTSS 355-Q4) with a pulse duration of 1.4 ns and a repetition rate of 1 kHz at λ_{ex} = 355 nm as depicted in **Fig. 4.2**. The excitation beam with a spot diameter of ~100 μm was incident normal to the bottom DBR mirror and the far-field s-polarized emission from the Au top surface was coupled into an optical fiber collecting to a CCD spectrometer (Roper Scientific SP2156) and detected by a CCD camera (Roper Scientific pro EM512) using an collection lens mounted on a rotation stage. The excitation power density was ~5 mW/cm^2. For angle-resolved reflection measurement, the s-polarized white light of a deuterium tungsten lamp (Ocean Optics DH-2000) was focused onto the top Au surface with a spot diameter of ~100 μm. The far-field reflection beam was analyzed with the same CCD spectrometer and CCD camera used for the PL measurements (**Fig. 4.2**). Optical excitation density dependence measurements were performed for the microcavity EL devices with an excitation duration of 200 fs and a repetition rate of 1 kHz with a Ti:S pulsed laser. The
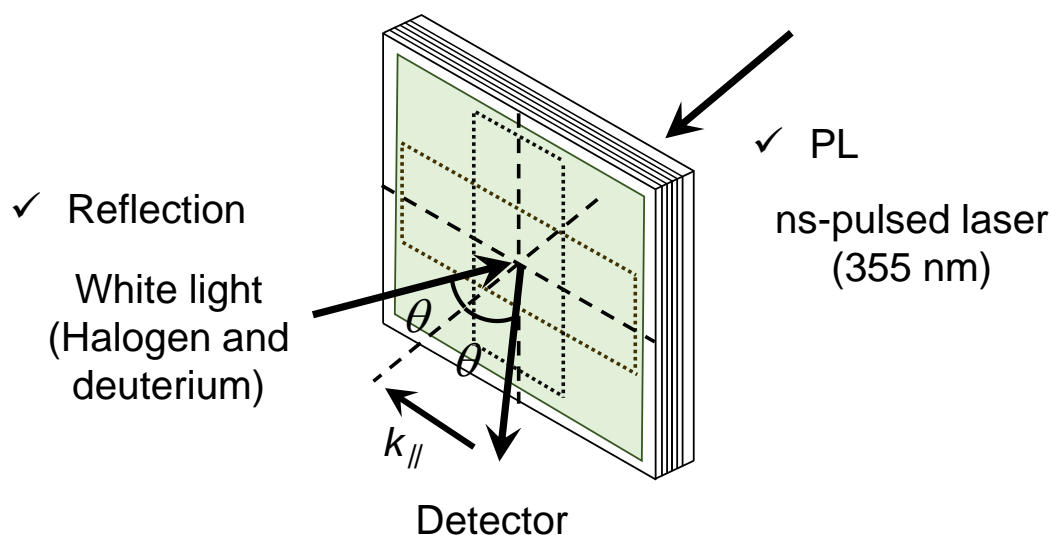
Fig. 4.2. Schematic representation of optical setup for angle-resolved PL and reflection spectroscopy measurements.

microcavity was excited from the bottom DBR mirror and the emitted light from the normal of the DBR mirror was collected with a CCD spectrometer (Roper Scientific ST-133 series). These experiments were carried out in atmosphere at room temperature. In electrical measurements, the fabricated devices were set up in an evacuated glass chamber ($\sim 1.0 \times 10^3$ Pa), and current-voltage (*I–V*) curves were recorded using a source meter system (Keithley 2400). EL spectra and luminance were taken using a CCD multichannel spectrometer (Hamamatsu Photonics PMA-12) and a luminance meter (TOPCON BM-8), respectively. Angle-resolved EL measurements were performed using a light distribution measurement system (Hamamatsu Photonics C9920-11) at a constant voltage of 12 V (~ 80 mA/cm^2).

4.3   Results and Discussion

According to the previous Chapters, the inverted EL device is here adopted as an ideal structure consisting of an air-stable Au anode mirror to construct the microcavity EL devices as shown in **Fig. 4.3(a)**. **Figure 4.3(b)** displays the PL and optical absorption spectra of the
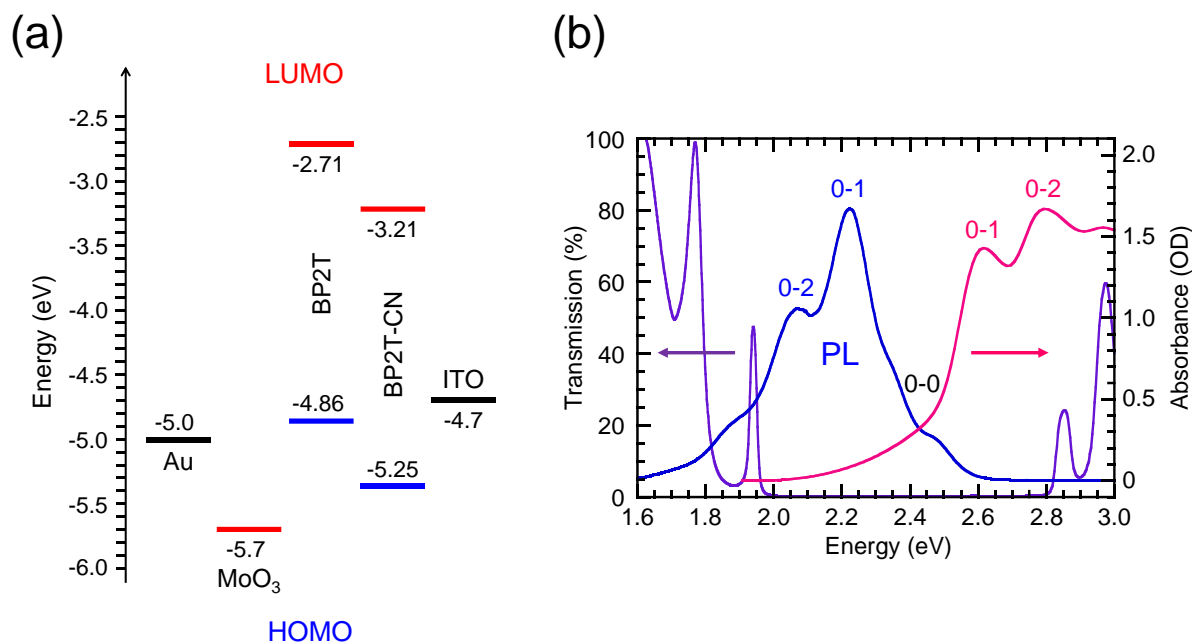
Fig. 4.3. (a) Energy diagram for multilayered components in the device. The HOMO/LUMO energies of BP2T and BP2T-CN were determined by DFT calculation. (b) PL and absorption spectra of BP2T-CN film vapor-deposited on glass substrate and transmission spectrum of bottom DBR mirror used in the device.

vapor-deposited BP2T-CN film with 125 nm thickness on a glass substrate. Vibrational progressions of the 0–1 and 0–2 absorption bands appear at around 2.61 and 2.78 eV, and the 0–1, 0–2 PL bands appear at around 2.22 and 2.09 eV, respectively. The lowest 0–0 transition is estimated at 2.42 eV under the harmonic oscillation approximation. Thus, the 0–0 and 0–1 exciton energies were determined to be E_{ex0-0} = 2.42 eV, and E_{ex0-1} = 2.61 eV, respectively. The purple line in **Fig. 4.3(b)** shows the transmission spectrum of the bottom DBR mirror taken at normal incidence. This DBR mirror consists of SiO_2/Ta_2O_5 quarter wavelength multilayers with high reflectivity of ~99% at the energy range of from 2.0 to 2.7 eV which covers the emission band of the BP2T-CN layer. The DBR was coated with 64 nm-thick ITO to give a quarter wavelength layer at its central reflection energy (E_0 = 2.3 eV). In order to maximize electroluminescence and strong exciton-photon coupling, the emission layer was optimally set

at the antinode position of the optical standing wave when 125 nm-thick BP2T-CN was deposited in the microcavity device. For the observation of exciton-polariton formation in the fabricated microcavity EL device, angle-resolved reflectance spectroscopy was first performed with s-polarized white light. **Figure 4.4(a)** shows reflection spectra as a function of reflectance angle $\theta = 26-60°$ taken from the top Au surface of the microcavity EL device with 125 nm-thick BP2T-CN. As marked in the spectra, three series of reflection dispersions are observed and their negative peak positions shift to the higher energy with increasing reflection angles. The lowest energy dispersion (closed triangles) appears below E_{ex0-0} while the middle energy dispersion emerges between E_{ex0-0} and E_{ex0-1}. Although the highest energy peaks are weak, their magnified spectra show the dispersion above E_{ex0-1}. The anticrossing behaviors of those dispersions are a strong indication of exciton-photon coupling in the fabricated EL device. For clarifying their dispersion relations, the observed angle-resolved reflection spectra were analyzed using a phenomenological 3×3 Hamiltonian, which describes interactions between one cavity photon mode and two exciton mode:

$$H = \begin{pmatrix} E_{ph}(\theta) & \hbar\Omega_0 & \hbar\Omega_1 \\ \hbar\Omega_0 & E_{ex0-0} & 0 \\ \hbar\Omega_1 & 0 & E_{ex0-1} \end{pmatrix}, \tag{4.1}$$

where $\hbar\Omega_0$ and $\hbar\Omega_1$ are the exciton-photon interaction terms with respect to the E_{ex0-0} and E_{ex0-1} excitons, respectively. The cavity photon $E_{ph}(\theta)$ is given by:

$$E_{ph}(\theta) = E_{ph}(0)\left(1 - \frac{\sin^2\theta}{n_{eff}^2}\right)^{-1/2}. \tag{4.2}$$

The analyzed results and the eigenvalues of **formula (4.1)** are shown in **Fig. 4.4(b)**. The three observed reflection dispersions are characterized as the lower, middle and upper polariton blanches (LPB, MPB, and UPB). The fitting parameters are $E_{ph}(0) = 2.35$ eV, $n_{eff} = 1.68$, $2\hbar\Omega_0 = 250$ meV, and $2\hbar\Omega_1 = 244$ meV. **Figure 4.4(c)** displays polariton mixing coefficients for the
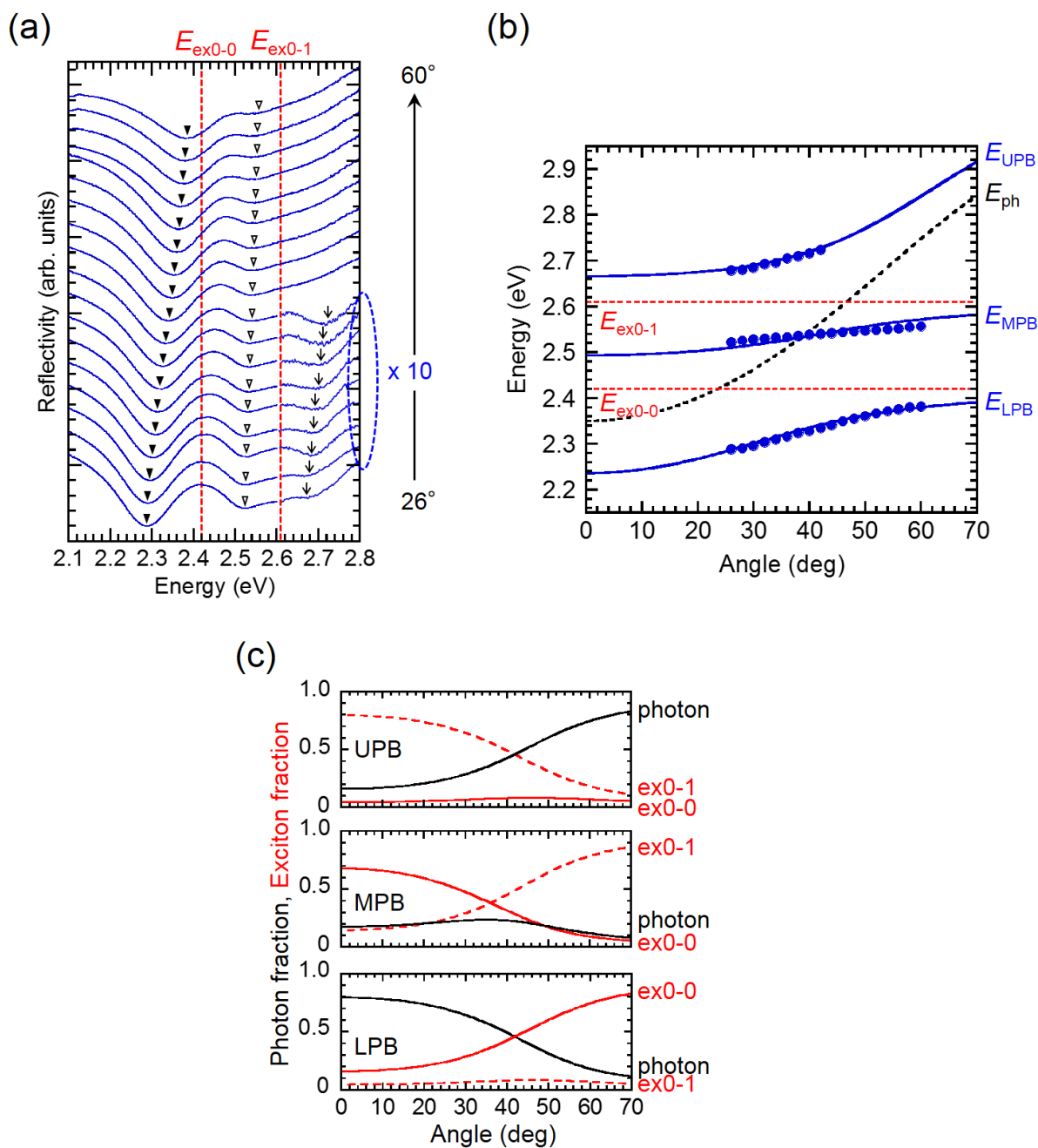
Fig. 4.4. (a) Angle-resolves reflectance spectra taken from the microcavity EL device with 125 nm-thick BP2T-CN layer showing LPB (closed triangle), MPB (open triangle) and UPB (arrow). (b) Dispersion relations of LPB, MPB and UPB plotted from angle-resolved reflectance spectra in (a). The solid blue lines show a fitting result obtained from a calculation with phenomenological Hamiltonian. Dashed black and red lines indicate uncoupled cavity photon and exciton modes, respectively. (c) Angle-dependence of polariton mixing fractions for LPB, MPB, and UPB. Black solid, red solid and red dashed lines are cavity photon, exciton 0−0 and exciton 0−1 fractions, respectively.

LPB, MPB, and UPB, respectively. The LPB has more photonic mixing fraction at small θ while the excitonic fraction (ex0–0) increases at larger θ. In the MPB, there is an excitonic transition from ex0–0 to ex0–1 while the photon contribution is small and almost flat as a function of θ. The UPB is more excitonic (ex0–1) at small θ and becomes photonic with increasing θ. As a result, the large Rabi-splitting energies ($2\hbar\Omega$) of ~250 meV owing to strong coupling between the cavity-photon and the both excitons demonstrate a stable formation of cavity polaritons in the microcavity EL device at room temperature. The obtained strong coupling regime is discussed with the cavity Q factor of the microcavity. The Q factor of the fabricated device is evaluated by

$$Q = 2\pi n_{\text{eff}}/\lambda \left[\alpha - \frac{1}{L_{\text{cav}}} \ln(\sqrt{R_{\text{top}}R_{\text{bot}}}) \right], \qquad (4.3)$$

where λ is the resonance wavelength, R_{top}, and R_{bot} are the reflectance of the top and bottom mirrors, respectively [R_{top}(Au) = ~0.8, R_{bot}(DBR) = ~0.99]. L_{cav} is the cavity length including a mirror penetration depth in the DBR. The cavity loss α was ignored. From **formula (4.3)**, a Q factor value of ~111 was obtained for the microcavity device. For strong exciton-photon coupling, the following inequality should be satisfied:

$$Q \gg \hbar\omega/2\hbar\Omega, \qquad (4.4)$$

where $\hbar\omega$ is exciton transition energy. The estimated values of $\hbar\omega_0/2\hbar\Omega_0 = 9.68$ and $\hbar\omega_1/2\hbar\Omega_1 = 10.7$ confirm to satisfy this condition for the present microcavity device. The Rabi-splitting energy ($2\hbar\Omega$) is generally described as

$$2\hbar\Omega \propto \left(\frac{fN}{V} \right)^{1/2}, \qquad (4.5)$$

where f, N, and V are the magnitude of the oscillator strength, the number of dipoles coupled in the cavity, and the photonic volume of the cavity, respectively. Compared to the single-crystal microcavity with high molecular orientation, the present vapor-deposited film results in
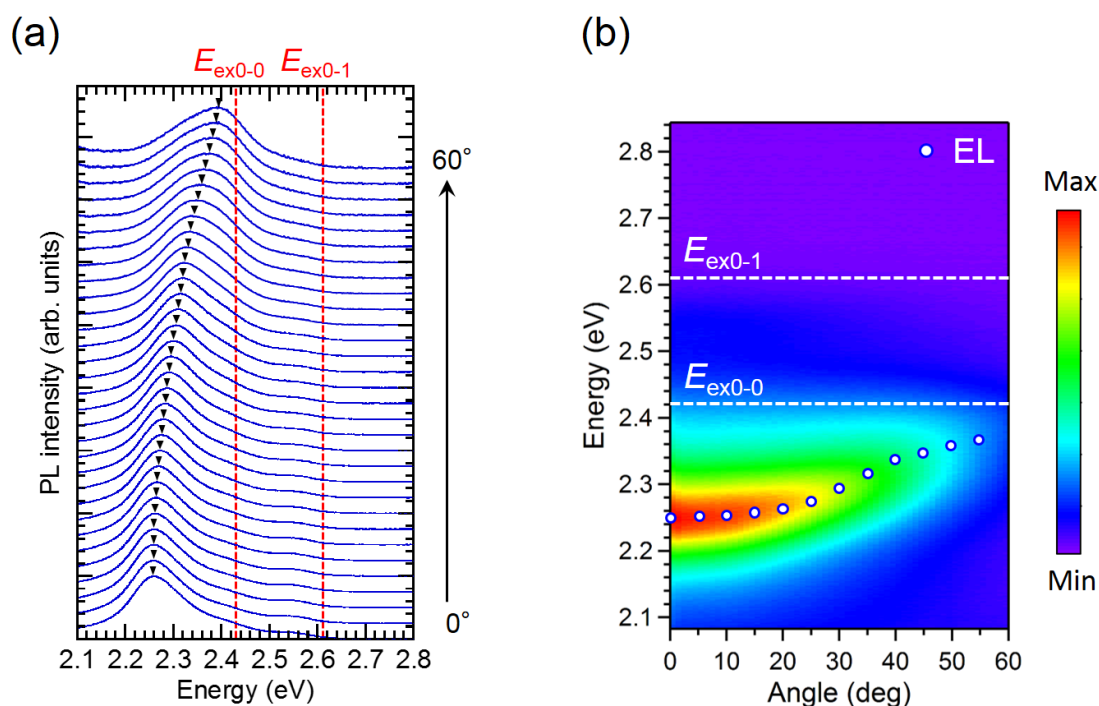
Fig. 4.5. (a) Angle-resolves PL spectra taken from microcavity EL device with 125 nm-thick BP2T-CN layer under ns-pulsed excitation. Closed triangles correspond to energy dispersion of LPB. (b) Contour map of PL spectra taken at 1° increments. Open circles show LPB peaks plotted from EL spectra in Fig. 4.8(a).

lower N, however, its thinner thickness contributes to reduce V to give the large Rabi splitting. The normalized coupling factor ($g = 2\hbar\Omega/\hbar\omega$) of the present microcavity device is about 10%. Further improvement in the molecular orientation and crystallinity in the vapor-deposited films is required to increase the Q factor and achieve an ultrastrong coupling regime ($g > 20\%$) based on cavity quantum electrodynamics (cavity-QED).

Next, angle-resolved PL measurements were performed under ns-pulsed excitation ($\lambda_{ex} = 355$ nm, 1.4 ns, 1 kHz). The excitation beam was incident normal to the bottom surface of the DBR/glass substrate, and the far-field emission from the top Au surface was collected as a function of emission angle θ. **Figure 4.5(a)** shows PL spectra taken at $0 < \theta < 60°$ with s-polarized excitation. The emission peak at $\theta = 0°$ appears at 2.26 eV. As marked with closed

triangles, this peak position is blue-shifted approaching to the 0–0 exciton energy ($E_{ex0-0} = 2.42$ eV) with increasing θ. In analogy to the angle-resolved reflection spectra [**Fig. 4.4(a)**], this PL dispersion is assigned to emission from the LPB. In addition, a weak emission dispersion corresponding to the MPB is faintly observed in the energy range between E_{ex0-0} and E_{ex0-1}. However, no UPB emission is visible, probably due to the fast energy relaxation to the lower polariton states. The contour map drawn from these PL spectra is shown in **Fig. 4.5(b)**. As is clearly seen in this angle-resolved PL map, the emission is mostly converged within the angle range of $\theta < 30°$ indicating that the created polaritons are efficiently relaxed into the lowest LPB state ($k = 0$) under optical excitation.

In order to further characterize the fabricated microcavity devices, the dependence of exciton-photon coupling phenomena on the cavity length was investigated by changing the BP2T-CN layer thickness as depicted in **Fig. 4.6**. With increasing thickness of the BP2T-CN layer, the PL bandwidth of the LPB increases, and the $E_{ph}(0)$ decreases [see **Figs. 4.7(a)** and **(b)**] since the magnitudes of negative detuning of $E_{ph}(0)$ from E_{ex0-0} and E_{ex0-1} increases.

Accordingly, both the Rabi-splitting energies of $2\hbar\Omega_0$ and $2\hbar\Omega_1$ become large with the increasing thickness of the BP2T-CN layer as shown in **Fig. 4.7(c)**. It is known for semiconductor quantum-well microcavities that the Rabi-splitting energy depends on the cavity length as

$$2\hbar\Omega \propto \left(\frac{d}{d + L_{DBR}}\right)^{1/2}, \tag{4.6}$$

where d and L_{DBR} are the thicknesses of the active layer and DBR mirror.[25] The present results qualitatively agree with it, therefore, the exciton-photon interaction can be controlled by changing the thickness of vapor-deposited organic layers.
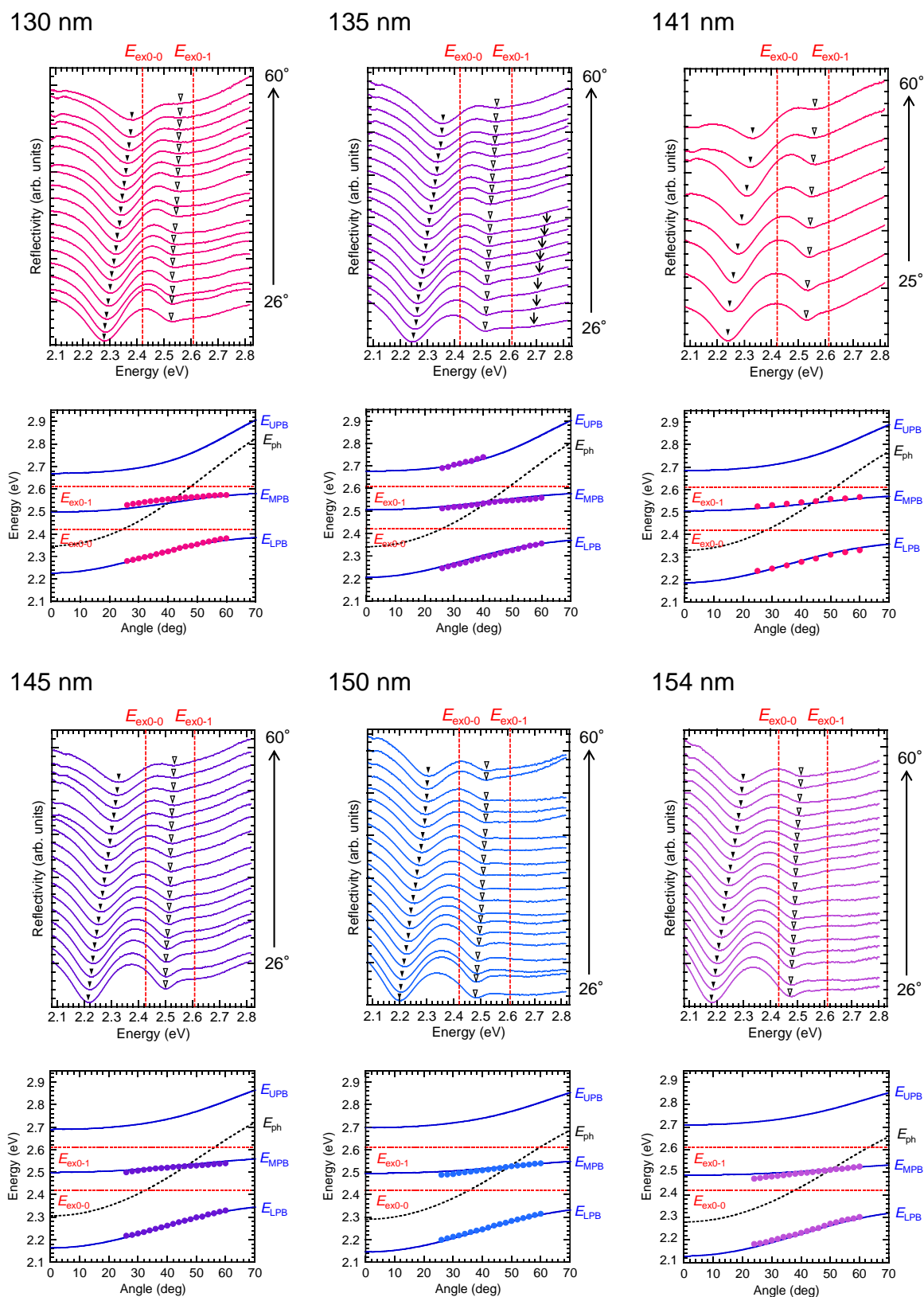
Fig. 4.6. Angle-resolved reflectance spectra and dispersion relations for microcavity EL devices with different BP2T-CN thicknesses.
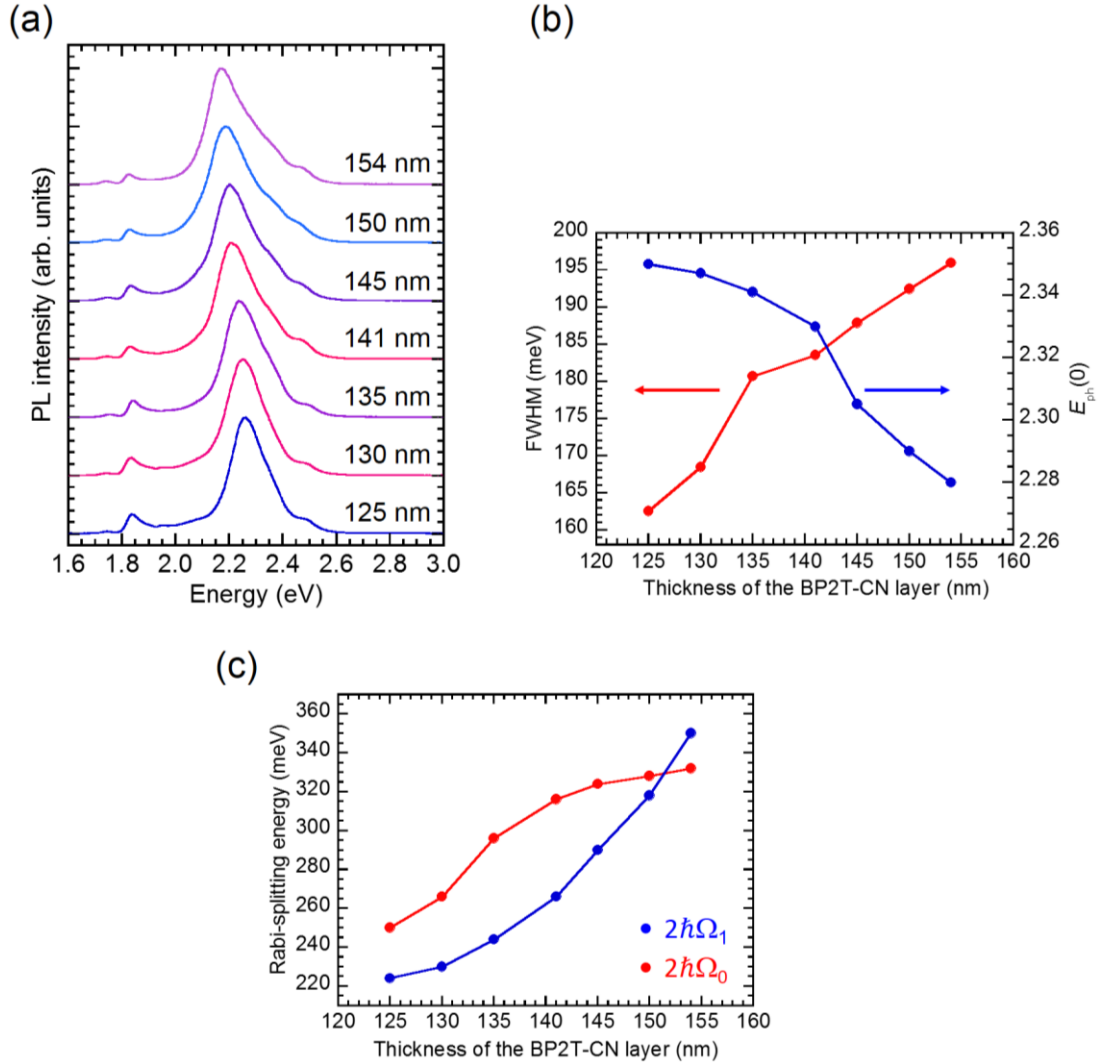
Fig. 4.7. (a) PL spectra taken at θ = 0° for microcavity EL devices with different BP2T-CN thicknesses. (b) Cavity-length dependences of $E_{ph}(0)$ (blue dots) and FWHM of LPB emission peak (red dots) for microcavity EL devices with different thicknesses of BP2T-CN layer. (c) Cavity-length dependences of $2\hbar\Omega_0$ (red dots) and $2\hbar\Omega_1$ (blue dots) determined from fitted exciton-polariton dispersions for microcavity EL devices with different thicknesses of BP2T-CN layer.

Next, the formation of exciton-polariton and resulting polariton emission in the microcavity device were examined under electrical excitation. **Figure 4.8(a)** displays the angle-resolved EL spectra taken from the microcavity EL device (Au/MoO₃/BP2T/BP2T-CN/ITO/DBR) with 125 nm-thick BP2T-CN layer at room temperature. The angle-dependent EL spectra are similar to those of the PL measurements [**Fig. 4.8(a)**, closed triangles], showing
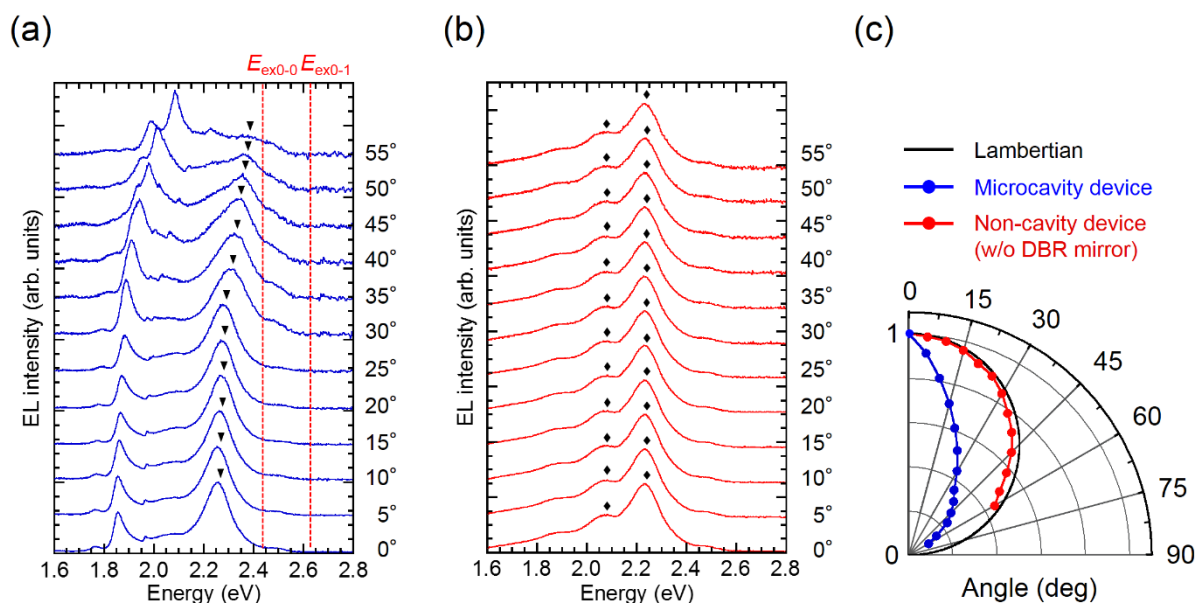
Fig. 4.8. Angle-resolved EL spectra for the microcavity EL device with 125 nm-thick BP2T-CN layer (a) and the non-cavity EL device (b) taken at bias voltage of 12 V (~80 mA/cm^2). Closed triangles in (a) correspond to energy dispersion of LPB. (c) Spatial distribution of angle dependent emission intensity for the microcavity EL device with 125 nm-thick BP2T-CN layer (blue dots) and the non-cavity EL device (red dots). The black solid line shows a curve of Lambertian distribution.

anticrossing polaritonic characteristics. The emission peak at 2.26 eV at $\theta = 0°$ corresponding to the LPB emission shifts to the higher energy approaching to E_{ex0-0}. Furthermore, weak emissions assigned to the MPB are visible in the energy range between E_{ex0-0} and E_{ex0-1}. Another peak at around 1.86 eV comes from the lower order mode which does not contribute to strong coupling, and additional peaks at around 1.76 and 1.94 eV are caused by the transmission leak from the bottom DBR mirror [**Fig. 4.3(b)**]. The same measurement using a non-cavity EL device without the DBR mirror (Au/MoO$_3$/BP2T/BP2T-CN/ITO) indicates no such angular dispersion as shown in **Fig. 4.8(b)**, and its EL spectrum is consistent with the PL spectrum of the BP2T-CN film. These results clearly demonstrate that cavity-polaritons are formed in the microcavity EL devices under electrical excitation as well as optical excitation. It is also noted that the EL intensity of the LPB emission in the
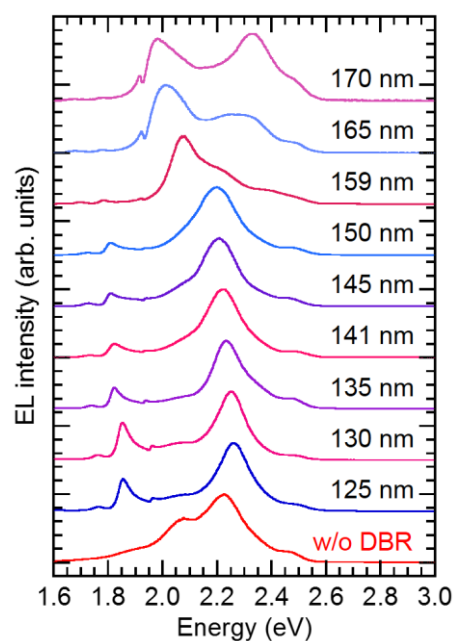
Fig. 4.9. EL spectra taken at θ = 0° for microcavity EL devices with different BP2T-CN thicknesses and for the non-cavity EL device w/o DBR.

microcavity device remarkably increases as the θ approaches to 0° [**Fig. 4.8(a)**] while that in the non-cavity EL device changes a little. **Figure 4.8(c)** shows spatial distribution of angle dependent emission intensity around 2.2–2.4 eV for the microcavity and non-cavity EL devices. The non-cavity EL device indicates a Lambertian-like spatial distribution typical for surface-emitting organic EL devices. By contrast, the EL intensity of the microcavity device is converged within smaller angles from the normal direction. This narrow convergence of the microcavity EL again suggests effective relaxation of cavity polaritons into the lowest LPB state.

The cavity-length dependence of polariton formation was also confirmed under electrical excitation as depicted in **Fig. 4.9**. EL spectra were collected at normal direction ($\theta = 0°$) from the microcavity EL devices with different thickness of the BP2T-CN layer. The emission peak corresponding to the LPB at 2.26 eV for 125 nm thickness is red-shifted to 1.97 eV for 170 nm thickness as the negative detuning of $E_{ph}(0)$ increases with increasing thickness of the BP2T-

CN layer. By contrast, the peak position of weak MPB emissions is almost constant in the energy range between E_{ex0-0} and E_{ex0-1}. When the film thickness of the BP2T-CN layer is over 165 nm, another emission peak emerges at the higher energy side. This additional peak is assigned to the LPB coupled with a higher order cavity photon mode.

Finally, excitation-density dependence of EL characteristics of the microcavity device was investigated. **Figures 4.10 (a)** and **(b)** display current density-voltage and luminance-current density characteristics, respectively, taken for the microcavity EL device with 125 nm-thick BP2T-CN layer. In the figures, those characteristics are also shown for the non-cavity EL device as a reference. Electrical properties for both devices are similar since their carrier injection, transport and recombination properties are not dependent on the existence of the bottom DBR mirror. In these *I−V* measurements, EL emission was observed from the top Au anode when the bias voltage and current density exceed ~6 V and ~0.3 mA/cm^2, respectively. Contrastingly, their luminance taken at the normal direction with a collection angle of 2° is remarkably higher for the microcavity device than the non-cavity EL device [**Fig. 4.8(b)**]. Some previous studies in organic microcavities, such as TDBC[15] and squaraine dye[26,27] have reported that their output intensities measured at the same current density are reduced compared to non-cavity EL devices. The reason for the reduced microcavity EL intensities has been attributed to the slow scattering of excitons into the polariton state, that is most excitons remain in the reservoir rather than being relaxed into the emissive polariton branches.[15,26,27] To avoid these relaxation bottleneck effects, it is necessary to optimize molecular assembling structure and device geometry for longer polariton lifetime and efficient condensation into $k = 0$ toward realizing electrically pumped organic polariton lasing.

Since organic EL is a current injection type device, in general, the luminance has a linear proportional relationship with the current density. However, both devices show superlinear

Fig. 4.10. Curent density-voltage (a) and luminance-curent density (b) characteristics for the microcavity EL device with 125 nm-thick BP2T-CN layer (blue dots) and the non-cavity EL device (red dots). Excitation-density dependence of PL (c) and EL (d) spectra for the microcavity EL device with 125 nm-thick BP2T-CN layer. The inset shows integrated PL and EL intensity of LPB emission around 2.26 eV as a function of current density, respectively. The black dotted line shows a linear dependence for eye guide.

increase of luminance with increasing the current density. As a well-known phenomenon, triplet-triplet annihilation (TTA) is involved in electrically injected emission process where the fusion of two excited triplet excitons ($T_1 + T_1$) gives a upconverted singlet exciton (S_1) and a ground state (S_0), as expressed by the following formula:

$$T_1 + T_1 \rightarrow S_1 + S_0,$$ (4.7)

The luminance of EL devices increases superlinearly with current density, because the S_1 exciton is generated in proportion to the square of T_1 density.[28] Therefore, the nonlinear luminance increase observed for the both microcavity and non-cavity devices is ascribed to the contribution of TTA to their electroluminescence. However, the superlinear inclination of the luminescence is considerably higher for the microcavity device than for the non-cavity EL device [**Fig. 4.10(b)**].

To make these characteristics clearer, the excitation-density dependences of PL and EL were also compared for the microcavity EL device as shown in **Figs. 4.10(c)** and **(d)**, respectively. PL and EL spectra were taken from the device with 125 nm-thick BP2T-CN layer at normal collection ($\theta = 0°$) as a function of excitation density. The PL spectra under fs-pulsed excitation (λ_{ex} = 397 nm, 200 fs, 1 kHz) indicate that their integrated PL intensity at the LPB peak at 2.26 eV increases linearly as a function of optical excitation density [**Fig. 4.10(c)**]. By contrast, its integrated EL intensity increases superlinearly as a function of current density with the ~1.7th power as shown in the inset. This superlinear inclement is again higher than the luminance inclement of the non-cavity device with the ~1.4th power [**Fig. 4.10(b)**]. These results suggest that the efficient relaxation of polaritons into the LPB in the present microcavity device would involve other contribution of electrically injected excitons more than expected from the TTA process. Formation of exciton-polariton is basically considered to be dominated by the radiative S_1 excitons with allowed electronic transition which can couple with light in the microcavity. It is still an open question, however, the strong polaritonic interaction between the injected excitons and confined light may cause incorporation of triplet excitons to the LPB formation through a kind of spin-orbit interaction induced by strong coupling between electromagnetic field of cavity photons and excitons. In the study for a GaAs polariton-LED, both polariton intensity in the PL and EL spectra shows a superliner increase with increasing

excitation density,[28] which is ascribed to polaritonic interaction even below the excitation threshold of polariton lasing. On the other hand, there has been no report on such a superlinear behavior for organic microcavities under electrical excitation. Therefore, it is believed that this similarity between inorganic and organic semiconductor materials is largely related to the contribution of triplet excitons in the organic microcavity under electrical excitation.

Further increase of current density in the present microcavity EL device results in a roll-off of the EL intensity [see also **Fig. 4.10(b)**], and a slight blue-shift ($\Delta E \sim 9.2$ meV) of the LPB emission peak was observed when the current density is beyond 100 mA/cm^2 as depicted in **Fig. 4.11**. A spectral blue-shift is known to be caused by polariton-polariton scattering under optical pumping when the polariton lasing transitions to the photon lasing regime.[8–12] On the other hand, as reported for polariton-LEDs with inorganic semiconductor materials,[29–32] polariton EL peaks show a progressive transition to the weak coupling regime due to exciton screening at high carrier density accompanying blue-shift of LPB. In the present electrical excitation of the microcavity EL device, the integrated intensity and bandwidth of the LPB emission shows no threshold for polariton lasing. The excited density is still too low to reach polariton condensation, therefore, the observed roll-off and blue-shift are probably attributed to the exciton screening by the injected carriers.

In the present vapor-deposited active layer of BP2T-CN, the suitable lying molecular orientation probably contributes to strong coupling between the oligomer excitons with large transition dipoles and favorably polarized photons in the microcavity device. However, such oriented molecular domains are limited within a microcrystalline grain in the film. Further improvement to realize polariton lasing demands the development of film growth techniques enabling large-domain crystallization with favorable orientation responsible for spatially interacted condensation of cavity polaritons. As mentioned above, exciton screening by
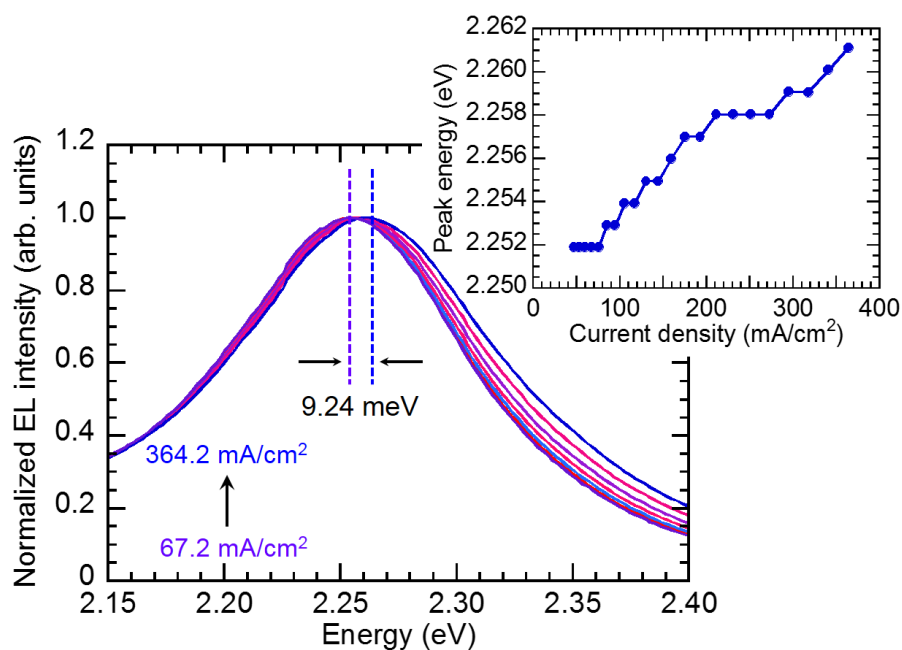
Fig. 4.11. Normalized EL spectra of LPB emission taken at varied current densities. Dashed purple and blue lines show energy peak positions at 67.2 and 364.2 mA/cm², respectively. The inset shows peak energy of LPB emission as a function of current density.

carriers known as singlet-polaron annihilation in organic EL devices[33–35] should be solved to achieve high current-density pumping. In order to reduce the exciton screening, the exciton diffusion and carrier injection regions should be separated, for example by means of introducing locally patterned injection electrodes. [34,36]

4.4   Conclusions

Exciton-polariton electroluminescence from organic microcavity devices with cyano-substituted TPCO was observed at room temperature. Although the fabricated EL devices using vapor-deposited films have a low Q factor, a strong coupling regime with a large Rabi-splitting energy (~250 meV) was obtained under both optical and electrical excitations. The angle-resolved spectroscopy indicated efficient relaxation of exciton-polaritons into the bottom of LPB ($k = 0$), bypassing bottleneck effects. Moreover, cavity-length dependences of Rabi-

splitting energy and polaritonic EL wavelength was confirmed by detuning the exciton-photon coupling. Furthermore, the superlinear inclement of polaritonic EL intensity was indicated for the first time strongly suggesting a contribution of electrically injected triplet excitons to the polariton formation. Consequently, the TPCO derivatives are promising candidate materials for organic polariton lasers owing to their unique molecular orientation even in vapor-deposited films. Towards the accomplishment of an electrically pumped organic polariton laser, further improvements such as the introduction of top DBR mirror, electron injection/transport layers and development of large-domain crystal growth techniques are necessary.

References

[1] A. Imamoglu, R. J. Ram, S. Pau, Y. Yamamoto. *Phys. Rev. A* **1996,** 53, 4250.

[2] H. Deng, G. Weihs, C. Santori, J. Bloch, Y. Yamamoto, *Science* **2002,** 298, 199.

[3] J. Kasprzak, M. Richard, S. Kundermann, A. Baas, P. Jeambrun, J. M. J. Keeling, F. M. Marchetti, M. H. Szymańska, R. André, J. L. Staehli, V. Savona, P. B. Littlewood, B. Deveaud, L. S. Dang, *Nature* **2006,** 443, 409.

[4] S. Christopoulos, G. B. H. von Högersthal, A. J. D. Grundy, P. G. Lagoudakis, A. V. Kavokin, J. J. Baumberg, G. Christmann, R. Butté, E. Feltin, J.-F. Carlin, N. Grandjean, *Phys. Rev. Lett.* **2007,** 98, 126405.

[5] G. Nardin, K. G. Lagoudakis, M. Wouters, M. Richard, A. Bass, R. Andé, L. S. Dang, B. Pietka, B. Deveaud-Plédran, *Phys. Rev. Lett.* **2009,** 103, 256402.

[6] D. Bajoni, *J. Phys. D: Appl. Phys.* **2012,** 45, 313001.

[7] T. C. Lu, Y. Y. Lai, Y. P. Lan, S. W. Huang, J. R. Chen, Y. C. Wu, W. F. Hsieh, H. Deng, *Opt. Express* **2012,** 20, 5530.

[8] S. Keńa-Cohen, S. R. Forrest, *Nat. Photonics* **2010,** 4, 371.

[9] K. S. Daskalakis, S. A. Maier, R. Murray, S. Keńa-Cohen, *Nat. Mater.* **2014,** 13, 271.

[10] J. D. Plumhof, T. Stöferle, L. Mai, U. Scherf, R. Mahrt, *Nat. Mater*. **2014,** 13, 247.

[11] T. Cookson, K. Georgiou, A. Zasedatelev, R. T. Grand, T. Virgili, M. Cavazzini, F. Galeotti, C. Clark, N. G. Berloff, D. G. Lidzey, P. G. Lagoudakis, *Adv. Opical Mater*. **2017,** 5, 1700203.

[12] G. G. Paschos, N. Somaschi, S. I. Tsintzos, D. Coles4 J. L. Bricks, Z. Hatzopoulos, D. G. Lidzey, P. G. Lagoudakis, P. G. Savvidis, *Sci. Rep*. **2017,** 7, 11377.

[13] J. R. Tischler, M. S. Bradley, V. Bulović, J. H. Song, A. Nurmikko, *Phys. Rev. Lett.* **2005,** 95, 036401.

[14] G. H. Lodden, R. J. Holmes, *Appl. Phys. Lett.* **2011,** 98, 233301.

[15] N. Christogiannis, N. Somaschi, P. Michetti, D. M. Coles, P. G. Savvidis, P. G. Lagoudakis, D. G. Lidzey, *Adv. Optical Mater.* **2013,** 1, 503.

[16] C. R. Gubbin, S. A. Maier, S. Keńa-Cohen, *Appl. Phys. Lett.* **2014,** 104, 233302.

[17] S. Gambino, M. Mazzeo, A. Genco, O. D. Stefano, S. Savasta, S. Patanè, D. Ballarini, F. Mangione, G. Lerario, D. Sanvitto, G. Gigli, *ACS Photonics* **2014,** 1, 1042.

[18] A. Graf, M. Held, Y. Zakharko, L. Tropf, M. C. Gather, J. Zaumseil, *Nat. Mater*. **2017,** 16, 911.

[19] M. Held, A. Graf, Y. Zakharko, P. Chao, L. Tropf, M. C. Gather, J. Zaumseil, *Adv. Optical Mater.* **2018,** 6, 1700962.

[20] Y. Tanaka, K. Goto, K. Yamashita, T. Yamao, S. Hotta, F. Sasaki, Y. Yanagi, *Appl. Phys. Lett.* **2015,** 107, 163303.

[21] K. Goto, K. Yamashita, Y. Yanagi, T. Yamao, S. Hotta, *Appl. Phys. Lett.* **2016,** 109, 061101.

[22] T. Nishimura, K. Yamashita, S. Takahashi, T. Yamao, S. Hotta, H. Yanagi, M. Nakayama, *Opt. Lett*. **2018,** 43, 1047.

[23] K. Yamashita, U. Huynh, J. Richter, L. Eyre, F. Deschler, A. Rao, K. Goto, T. Nishimura, T. Yamao, S. Hotta, H. Yanagi, M. Nakayama, R. H. Friend, *ACS Photonics* **2018,** 5, 2182.

[24] R. Hatano, K. Goto, K. Yamashita, F. Sasaki, H. Yanagi, *Jpn. J. Appl. Phys.* **2017**, 56, 04CL02.

[25] A. Tredicucci, Y. Chen, V. Pellegrini, M. Börger, L. Sorba, F. Belttram, F. Bassani, *Phys. Rev. Lett.* **1995,** 75, 3906.

[26] M. Mazzeo, A. Genco, S. Gambino, D. Ballarini, F. Mangione, O. Di. Stefano, S. Patanè, S. Savasta, D. Sanvitto, G. Gigli, *Appl. Phys. Lett.* **2014,** 104, 233303.

[27] S. Gambino, A. Genco, G. Accorsi, O. D. Stefano, S. Savasta, S. Patanè, G. Gigli, M. Mazzeo, *Appl. Mater. Today* **2015**, 1, 33.

[28] C. Ganzorig, M. Fujiwara, *Appl. Phys. Lett.* **2002,** 81, 3137.

[29] S. I. Tsintzos, N. T. Pelekanos, G. Konstantinidis, Z. Hatzopoulos, P. G. Savvidis, *Nature* **2008,** 453, 372.

[30] D. Bajoni, E. Semenova, A. Lemaître, S. Bouchoule, E. Wertz, P. Senellart, J. Bloch, *Phys. Rev. B* **2008,** 77, 113303.

[31] S. I. Tsintzos, P. G. Savvidis, G. Deligeorgis, Z. Hatzopoulos, N. T. Pelekanos, *Appl. Phys. Lett.* **2009,** 94, 071109.

[32] T-C. Lu, J-R. Chen, S-C. Lin, S-W. Huang, S-C, Wang, Y. Yamamoto, *Nano Lett.* **2011,** 11, 2791.

[33] M. A. Baldo, D. F. O'Brien, M. E. Thompson, S. R. Forrest, *Phys. Rev. B* **1999**, 60, 14422.

[34] Y. Setoguchi, C. Adachi, *J. Appl. Phys.* **2010,** 108, 064516.

[35] C. Murawski, K. Leo, M. Gather, *Adv. Mater.* **2013,** 25, 6801.

[36] K. Hayashi, H. Nakanotani, M. Inoue, K. Yoshida, O. Mikhnenko, T-Q. Nguyen, C. Adachi, *Appl. Phys. Lett.* **2015,** 106, 093301.

Chapter 5

Fabrication of Organic Crystalline Films by Vaporized Film Deposition Method and Their Lasing and EL Characteristics

---

In Chapter 3–4, organic EL devices were fabricated using vapor-deposited film. However, their morphology composed of microcrystal grains is not feasible for amplified emission under optical excitation. In order to obtain optically pumped lasing, it is necessary to prepare single crystalline thin films. In this Chapter, a crystalline film growth technique for organic materials called vaporized film deposition (VFD) is proposed. This method consists of two simple step: vapor-depositing a microcrystalline film on a substrate, then transferring it on another substrate by heating under vacuum. In this study, BP2T-CN is first vapor-deposited on a glass substrate. By facing another substrate with a spacing of ~1 mm against the deposited BP2T-CN film and heating, the BP2T-CN film was vaporized and transferred into a polycrystalline film composed of single-crystal grains with a size of 5–20 μm. This method enables to fabricate homogeneous polycrystalline films under controlled thickness. Consequently, optically pumped lasing and EL characteristics from this polycrystalline films are observed.

110

5.1   Introduction

In the previous Chapters, p-n-junction-type organic EL devices using vapor-deposited films of p-type BP2T and n-type BP2T-CN were fabricated. Their EL performance was considerably improved by both lying orientation of their molecular axes on the substrate by depositing the n-type BP2T-CN layer first on the ITO substrate. However, the luminance was rolled-off as the current density was increased and amplified EL was not observed.

To achieve light amplification in these EL devices, crystallization of the TPCO layers is required to improve the efficiency of carrier injection and transfer as well as light confinement in a cavity structure. As one of methods to directly fabricate crystalline films on substrate, epitaxial growth[1–5] and high temperature deposition[6,7] of TPCOs have been reported. However, it is difficult to grow homogeneous crystalline films with controlled thickness by those methods. T. Yamao *et al.* have reported an improved vapor-deposition method to fabricate FET devices with TPCO films.[8,9] In their method, the polycrystalline growth was promoted by placing the TPCO source close to the substrate surface. By slight modification of this method, a vaporized film deposition (VFD) method which uses a pre-deposited film as the TPCO source to grow homogeneous polycrystalline films was developed. The obtained films were characterized by fluorescence microscopy, XRD, and then their light-emitting properties were measured under optical pumping with a pulsed laser. Furthermore, p-n heterojunction type organic EL devices with an active layer of this BP2T-CN crystalline film was preliminary fabricated.

5.2   Experimental Section

Sample preparation and crystal growth:

Bare and ITO-coated glass slides (10×10 mm^2, 1 mm in thickness) were used as substrate. The substrates were cleaned through ultrasonication in a neutral detergent, acetone, and

(a)

(b)
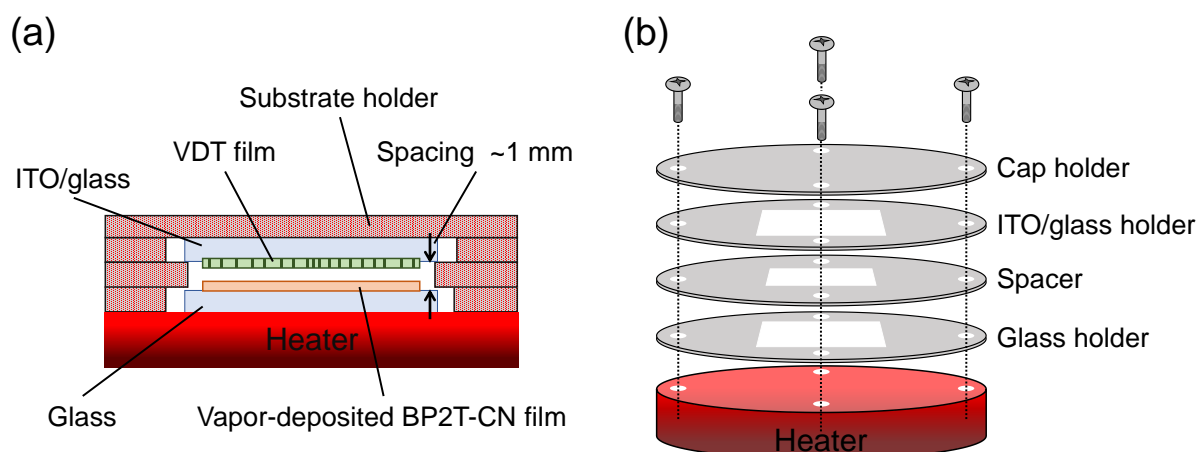
Fig. 5.1. Schematic diagrams of vaporized film deposition (VFD) apparatus (a) and its substrate holder (b). The distance between to substrates is 1 mm or less.

methanol for 15, 15, and 30 min, respectively, and were exposed to UV-ozone treatment for 20 min. **Figures. 5.1(a)** and **(b)** show schematic diagrams of the VFD apparatus. First, BP2T-CN was vapor-deposited on the glass substrate from a resistively heated quartz crucible under a vacuum of ~2.0×10^{-4} Pa. The deposition rate and film thickness of the BP2T-CN film were adjusted to ~0.1 nm/s and ~1 μm, respectively, by monitoring with a quartz crystal microbalance. The deposited thickness was confirmed with a surface profiler (Kosaka Laboratory ET200). This BP2T-CN/glass sample was placed on a resistively heated holder, and an ITO/glass substrate was faced down onto the BP2T-CN/glass surface with a spacing of ~1 mm. By heating at 250 °C for 40 min under vacuum ~2.0×10^{-4} Pa, the BP2T-CN film was vaporized and transferred from the bottom glass to the top ITO/glass substrate and thermally treated on the upper substrate holder (~1 mm in thickness) made of stainless.

As a reference for PL characterization, a single-crystal BP2T-CN sample was prepared by the PVT method as described in Chapter 2.

Crystal characterization:

Fluorescence images, PL spectra, surface morphology, crystalline structure and molecular

orientation of the VFD films were described in Chapter 3.

Optical measurement:

Optically pumped PL measurements were described in Chapter 2. The excitation beam with a stripe shape (spot size: 50 μm in length, 20 μm in width) was incident with an angle of 60° against the sample plane. The PL signal emitted from the film edge of the VFD sample was collected with a liquid-N_2-cooled CCD spectrometer in the direction parallel to the sample surface.

Fabrication and evaluation of organic EL devices with crystalline film:

Glass substrates (10×10 mm^2) coated with a stripe pattern (0.15×7 mm^2, 150 nm-thick) of ITO were used. After fabrication of the BP2T crystalline film on this ITO/glass substrate by the VFD method, BP2T (100 nm) was vapor-deposited with a rate of 0.5 Å/s under a vacuum of ~2.0×10^{-4} Pa. Finally, Au anode (3×10 mm^2, 50 nm-thick) was deposited through a stainless steel shadow mask aligned to cross the ITO cathode under a vacuum of ~2.0×10^{-4} Pa. The completed device has an emission area of 0.15×3 mm^2. EL measurements of the fabricated devices were carried out with a probe system installed in a vacuum chamber (1.0×10^{-3} Pa), and current−voltage (I−V) characteristics were obtained with a source measure unit (Agilent B2902). EL spectra were recorded through the Au anode using a CCD multichannel spectrometer (Hamamatsu Photonics PMA-12).

5.3. Results and discussion

Fluorescence micrographs of the VFD film of BP2T-CN are shown in **Fig. 5.2**. As a result of the VFD process, a polycrystalline film composed of 5−20 μm grains was grown on the ITO/glass substrate. In the fluorescence micrographs taken with vertical [**Fig. 5.2(b)**] and
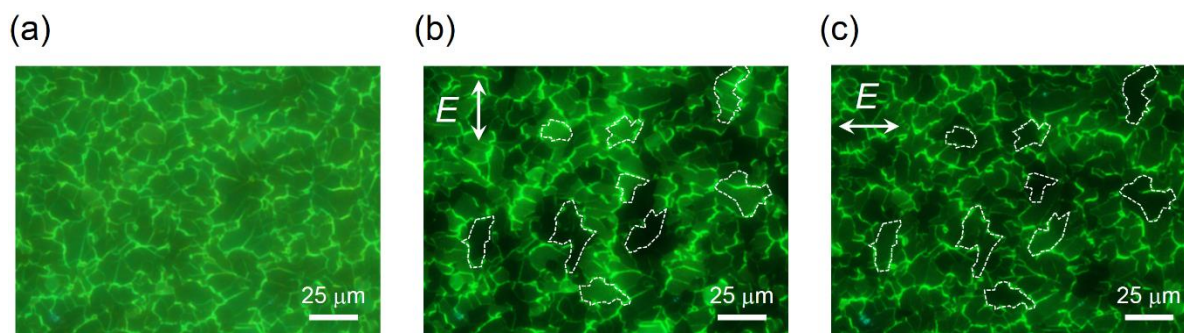
Fig. 5.2. Fluorescence micrographs of the VFD film of BP2T-CN taken without polarizer (a), with vertical (b) and horizontal (c) polarizations. The crystallites marked with dashed line indicate single crystal domains.
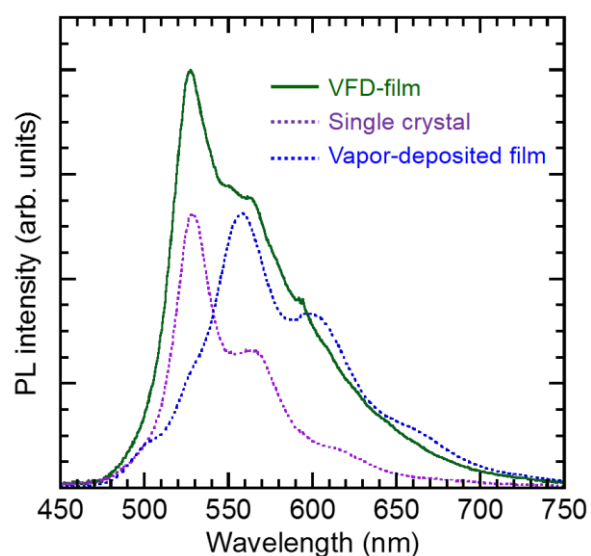
Fig. 5.3. Fluorescence spectrum of the VFD film of BP2T-CN together with PL spectra of single crystal (dashed purple) and vapor-deposited film (dashed blue) of BP2T-CN.

horizontal [**Fig. 5.2(c)**] polarization of the electric field indicates that the brightness of crystal

images changes by the polarization directions. It demonstrates that each grains consist of single

crystals. **Figure. 5.3** shows PL spectra of this VFD film (solid green) together with the

reference samples of a single-crystal BP2T-CN prepared by the vapor-phase growth (dashed

purple) and a vapor-deposited BP2T-CN film before the VFD procedure (dashed blue). The

vapor-deposited BP2T-CN film exhibits emission peaks at around 559 and 595 nm which are

assigned to the 0−1 and 0−2 $\pi-\pi^*$ transition, respectively, as presented in Chapter 2. By
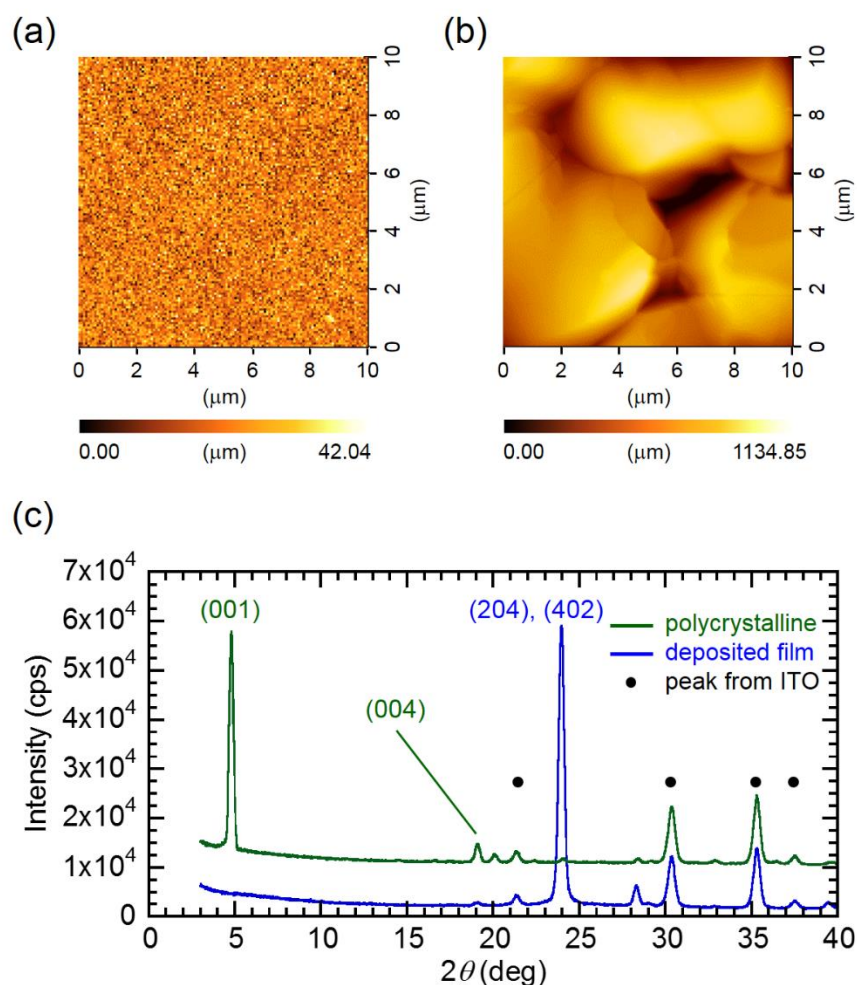
Fig. 5.4. (a) AFM images of the vapor-deposited film (a) and the VFD film (b) of BP2T-CN. (c) XRD patterns of the vapor-deposited film (blue) and the VFD film (green).

contrast, the VFD film indicates the 0–1 and 0–2 transitions at 530 and 561 nm, respectively.

Their emission peak wavelengths coincide with those of the single-crystal BP2T-CN. Therefore,

it confirms that each grains in the VFD film consist of single-crystal BP2T-CN.

   Figures 5.4(a) and **(b)** show AFM images of the vapor-deposited and VFD film of BP2T-

CN scanned over an area of 10×10 μm^2, respectively. The BP2T-CN vapor-deposited and

VFD films are composed of grains with a size larger than 0.2 and 5 μm with an average surface

roughness of 5.38 and 157 nm, respectively. **Figure 5.4(c)** displays XRD patterns of the vapor-

deposited film (blue) and the VFD film (green) on ITO/glass substrate. In the pattern of the

vapor-deposited film, the highest diffraction peak appears at 23.9° corresponding to the spacing

of d = 3.71 Å. According to the crystal structure of BP2T-CN (monoclinic, $P2_1$, a = 18.3994, b = 7.2397, c = 18.4431 Å, β = 100.572°), this peak is assigned to its (204) or (402) plane. It indicates that the molecular axis of BP2T-CN in the vapor-deposited film is almost lying with an angle of 25°. Since the transition dipole moment between the HOMO and LUMO of BP2T-CN is parallel to the molecular axis, this lying molecular orientation of the vapor- deposited BP2T-CN film is favorable for surface emission from the device. On the other hand, the XRD pattern of the VFD film is exhibited a strong diffraction peak at 4.78° corresponding to d = 18.5 Å and its higher-order reflections up to the eighth were observed. This peak is assigned to the (001) plane, indicating that the molecular axis in the VFD film is obliquely standing with an angle of 40° against the substrate. It is considered that the molecular orientation becomes a little upright in the VFD film since the VFD process undergoes at higher substrate temperature. This change in the molecular orientation probably causes the difference in their PL spectra shown in **Fig. 5.3**.

   Figure. 5.5(a) shows excitation density dependence of PL spectra of the VFD film optically pumped with a femtosecond pulsed laser at room temperature. As the excitation density increases, the spectrum changes from a broad fluorescence band to a typical feature of ASE. The 0−1 emission is amplified into gain-narrowed peaks with a FWHM of ~1 nm. In the inset of **Fig. 5.5(a)**, integrated intensity of the 0−1 band is plotted as a function of the excitation density. It indicates a threshold density for light amplification is estimated to be 205 $\mu J/cm^2$. In the high resolution measurement (grating of 1800/nm), multimode lasing oscillations are observed in the 0−1 band above the threshold as shown in **Fig. 5.4(b)**.

   Since the energy intervals between those lasing peaks are not constant (Δv = 16.3−41.9 cm^{-1}), the origin of this lasing is not a simple mode of F−P resonation but rather multiple reflection modes in one or some of single-crystal grains. The Q factor of the cavity is estimated to be 720−1170 from the Δv and the FWHM of the lasing peak. Although this Q factor is lower
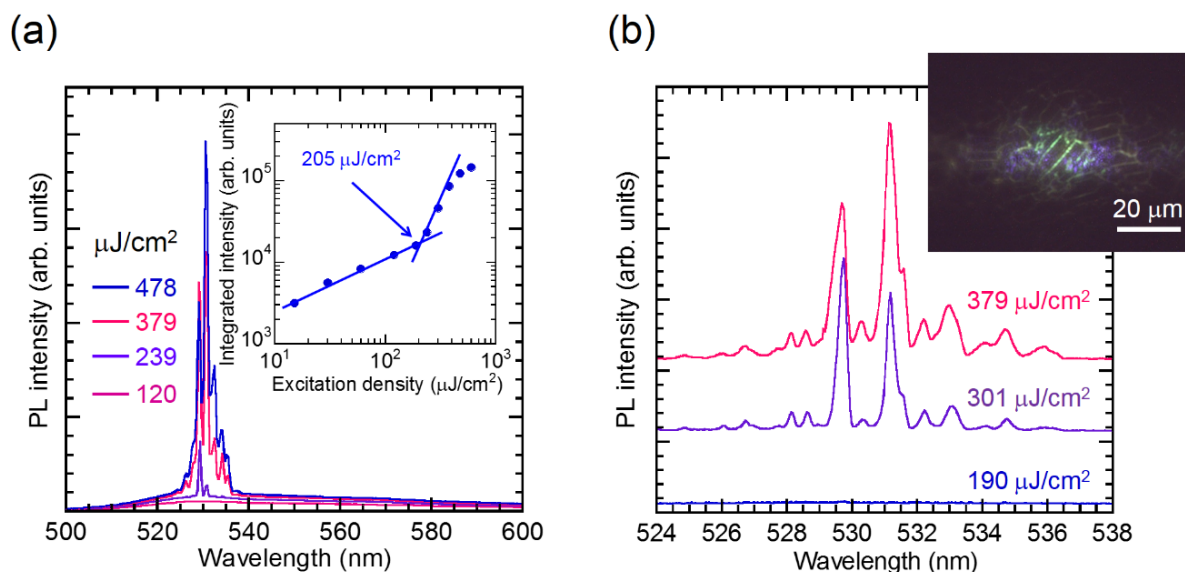
Fig. 5.5. (a) Excitation density dependence of PL spectra of the VFD film of BP2T-CN. The inset shows excitation density dependence of integrated 0–1 band intensity. (b) Excitation density dependence of high-resolution PL spectra at the 0–1 band.

than those for the F–P lasing of single-crystal TPCO derivatives ($Q = 1860$–4500)[10–14], the simple VFD method is feasible to yield polycrystalline cavities which demonstrate optically pumped lasing.

The organic EL device (Au/BP2T/BP2T-CN/ITO) was fabricated with the BP2T vapor-deposited film onto the VFD film of BP2T-CN. Although this *I–V* characteristic is inferior compared with EL devices using vapor-deposited p-n film as mentioned in Chapter 3, EL characteristic was obtained with emission peaks at around 530 and 561 nm as depicted in **Fig. 5.6**. The EL spectrum at 28 V is consistent with the 0–1 and 0–2 emission band in the PL spectrum of the BP2T-CN VFD film. The electrons injected from the ITO cathode are accumulated in the BP2T-CN grains and recombine with the holes transported from the BP2T layer as same as in the EL devices using vapor-deposited p-n films. Due to the obliquely lying molecular orientation of BP2T-CN and thicker film thickness in this polycrystalline VFD film, the EL intensity is lower than those of the vapor-deposited p-n films. In order to improve the
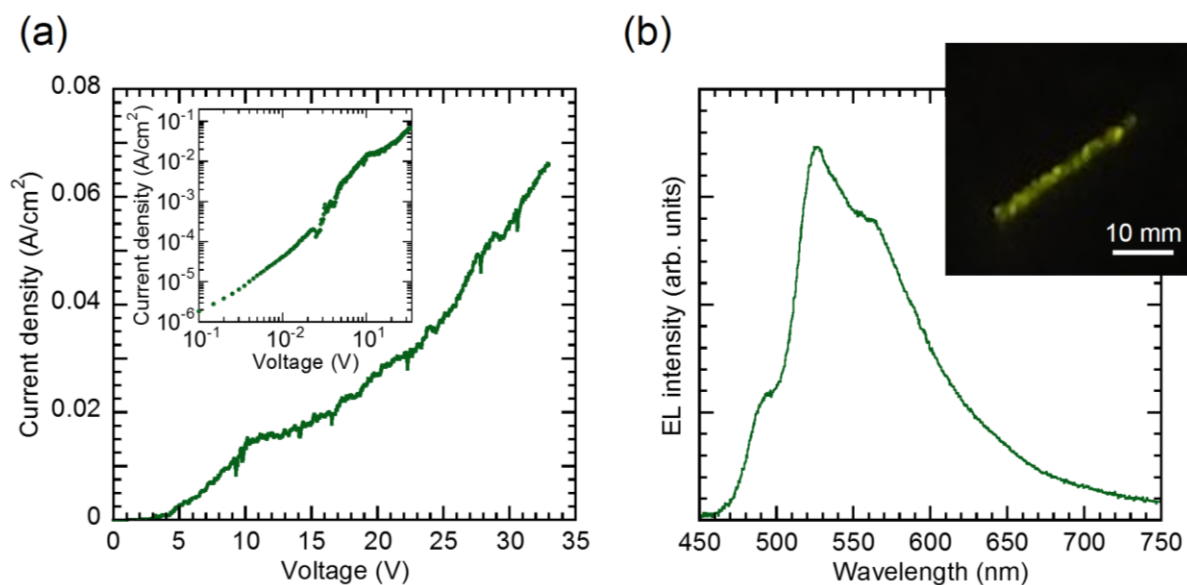
Fig. 5.6. (a) Current−voltage characteristics of the organic EL device with the BP2T-CN polycrystalline VFD film. The inset shows its double logarithmic plot. (b) EL spectrum of the EL device with the BP2T-CN polycrystalline VFD film. The inset shows photographs of the EL device under bias application at 28 V.

EL characteristics of the VFD film, the VFD conditions should be considered to enable lying molecular orientation and thinner film growth with larger single crystal grains.

5.4   Conclusions

Using the simple VFD method, the vapor-deposited microcrystalline film of BP2T-CN is successfully converted to the polycrystalline film. This method enables us to fabricate homogeneous films composed of single-crystal grains in size of 5−20 μm. Consequently, optically pumped lasing based on light confinement in the crystal grain cavity was observed. Compared to other growth methods for TPCO crystals, the crystallite thickness can be controlled by changing the pre-deposited film in the VFD process. By further improvement of molecular orientation and grain size, this method could provide a useful fabrication process for organic thin film devices.

Reference

[1]   H. Yanagi, T. Morikawa, *Appl. Phys. Lett.* **1999,** 75, 187.

[2]   H. Yanagi, T. Morikawa, S. Hotta, K. Yase, Q. Dong, *Adv. Mater.* **2001,** 13, 767.

[3]   H. Yanagi, Y. Araki, T. Ohara, S. Hotta, M. Ichikawa, Y. Taniguchi, *Adv. Funct. Mater.* **2003,** 13, 767.

[4]   K. Hashimoto, F. Sasaki, S. Hotta, H. Yanagi, *J. Nanosci. Nanotechnol.* **2016,** 16, 3200.

[5]   K. Torii, T. Higuchi, K. Mizuno, K. Bando, K. Yamashita, F. Sasaki, H. Yanagi, *ChemNanoMat* **2017,** 3, 625.

[6]   Y. Ido, Y. Masumoto, F. Sasaki, M. Mori, S. Haraichi, S. Hotaa, *Appl. Phys. Express* **2010,** 3, 012702.

[7]   F. Sasaki, M. Mori, S. Haraichi, Y. Ido, K. Bando, Y. Masumoto, S. Hotta, *Org. Electron*, **2010,** 11, 1192.

[8]   T. Yamao, S. Ota, T. Miki, S. Hotta, R. Azumi, *Thin Solid Films,* **2008,** 516, 2527.

[9]   T. Yamao, K. Juri, A. Kamoi, S. Hotta, *Org. Electron*, **2009,** 10, 1241.

[10] M. Ichikawa, R. Hibino, M. Inoue, T. Haritani, S. Hotta, K. Araki, T. Koyama, Y. Taniguchi, *Adv. Mater.* **2005,** 17, 2073.

[11] T. Yamao, K. Yamamoto, Y. Taniguchi, T. Miki, S. Hotta, *J. Appl. Phys.* **2008,** 103, 093115.

[12] H. Mizuno, I. Ohnishi, H. Yanagi, F. Sasaki, S. Hotta, *Adv. Mater.* **2012,** 24, 2404.

[13] H. Mizuno, U. Haku, Y. Marutani, A. Ishizumi, H. Yanagi, F. Sasaki, S. Hotta, *Adv. Mater.* **2012,** 24, 5744.

[14] H. Mizuno, T. Maeda, H. Yanagi, H. Katsuki, M. Aresti, F. Quochi, M. Saba, A. Mura, G. Bongiovanni, F. Sasaki, S. Hotta, *Adv. Optical Mater.* **2014,** 2, 529.

Chapter 6

Summary and Future Works

Section 6.1

Summary of This Thesis

In this thesis, optically pumped lasing, organic electroluminescence (EL) devices and organic microcavity EL devices were investigated using thiophene/phenylene co-oligomer (TPCO) derivatives. These results indicate that TPCO derivatives are useful as organic semiconductor laser media, and they can contribute to the development of new organic optical devices such as electrically pumped polariton lasers in the future.

6.1.1   Summary of Chapter 2

Toward fabrication and evaluation of organic EL devices with p-n heterojunction, optical characteristics of single crystal of TPCO derivatives were investigated. 5,5'-bis(4-biphenylyl)-2,2'-bithiophene (BP2T) as p-type and cyano-substituted BP2T, 5,5'-bis(4'-cyanobiphenyl-4-yl)-2,2'-bithiophene (BP2T-CN) were chosen for p- and n-type organic semiconductors, respectively. This combination of both molecules with p-n semiconducting conduction enables p-n heterojunction type organic EL devices since the HOMO/LUMO energies of BP2T-CN are deepened by 0.39/0.50 eV compared to those of BP2T. Moreover, optically pumped multimode lasing was observed from their crystals based on light confinement in the planar crystal cavity and Fabry–Pérot (F–P) resonation a pair of the parallel crystal facets. From their photoluminescence (PL) spectra, single crystal cavities of BP2T and BP2T-CN show high

quality factor (Q ~2545, ~4500) and high group refractive index (n_g ~5.14, ~5.20), indicating their promising potential as organic semiconductor laser media.

6.1.2 Summary of Chapter 3

In Section 3.1, fabrication and evaluation of organic EL devices with bilayered vapor-deposited films of BP2T and BP2T-CN (Al:Li/BP2T-CN/BP2T/ITO) were first carried out. In the fabricated device, BP2T and BP2T-CN showed p- and n-type conduction, which were respectively, evaluated from the rectifying current-voltage characteristics, resulting EL from the BP2T-CN layer. However, XRD measurements indicated that the molecular axis of BP2T-CN obliquely lay on top of the standing BP2T molecular layer. Due to these molecular orientations, the EL intensity was still low, and it was concluded that the device structure should be improved.

In order to improve the EL performances, the inverted EL device structure (Au/BP2T/BP2T-CN/ITO) was fabricated using Au anode with a high work function in Section 3.2. When the BP2T-CN layer was first deposited onto the ITO/glass substrate, the EL characteristics and current density were significantly increased, compared to the previous EL device (Al:Li/BP2T-CN/BP2T/ITO), since both molecules tended to orient lying in each films and carrier injection and transport were improved. Consequently, this inverted device is used for the microcavity structure toward polariton lasing in Chapter 4.

In Section 3.3, organic EL devices with trilayered p-i-n structure were investigated using the vapor-deposited film of 5'''-bis(4-trifluoromethylphenyl)[2,2';5',2'';5'',2''']quaterthiophene (P4T-CF$_3$) as the i-layer in the p-n heterojunction type devices. Fabricated devices in which the BP2T layer was first deposited on the ITO/glass substrate (Al:Li/BP2T-CN/P4T-CF$_3$/BP2T/ITO) showed homogeneous EL. On the other hand, the device having opposite deposition order (Au/BP2T/P4T-CF$_3$/BP2T-CN/ITO) showed dotted emission from the P4T-CF$_3$ layer with

higher efficiency. XRD measurements suggested that the dotted morphology in the i-layer was caused by crystallization of lying P4T-CF$_3$ molecules on the BP2T-CN layer in which intermolecular $\pi-\pi$ stacking and electrostatic interaction between their electron-withdrawing cyano and trifluoromethyl groups played a significant role. Moreover, optically pumped lasing was observed for the solution-grown P4T-CF$_3$ single crystal, and a preliminary EL device was fabricated by inserting the P4T-CF$_3$ crystal between the p- (BP2T) and n- (BP2T-CN) layers.

6.1.3 Summary of Chapter 4

Organic microcavity EL devices (Au/MoO$_3$/BP2T/BP2T-CN/ITO/DBR) using distributed bragg reflector (DBR) mirror were fabricated based on the p-n junction device structure mentioned Section 3.2. Strong coupling between photons and excitons in the microcavity EL devices were examined under optical and electrical excitation. The formation of cavity polariton with a large Rabi-splitting energy ($2\hbar\Omega = 250$ meV) was evaluated by angle-resolved reflection, PL, and EL spectroscopies at room temperature. The convergence of EL dispersion of the lower polariton branch (LPB) at narrow angles demonstrated the effective relaxation of cavity polaritons to the bottom state ($k = 0$), bypassing bottleneck effects. The superlinear increase of EL intensity as a function of current density suggested the triplet-triplet annihilation process and the contribution of triplet excitons to the LPB formation. It was expected, however, that the strong polaritonic interaction between the injected excitons and confined light might cause incorporation of triplet excitons to the LPB formation through spin-orbit interaction induced by strong electromagnetic field of cavity photons.

6.1.4 Summary of Chapter 5

Toward the realization of the electrically pumped organic lasers, a crystalline film growth technique for organic materials called vaporized film deposition (VFD) method was proposed.

Using this simple VFD method, a vapor-deposited microcrystalline film of BP2T-CN was successfully converted to its polycrystalline film. Optically pumped lasing was observed from this polycrystalline film based on light confinement in each crystalline grains. Preliminary EL characteristics were obtained from the p-n junction devices with this polycrystalline BP2T-CN film.

Section 6.2
Future Works

Future works toward electrically pumped organic semiconductor laser devices with TPCO derivatives based on the results in this thesis are proposed as described below.

6.2.1 Organic Microcavity EL Devices with High Quality Factor

In Chapter 4, organic microcavity EL devices were investigated and strong exciton-photon coupling with a large Rabi-splitting energy (~250 meV) was obtained under both optical and electrical excitations. However, the Q factor of the microcavity was still low (~256) because of the Au/DBR mirror structure. In order to obtain higher Q factor in this device, both DBR/DBR full cavity structure is proposed. LiF or Liq (electron injection layer, EIL), BP2T-CN (electron transport layer, ETL, and emission layer, EML), BP2T (hole transport layer, HTL), and MoO_3 (hole injection layer, HIL) are consecutively vapor-deposited in this order onto the ITO/bottom DBR substrate as shown in **Fig. 6.1**. Thin film (~1 nm) of LiF or Liq is introduced to improve electron injection and molecular orientation of BP2T-CN. After deposition of MoO_3 layer, the ITO anode and top DBR consisting of SiO_2 and Ta_2O_5 thin films are deposited by the sputtering method. The optical constants and thickness of SiO_2/Ta_2O_5 multilayer are calculated by using finite-difference time-domain (FDTD) method and the transfer matrix method (TMM). The MoO_3 layer may play an important role to avoid a damage of organic layers when the ITO anode and top DBR are deposited. Using such a DBR/DBR full cavity structure, quasi-amplified emission, spectrally narrowed emission, and a modification of the radiative emission rate (Purcell effect) are expected as reported.[1,2] Then firstly, angle-resolved EL spectroscopy is performed using fabricated microcavity EL devices,

EL

Top mirror

ITO anode

MoO$_3$ (HIL)

BP2T (HTL)

BP2T-CN (ETL/EML)

LiF or Liq (EIL)

ITO cathode

Bottom mirror

Glass substrate
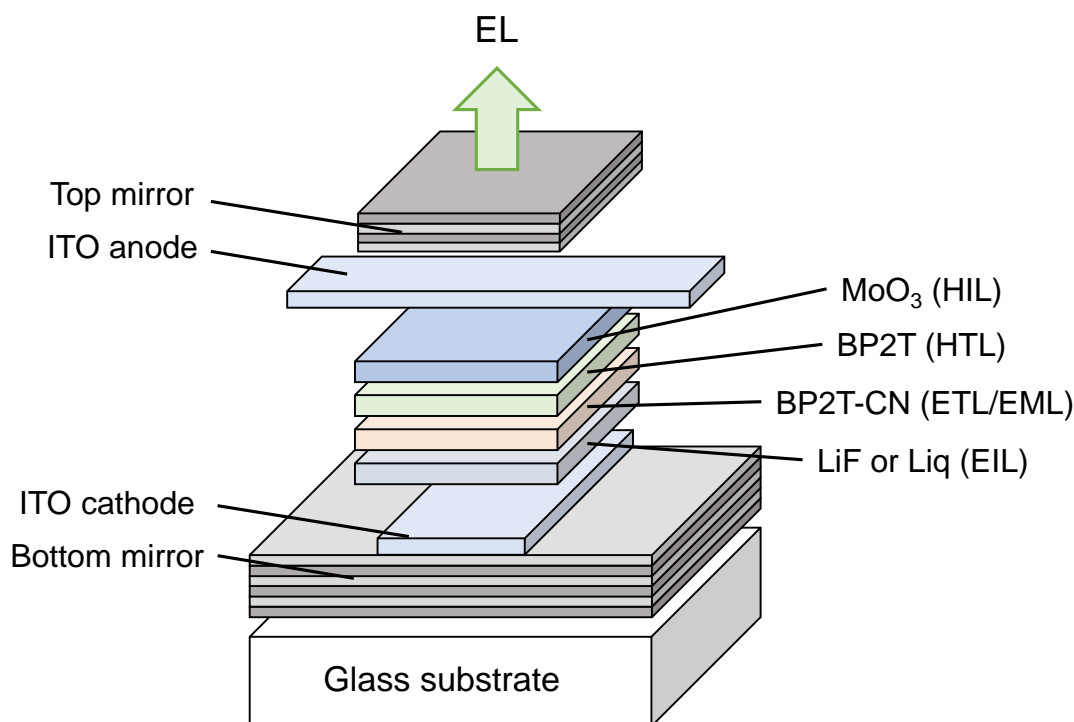
Fig. 6.1. Schematic diagram of microcavity EL device with DBR/DBR full cavity structure.

and the formation of cavity polariton is confirmed under electrical excitation. To prevent deterioration due to Joule heating and exciton annihilation by polarons, short pulse voltage measurements can be also attempted. Moreover, the possibility of a polariton lasing is examined by excitation-density dependence of EL characteristics, and the involvement of triplet excitons in the polariton formation is discussed from time-resolved PL measurements to clarify the mechanisms of light-matter interaction and strong coupling in organic microcavity under electrical excitation.

6.2.2   Vertical Microcavity Organic Light-emitting Field-effect Transistors

Since most of TPCOs are crystalized in platelet morphology in which their molecular axes are standing almost perpendicular against the crystal surface, TPCO crystals are favorably used for organic field-effect transistors (OFETs) in which the transport occurs in the transverse direction. As studied in this thesis, the BP2T-CN film with lying molecular orientation on the

EL

Ca drain
CsF
Ag source
BP2T polycllistaline film
● ● ● ● ● ● ● ● ○ ○ ○
Polystyrene
CYTOP insulator
+ + + + + + + - - - -
ITO gate
DBR mirror
Glass substrate
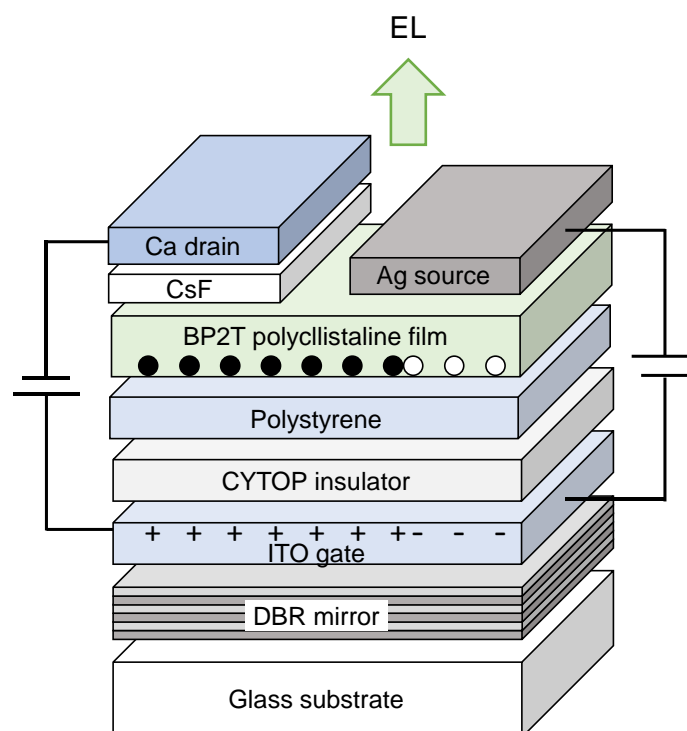
Fig. 6.2. Schematic diagram of vertical microcavity organic light-emitting field-effect transistor with BP2T-CN VFD film.

substrate is suitable for organic EL devices in which the carrier transport is in the vertical direction. As mentioned in Chapter 5, the BP2T-CN molecules in the polycrystalline film prepared by the VFD method are obliquely tilting with an angle of 40° against the substrate. This molecular orientation is suitable for vertical microcavity organic light-emitting FET[3,4] with vertical EL and transverse carrier transport. Recently, H. Shimotani and K. Tanigaki *et al.* have reported a gain-narrowed EL from ambipolar FET using single-crystal TPCO.[5–12] They used a device structure with Ca/LiF drain electrode and polystyrene buffer layer to improve electron injection and transport, and achieved high-density carrier injection (18 kA/cm^2). Referring their device structure, a vertical microcavity organic light-emitting FET with the VFD film of BP2T-CN is proposed as depicted in **Fig. 6.2**. The ITO and a bottom DBR mirror are deposited by the sputtering method where the ITO layer functions as the gate electrode. Amorphous fluoropolymer CYTOP having high transparency and a polystyrene layer are used

as a dielectric and a buffer layer, respectively. On the gate substrate, the BP2T-CN polycrystalline film is deposited using the VDF method. Finally Ag and Ca/CsF are deposited as source and drain electrodes, respectively, while the Ag layer also functions as the top mirror. The fabricated devices give EL in the area between the Ag drain and bottom mirror by controlling the gate bias. Using this device, optical and electrical measurements are carried out, and lasing property is discussed from current-density dependence of EL intensity and the linewidth of EL spectra.

References

[1]   X. Liu, H. Li, C. Song, Y. Liao, M. Tian, *Opt. Lett.* **2009,** 34, 503.

[2]   A. Genco, G. Giordano, S. Carallo, G. Accorsi, Y. Duan, S. Gambino, M. Mazzeo, *Org. Electron.* **2018,** 62, 174.

[3]   Y. Hu, L. Song, D. Li, J. Lin, X. Liu, *Org. Electron.* **2015,** 26, 92.

[4]   Y. Hu, J. Lin, L. Song, Q. Lu, W. Zhu, X. Liu, *Sci. Rep.* **2016,** 6, 23210.

[5]   H. Shimotani, T. Kanagasekaran, K. Kasai, S. Onuki, K. Tanigaki, *The 78th JSAP Autumm Meeting,* **2017,** 7a-A203-1 [In Japanese].

[6]   H. Shimotani, T. Kanagasekaran, K. Kasai, S. Onuki, K. Tanigaki, *Organic Solid Laser,* **2017,** RTM-17-59 [In Japanese].

[7]   H. Shimotani, T. Kanagasekaran, K. Kasai, S. Onuki, D. Miura, K. Tanigaki, *The65th JSAP Spring Meeting,* **2018,** 20a-D102-1 [In Japanese].

[8]   K. Tanigaki, T. Kanagasekaran, H. Shimotani, K. Kasai, S. Onuki, D. Miura, *The 65th JSAP Spring Meeting,* **2018,** 20a-D102-2 [In Japanese].

[9]   K. Tanigaki, T. Kanagasekaran, S. Onuki, D. Miura, H. Shimotani, *The 79th JSAP Autumm Meeting,* **2018,** 20a-231C-3 [In Japanese].

[10] H. Shimotani, T. Kanagasekaran, S. Onuki, D. Miura, K. Tanigaki, *The 79th JSAP Autumm Meeting,* **2018,** 20a-231C-4 [In Japanese].

[11] K. Tanigaki, T. Kanagasekaran, H. Shimotani, S. Onuki, D. Miura, *The 66th JSAP Spring Meeting,* **2019,** 11a-S222-1 [In Japanese].

[12] H. Shimotani, T. Kanagasekaran, S. Onuki, D. Miura, K. Tanigaki, *The 66th JSAP Spring Meeting,* **2019,** 11a-S222-2 [In Japanese].

List of Publications

[1] S. Dokiya, Y. Ono, F. Sasaki, S. Hotta, H. Yanagi, "Organic Light-Emitting Diodes with Heterojunction of Thiophene/Phenylene Co-Oligomer Derivatives" *J. Nanosci. Nanotechnol.* **2016,** 16, 3194.

[2] S. Dokiya, F. Sasaki, S. Hotta, H. Yanagi, "Improved Electroluminescence with Reversed Bilayers of Thiophene/Phenylene Co-Oligomer Derivatives" *Jpn. J. Appl. Phys.* **2016,** 55, 03DC13.

[3] S. Dokiya, F. Sasaki, H, Yanagi, "Fabrication of Polycrystalline Films of Cyano-Substituted Thiophene/Phenylene Co-Oligomer by Vaporized Film Deposition Method" *J. Cryst. Growth* **2017,** 468, 792.

[4] F. Sasaki, S. Dokiya, H, Yanagi, "Optically Pumped Lasing of Cyano-substituted Thiophene/Phenylene Co-Oligomers Microcrystals Fabricated by The Slide Boat Method" *Jpn. J. Appl. Phys.* **2019,** 58, SBBG05.

[5] S. Dokiya, H. Ishigami. T. Akazawa, F. Sasaki, H. Yanagi, "Organic Light-emitting Diodes with *PIN* Double-hetero Structure of Thiophene/Phenylene Co-Oligomer Derivatives" submitted.

[6] S. Dokiya, H. Mizuno, H. Katsuki, K. Yamashita, F. Sasaki, H. Yanagi, "Strong Exciton-photon Coupling in Organic Microcavity Electroluminescence Devices with Thiophene/Phenylene Co-Oligomer Derivatives" submitted.

Research Funds

Awards

[1] Outstanding Student Poster Award: Eight International Conference on Molecular Electronics and Bioelectronics (M&BE8), Tower Hall Funabori, Tokyo, Japan, S. Dokiya, F. Sasaki, S. Hotta, H. Yanagi, "Improved Electroluminescence with Reversed Bilayers of Thiophene/Phenylene Co-Oligomer Derivatives", 23, June, 2015.

[2] NAIST Excellent Student Scholarship Program (NAIST Top Scholarship Program): Nara Institute of Science and Technology (NAIST), Nara, Japan, S. Dokiya, "Fabrication and Characterization of Organic Electroluminescence Devices with Microcavity Structure"5, July, 2016. [in Japanese]

[3] Poster Award: The 78rd Japan Society of Applied Physics (JSAP) Autumn Meeting, Fukuoka Conventional Center, Fukuoka, Japan, S. Dokiya, H. Mizuno, H. Katsuki, K. Yamashita, F. Sasaki, H. Yanagi, "Organic Electroluminescence Devices in Microcavity Structure with π-Conjugated Oligomers", 1, October, 2017. [in Japanese]

[4] Oral Presentation Award: NAIST Best Student Award in the Ph. D. Thesis Defense, Graduate School of Materials Science, Nara Institute of Science and Technology (NAIST), Nara, Japan, S. Dokiya, "Organic Electroluminescence Devices with Microcavity Structure of Thiophene/Phenylene Co-Oligomer Thin Films" 22, March, 2019. [in Japanese]

Others

[1] AIST Innovation School Program (Short Course): National Institute of Advanced Industrial Science and Technology (AIST), Host Researcher: Dr. Fumio Sasaki, October 1, 2015- March 31, 2016.

[2] AIST Innovation School Program (Full Course): National Institute of Advanced Industrial Science and Technology (AIST), Host Researcher: Dr. Fumio Sasaki, April 1, 2016- March 31, 2017.

[3] Nanotechnology Platform Students Training Program: Nanotechnology Platform Japan, Host Researcher: Dr. Hiroyuki Matsuzaki, Advanced Industrial Science and Technology (AIST), August 1-3, 2017.

Acknowledgements

Shohei Dokiya